Generalized failure law for landslides, rockbursts, glacier breakoffs, and volcanic eruptions

Qinghua Lei[1]*, Didier Sornette[2]

[1] Department of Earth Sciences, Uppsala University; Uppsala, 752 36, Sweden.

[2] Institute of Risk Analysis, Prediction and Management, Academy for Advanced Interdisciplinary Studies, Southern University of Science and Technology; Shenzhen, 518055, China.

*Corresponding author. Email: qinghua.lei@geo.uu.se

Abstract

Catastrophic failures have momentous impact in many scientific and technological fields but remain challenging to understand and predict. One key difficulty lies in the burstiness of rupture phenomena, which typically involve a series of progressively shorter quiescent phases punctuated by sudden bursts, rather than a smooth continuous progression. This seemingly erratic pattern challenges the conventional power law assumption of continuous scale invariance. Here, we propose a generalized material failure law based on the log-periodic power law, which better captures the discrete scale invariance inherent in intermittent rupture dynamics. Our method's superiority is demonstrated through testing on 109 historical geohazard events, including landslides, rockbursts, glacier breakoffs, and volcanic eruptions. The results indicate that our method is general and robust, offering significant potential to forecast catastrophic failures.

Introduction

Catastrophic failure occurs in a wide spectrum of geological materials such as rock, soil, and ice, driving various extreme geohazards like landslides, rockbursts, glacier breakoffs, and volcanic eruptions that jeopardize life and property (1–4). It is thus crucial to develop the best possible predictive understanding of these rupture phenomena, which is a fundamental goal of many scientific and technological disciplines, such as geology, seismology, glaciology, volcanology, mechanics, and engineering. Various empirical and physical approaches have been proposed to describe geomaterial failure, with the power law singularity (PLS) model and the derived inverse rate technique (5–7) being widely adopted for time-to-failure analysis of geohazard events (8–15). Over the past decades, great efforts have also been devoted to develop and deploy high-precision monitoring technologies to observe various geohazards (3, 13, 16, 17). However, only a limited number of catastrophic events have been successfully predicted so far. One major uncertainty stems from the sporadic nature of rupture in heterogeneous materials, typically marked by a sequence of progressively shorter quiescent phases interspersed with sudden intense bursts (18–21), rather than a smooth continuous progression of deformation and damage. This seemingly erratic pattern complicates failure predictions as it challenges the continuous scale invariance assumed by the simple power law (5–8).

To address this issue, we propose a generalized failure law based on the log-periodic power law singularity (LPPLS) model. Amounting mathematically to a generalization of the power law exponent from real to complex numbers, this new failure law captures the partial break of continuous scale invariance to discrete scale invariance (22) that is inherent to the intermittent dynamics of damage and rupture processes in heterogeneous materials. We demonstrate the superiority of our LPPLS model over the conventional PLS model using real datasets (geodetic observations, geophysical records, and geochemical measurements) of 109 historical catastrophic events, including landslides, rockbursts, glacier breakoffs, and volcanic eruptions.

Theory

The response of a material prior to a catastrophic failure is generically governed by the following nonlinear dynamic equation (*5, 6*):

$$\ddot{\Omega} = \eta \dot{\Omega}^{\alpha}, \text{ with } \alpha > 1, \tag{1}$$

where Ω is an observable quantity (e.g., displacement, strain, energy release, gas emission), η is a constant, and α is the exponent defining the degree of nonlinearity. The condition of $\alpha > 1$ ensures the presence of positive feedbacks (*23*), where the instantaneous growth rate of $\dot{\Omega}$ defined as $d(\ln\dot{\Omega})/dt$ increases super-linearly as a function of $\dot{\Omega}$. This corresponds to a super-exponential dynamic ending with a finite-time singularity at which a catastrophic failure occurs. This is seen by integrating equation (1), which yields:

$$\dot{\Omega} = \kappa(t_c - t)^{-\xi}, \text{ with } \xi > 0, \tag{2}$$

where $\kappa = (\xi/\eta)^{\xi}$, $\xi = 1/(\alpha - 1)$, t is time, and t_c is the time of failure determined from the initial condition $\dot{\Omega}(t = t_0) = \dot{\Omega}_0$. Here, $\xi > 0$ (for $\alpha > 1$) ensures that $\dot{\Omega}$ exhibits a singular behavior at $t = t_c$. A further integration of equation (2) leads to the PLS formulation (*5–8*) (see Materials and Methods):

$$\Omega(t) = A + B(t_c - t)^m, \text{ with } m < 1, \tag{3}$$

where A and $B = -\kappa/m$ are constants, and $m = 1 - \xi$ is a critical exponent. Equation (3) is the general solution of Ω for $\alpha > 1$, $\xi > 0$, and thus $m < 1$ including $m = 0$ (see Materials and Methods), corresponding to an acceleration up to t_c. For $\alpha > 2$, $0 < \xi < 1$ and thus $0 < m < 1$, $\dot{\Omega}$ diverges at t_c but Ω converges to the finite value A; for $1 < \alpha < 2$, $\xi > 1$ and thus $m < 0$, both $\dot{\Omega}$ and Ω diverge at t_c.

We now consider a generalized scenario where the critical exponent is extended from real to complex numbers. Then, the first-order Fourier expansion of the general solution of Ω leads to the following LPPLS formula (*19, 22*) (see Materials and Methods):

$$\Omega(t) = A + \left\{ B + C\cos\left[\omega\ln(t_c - t) - \phi\right] \right\}(t_c - t)^m, \text{ with } m < 1, \tag{4}$$

expressing a log-periodic correction to the power law scaling, where C is a constant, ω is the angular log-periodic frequency, and ϕ is a phase shift. Incorporating a discrete hierarchy of time scales (see Materials and Methods), the LPPLS model captures the non-monotonous dynamics of the system with a geometric increase in burst frequency on the approach to t_c. A mechanism for this log-periodicity relies on the cascade of Mullins-Sekerka instabilities of competing growing cracks (*24*) with a relative amplitude typically on the order of 10^{-1} (*22*), driven by the localized and threshold nature of the mechanics of rupture in heterogeneous materials (*20, 21*). The LPPLS model is applicable to both constant and varying loading conditions, as demonstrated in the previous experimental and numerical studies (*18, 20, 25–27*).

Applications

We extensively test the LPPLS versus PLS models in the diverse contexts of landslides, rockbursts, glacier breakoffs, and volcanic eruptions. We implement a stable and robust model calibration scheme, briefly described as follows (see Materials and Methods for detailed procedures). First, the Lagrange regularization approach (*28*) is employed to endogenously detect the onset of the failure crisis, based on which the optimal time window is defined; here, the end of this time window is fixed at the last available data point prior to the failure. Then, the optimal parameter values for the LPPLS

or PLS model are determined by minimizing the sum of the squares of the residuals, which quantifies the difference between the model and data (29). The LPPLS model has seven parameters t_c, m, ω, ϕ, A, B, and C (with the four linear parameters A, B, $C \cos \phi$, and $C \sin \phi$ slaved to the three nonlinear ones t_c, m, and ω; see Materials and Methods), while the PLS model has four parameters t_c, m, A, and B (with the two linear parameters A and B slaved to the two nonlinear ones t_c and m; see Materials and Methods).

We quantitatively examine the performance of the two models based on a comprehensive list of evaluation metrics (see Materials and Methods). We first analyze the frequency distribution and empirical cumulative distribution function (eCDF) of residuals and further compute the normalized root mean square error (NRMSE). These metrics enable us to quantify the mismatch between the models and data. We also compute the normalized Akaike information criterion (NAIC) and normalized Bayesian information criterion (NBIC), which reward the goodness-of-fit while introducing a penalty term for the number of parameters. This enables an assessment of the relative quality of the two competing models having different numbers of parameters, with the one having the lower NAIC and NBIC values preferred. Furthermore, we test the null hypothesis H_0 that the data follow the PLS model (against the alternative that the data follow the LPPLS model) using the Wilks test, which is the most powerful test for comparing two competing models with one nested in another (here the PLS model is indeed nested in the LPPLS model). If the p-value for the Wilks test is below the prescribed significance level (e.g., 0.05), H_0 is rejected. Moreover, we perform two-sample Kolmogorov-Smirnov (KS) and Anderson-Darling (AD) tests of the null hypothesis that the probability distributions of the LPPLS and PLS residuals are identical. If the p-value is smaller than the significance level, the null is rejected, which may additionally indicate model superiority.

The first study case is the Veslemannen landslide in Norway. This instability complex, consisting of high-grade metamorphic rocks, has been continuously monitored since October 2014 by a ground-based interferometric synthetic-aperture radar system with an accuracy of 0.5 mm (30). This landslide primarily exhibited active movements during summer and autumn seasons, likely due to rainwater infiltration into the slope through the thawed upper frost zones. On September 5, 2019, a volume of ~54,000 m^3 rock collapsed. Prior to the failure, this landslide shifted significantly, displacing several meters over the course of approximately 3 months, showing an accelerating and oscillating behavior (see Fig. 1A for the monitoring data at one of the seven radar points and Fig. S1 for the data of all radar points). It is evident that the LPPLS model gives a much better fit to the data, with both the acceleration and oscillation well captured, whereas the PLS model only depicts the general acceleration trend (Fig. 1A and Fig. S1). The LPPLS residuals are confined in a much narrower range compared to the PLS residuals (Fig. 1A and Fig. S1, insets). The LPPLS model shows significantly lower NRMSE, NAIC, and NBIC values, while the p-values for the Wilks, KS, and AD tests are all well below 0.05 (Table 1), suggesting that the LPPLS model outperforms the PLS model. The superior performance of the LPPLS model is further demonstrated by its estimated t_c which is very close to the actual failure time (with a small discrepancy of 0.13 day; note that the data have a daily aggregation resolution), whereas the t_c estimated by the PLS model is about 9 days after the actual failure (Table 2).

The second example is a rockburst event that occurred in an underground mine at New South Wales, Australia (31). This coal mine, located at a depth of about 250 m, was mined using the longwall method. An in-situ monitoring system using multipoint extensometers (with an accuracy of 0.5 mm) was installed to record the roof displacement of a gateroad, which is a rectangular tunnel with a width of 5.2 m and a height of 3 m providing access to the longwall face. The roof catastrophically failed on June 4, 2004, prior to which a precursory accelerating and oscillating behavior was observed (Fig. 1B). A visual inspection indicates that the LPPLS model well captures the superimposed acceleration-oscillation

behavior of the roof, whereas the PLS model can only track the overall acceleration trend (Fig. 1B). This is consistent with the frequency and eCDF distributions of residuals (Fig. 1B inset), demonstrating that the LPPLS model more closely matches the data. The LPPLS model is also associated with smaller NRMSE, NAIC, and NBIC values than the PLS model, while the p-values for the Wilks, KS, and AD tests are all below 0.05 (Table 1). Furthermore, the estimated t_c by the LPPLS model is closer to the actual failure time (Table 2). All these results suggest that the LPPLS model surpasses the PLS model.
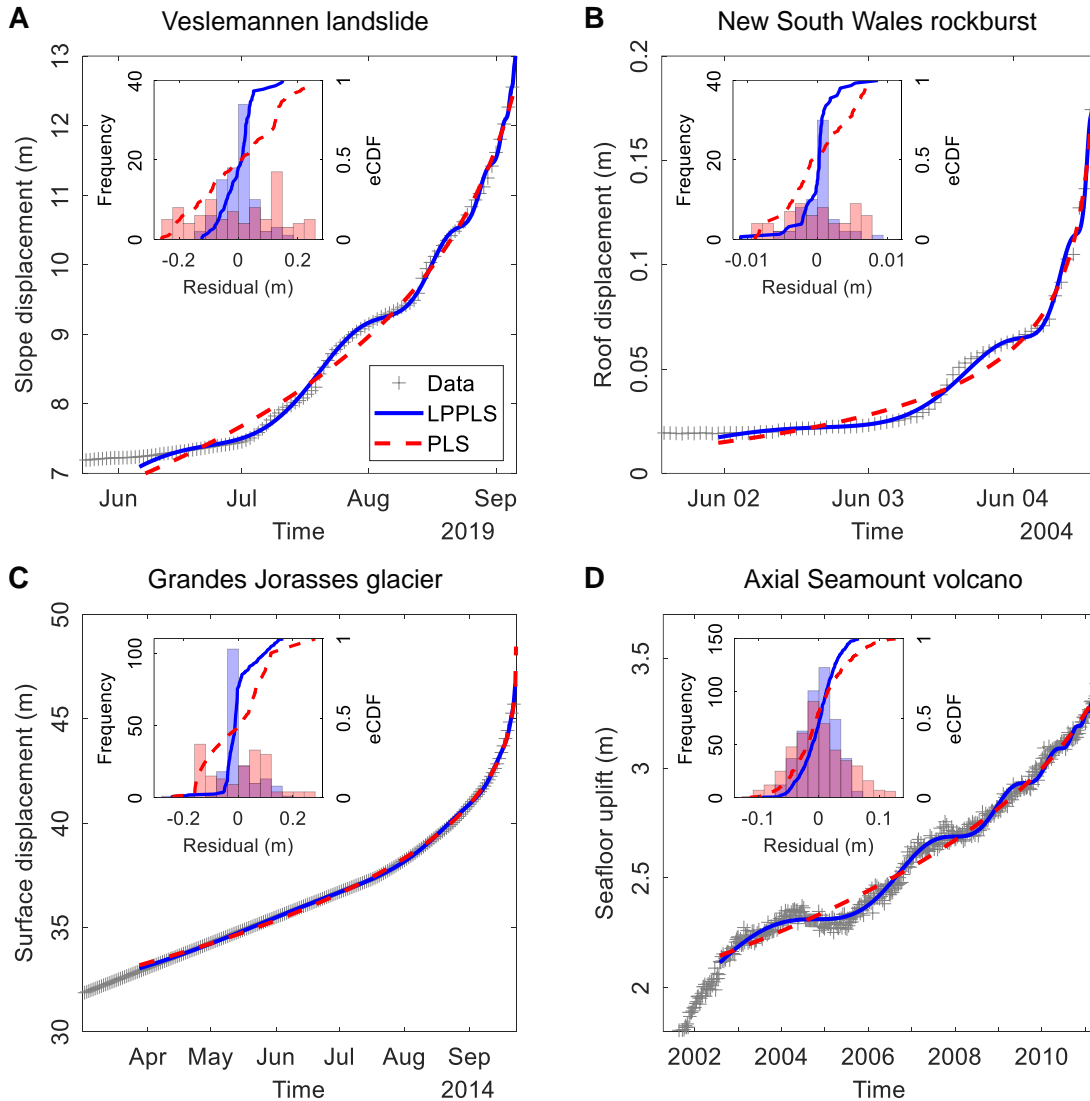

Fig. 1. Comparison between the LPPLS and PLS models in fitting the monitoring data of various geohazard events. (A) Slope surface displacement (aggregated on a daily basis) prior to a catastrophic landslide at Veslemannen, Norway. **(B)** Tunnel roof displacement (aggregated on an hourly basis) prior to a violent rockburst at New South Wales, Australia. **(C)** Glacier surface displacement (aggregated on a daily basis) prior to a rapid ice breakoff at Grandes Jorasses, Italy. **(D)** Seafloor uplift (aggregated on a weekly basis) prior to an explosive volcanic eruption at Axial Seamount, USA. Note that the raw measurement data for these events, originally recorded at higher frequencies, are aggregated on a lower frequency to expedite calibration and facilitate visualization.

The next case is a hanging cold glacier located on the south face of Grandes Jorasses, Italy and at an elevation of 3950 m above sea level (*13*). Surface displacements of this glacier, measured by a

robotic total station with multiple reflectors, were evaluated with an accuracy of ~1 cm. A large volume of ~105,000 m^3 ice broke off in two consecutive events on September 23 and 29, 2014 (*32*). We focus on the first breakoff event. One can see that this glacier experienced a generally smooth acceleration behavior over several months, for which both the LPPLS and PLS models show a close match to the trend (Fig. 1C) and provide excellent estimates of the failure time (Table 2). However, the LPPLS residuals are much smaller than the PLS residuals (Fig. 1C inset). The NRMSE, NAIC, and NBIC values of the LPPLS model are considerably lower than those of the PLS model, while the *p*-values for the Wilks, KS, and AD tests are all well below 0.05 (Table 1). These metrics collectively demonstrate that the LPPLS model performs better than the PLS model.

Table 1. Comparison between the LPPLS and PLS models in fitting the monitoring data of the Veslemannen landslide, New South Wales rockburst, Grandes Jorasses glacier, and Axial Seamount volcano.

Evaluation metrics	Veslemannen landslide	New South Wales rockburst	Grandes Jorasses glacier	Axial Seamount volcano
$NRMSE_{LPPLS}$	5.55×10^{-4}	4.34×10^{-5}	2.56×10^{-4}	6.02×10^{-4}
$NRMSE_{PLS}$	3.73×10^{-3}	1.42×10^{-4}	1.67×10^{-3}	1.55×10^{-3}
$NAIC_{LPPLS}$	-2.84	-8.85	-2.80	-4.31
$NAIC_{PLS}$	-1.00	-7.76	-1.46	-3.37
$NBIC_{LPPLS}$	-2.64	-8.61	-2.68	-4.24
$NBIC_{PLS}$	-0.89	-7.62	-1.39	-3.34
p-value (Wilks test)	0.00	0.00	0.00	0.00
p-value (KS test)	0.00	0.03	0.00	0.00
p-value (AD test)	0.00	0.00	0.00	0.00

Table 2. Parameters of the LPPLS and PLS models fitted to the monitoring data of the Veslemannen landslide, New South Wales rockburst, Grandes Jorasses glacier, and Axial Seamount volcano.

Model parameters		Veslemannen landslide	New South Wales rockburst	Grandes Jorasses glacier	Axial Seamount volcano
LPPLS:					
	t_c	0.13	0.02	0.00	6.00
	m	0.42	-0.12	0.33	0.64
	ω	7.49	4.94	4.94	9.23
	ϕ	-0.82	-0.01	0.65	0.61
	A	13.64	-0.24	48.76	3.38
	B	-1.03	0.28	-2.88	-0.01
	C	4.09×10^{-2}	5.77×10^{-3}	3.56×10^{-2}	5.12×10^{-4}
PLS:					
	t_c	9.23	0.05	0.00	323.10
	m	0.07	-0.28	0.34	0.32
	A	43.93	-0.08	48.46	4.38
	B	-26.85	0.12	-2.66	-0.16

Note: t_c is in day; m, ω, and ϕ are dimensionless; A is in meter; B and C are in meter per day^m. The actual time of failure corresponds to time $t = 0$ day. The start of the calibration time window is detected by the Lagrange regularization approach (see Materials and Methods), while the calibration time window ends at the last available data point before the actual failure occurs.
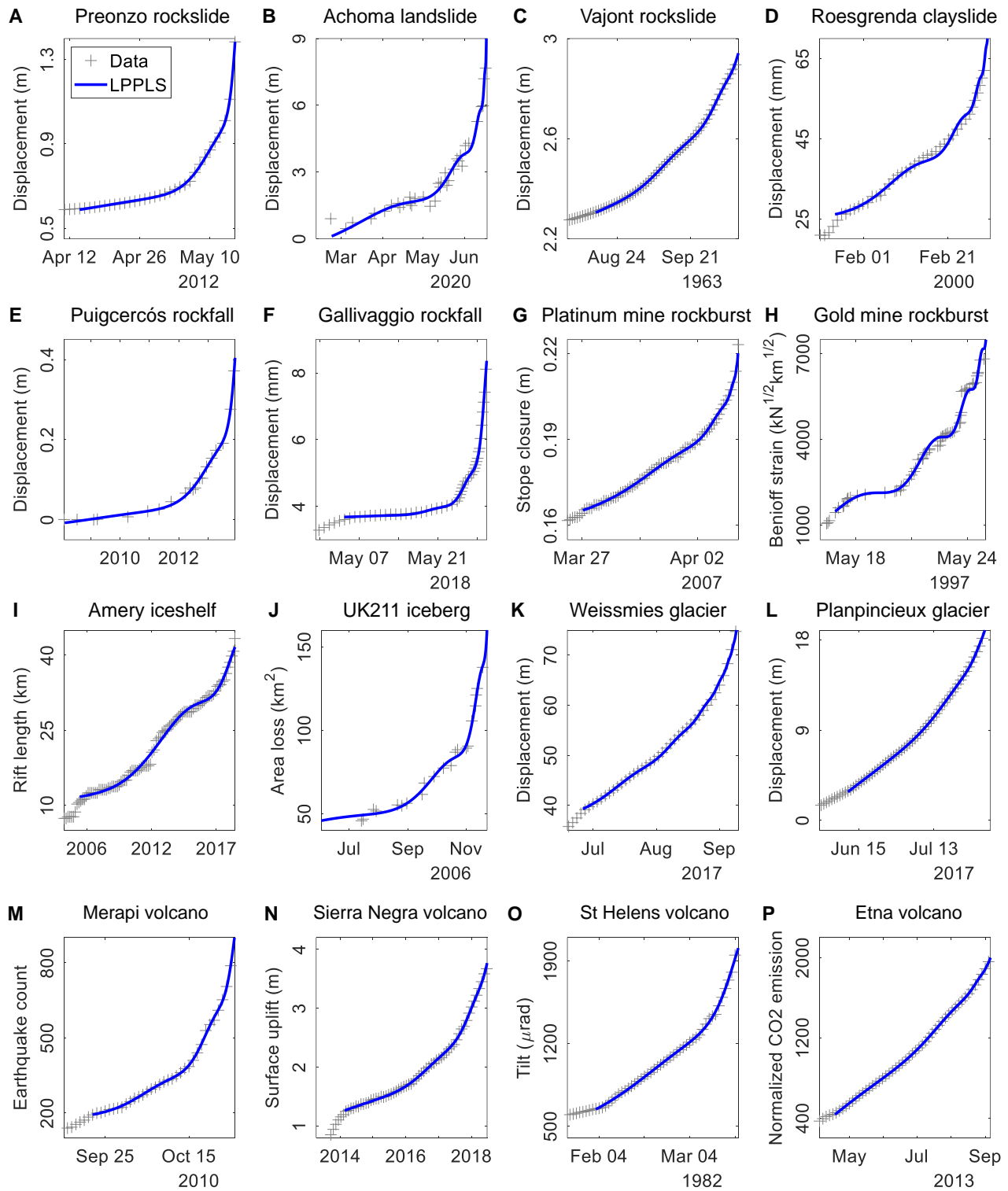
Fig. 2. Application of the generalized failure law based on the LPPLS model to various geohazard events. (**A**) Preonzo rockslide, Switzerland. (**B**) Achoma landslide, Peru. (**C**) Vajont rockslide, Italy. (**D**) Roesgrenda clayslide, Norway. (**E**) Puigcercós rockfall, Spain. (**F**) Gallivaggio rockfall, Italy. (**G**) Merensky rockburst, South Africa. (**H**) Goldmine rockburst, South Africa. (**I**) Amery iceshelf, Antarctica. (**J**) UK211 iceberg, Antarctica. (**K**) Weissmies glacier, Switzerland. (**L**) Planpincieux glacier, Italy. (**M**) Merapi volcano, Indonesia. (**N**) Sierra Negra volcano, Ecuador. (**O**) St. Helens volcano, USA. (**P**) Etna volcano, Italy.

The fourth example is Axial Seamount, an active submarine volcano with a summit caldera at ~1.5 km depth and a base at ~2.4 km, located ~500 km offshore Oregon, USA (*33*). This basaltic volcano with magma supplied from the Cobb hotspot has erupted three times over the past 26 years, in 1998, 2011, and 2015. It has been closely monitored by a cabled network of seafloor instruments since 1998, with the seafloor vertical deformation measured at a resolution of ~1 cm through bottom and mobile pressure recorders (*34*). We focus on the eruption event in April 2011, prior to which the volcano exhibited a series of inflation-deflation cycles over about 8 years (Fig. 1D). The LPPLS model effectively captures the oscillatory behavior of the seafloor deformation superimposed on an overall acceleration, whereas the PLS model only depicts the overall trend (Fig. 1D). Compared to the PLS model, the LPPLS model is associated with smaller residuals (Fig. 1D inset) and lower values for NRMSE, NAIC, and NBIC (Table 1). Additionally, the *p*-values for the Wilks, KS, and AD tests are all well below 0.05 (Table 1). The failure time estimated by the LPPLS model has a discrepancy of only 6 days compared to the actual eruption time (i.e., just one point of the weekly-aggregated data resolution), while that by the PLS model is almost 1 year after. All these results support the superior performance of the LPPLS model.

We further test the LPPLS model for describing the geomaterial failure behavior during various geohazard events (see Fig. 2 for some typical examples among 109 events analyzed in total; refer to Fig. S1-S18 and Tables S1-S16 for the complete inventory). More specifically, Fig. 2A shows the slope displacement data monitored by an extensometer at the Preonzo rockslide, Switzerland which collapsed on May 15, 2012 (*35*). Fig. 2B presents the displacement time series constructed from high-frequency optical satellite images for the Achoma landslide, Peru, which failed in June 2020 (*36*). Fig. 2C illustrates the displacement evolution of the Vajont rockslide, Italy, prior to a catastrophic failure on October 9, 1963 (*37*). Fig. 2D shows the acceleration behavior recorded by an extensometer at a quick clay slide at Roesgrenda, Norway (*38*). Fig. 2E displays the displacement data of a rock cliff acquired from a Terrestrial LiDAR instrument at Puigcercós, Spain, where a rockfall event occurred on December 3, 2013 (*39*). Fig. 2F depicts the displacement time series of a subvertical granitic slope monitored by a ground-based synthetic aperture radar at Gallivaggio, Italy, where a rockfall event occurred on May 29, 2018 (*40*). Fig. 2G shows the stope closure data measured by a closure meter prior to a violent rockburst in a deep platinum mine, South Africa (*41*). Fig. 2H gives the cumulative Benioff strain of seismic energy released before a large rockburst event in a deep gold mine, South Africa (*42*). Fig. 2I shows the multi-year rift propagation in the Amery Ice Shelf, Antarctica, preceding a large calving event on September 25, 2019 (*43*). Fig. 2J depicts the temporal evolution of area loss of the UK211 iceberg that rapidly disintegrated in 2006, tracked by the satellite-based Moderate Resolution Imaging Spectroradiometer sensor (*44*). Fig. 2K displays the surface displacement data of a polythermal glacier at Weissmies, Switzerland prior to a breakoff on September 10, 2017, recorded by a high-resolution camera (*45*). Fig. 2L gives the displacement data of a polythermal glacier at Planpincieux, Italy prior to a breakoff on September 16, 2015 (*46*). Fig. 2M illustrates the temporal evolution of earthquake count prior to an explosive eruption of the Merapi stratovolcano, Indonesia in October 2010 (*47*). Fig. 2N shows the ground uplift data recorded by a continuous Global Positioning System network during the 2018 eruption of the Sierra Negra shield volcano, Ecuador (*48*). Figs. 2O plots the tiltmeter measurements at the St. Helens stratovolcano during its 1982 eruption (*49*). Fig. 2P shows the temporal variation of cumulative normalized soil CO_2 efflux recorded by a geochemical monitoring network at the Etna stratovolcano that erupted in September 2013 (*50*).

The LPPLS model provides an excellent fit to the documented failure phenomena in all these cases, effectively capturing both the accelerating and oscillating behavior (a detailed comparison with the PLS model is given by Tables S9-S12). In total, we have tested 109 historical events (consisting of 160 time series data), including 49 landslides, 11 rockbursts, 17 glacier breakoffs, and 32 volcanic eruptions (Supplementary Materials). Fig. 3 illustrates the comparative model performance of LPPLS against PLS across the entire dataset (see Tables S9-S12 for more details). The NRMSE of the LPPLS

model is consistently smaller than that of the PLS model across the entire dataset; notably, for 67.5% of the data, the NRMSE of the LPPLS model is less than half that of the PLS model. The NAIC (respectively NBIC) values of the LPPLS model are lower than those of the PLS model by 0.5 unit for 65% (respectively 70%) of the data and by 1 unit for 35% (respectively 40%). Note that a 0.5 to 1 unit decrease in NAIC or NBIC corresponds to a relative likelihood improvement of 1.65 to 2.72 times per data point. For 91% of the data (Tables S9-S12), the p-value from the Wilks test is below 0.05, providing strong evidence of the LPPLS model's superiority. The p-values of the KS and AD tests are below 0.05 for 42% and 47% of the data, respectively, aligning with the fact that these tests are less powerful than the Wilks test, particularly given the limited data for some events (Tables S13-16). However, the evidence remains strong, as only 8 cases with p-values below 0.05 would be expected if the p-values were random. All these results collectively indicate the superior performance of the LPPLS model over the PLS model, because the former can constrain the fit to the bursty oscillating structures in the data while the latter is often poorly defined, particularly in the presence of noise.
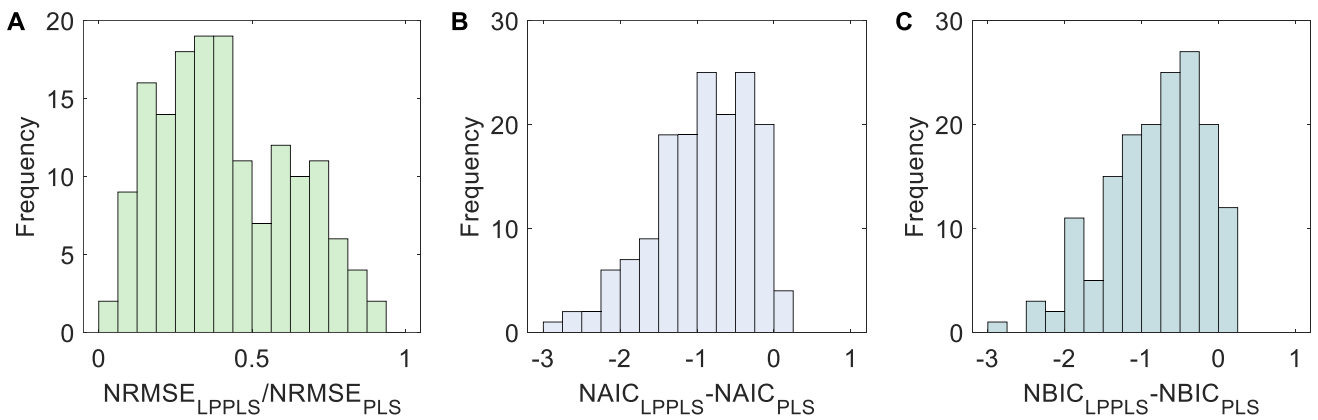

Fig. 3. Histograms showing a comparison of the evaluation metrics between the LPPLS and PLS models in fitting 109 geohazard events (with 160 time series monitoring data in total). (**A**) NRMSE ratio, (**B**) NAIC difference, and (**C**) NBIC difference between the LPPLS and PLS models.

Discussion

Our results reveal that the proposed generalized failure law can accurately describe the failure behavior of various geomaterials (rock, soil, and ice) under diverse contexts, ranging from landslides and rockbursts to glacier breakoffs and volcanic eruptions. These geohazard phenomena develop over a wide spectrum of time scales (from hours/days to months/years) and length scales (from meters to tens of kilometers). The broad applicability of our failure law highlights the commonality of different failure phenomena, which are mechanistically driven by the similar mechanisms involving interactions between many fractures, frictional processes, and final strain localization in heterogeneous materials. This failure law can be applied to various observables (e.g., surface displacement, tunnel closure, energy release, rift length, earthquake count, angular change, and gas emission) recorded by different instruments (e.g., extensometers, reflectors, tiltmeters, closuremeters, satellites, LiDAR, synthetic aperture radar, Global Positioning System, pressure recorders, and seismic/geochemical monitoring networks) (Tables S1-S4). These results indicate that our new failure law is general and robust, with significant potential to mitigate geohazard risks and enhance existing early warning systems. The LPPLS signatures observed in various geohazards imply the presence of characteristic time scales in the rupture of heterogeneous geomaterials, which could provide important insights into the underlying systems and/or physics as well as be very useful for prediction purposes (*21*). Our future work will focus on implementing this generalized failure law for prospective forecast of catastrophic events.

References

1. L. Caricchi, M. Townsend, E. Rivalta, A. Namiki, The build-up and triggers of volcanic eruptions. *Nat. Rev. Earth Environ.* **2**, 458–476 (2021).

2. Q. Lei, D. Sornette, H. Yang, S. Loew, Real-time forecast of catastrophic landslides via dragon-king detection. *Geophys. Res. Lett.* **50**, e2022GL100832 (2023).

3. X.-T. Feng, J. Liu, B. Chen, Y. Xiao, G. Feng, F. Zhang, Monitoring, warning, and control of rockburst in deep metal mines. *Engineering* **3**, 538–545 (2017).

4. J. N. Bassis, A. Crawford, S. B. Kachuck, D. I. Benn, C. Walker, J. Millstein, R. Duddu, J. Åström, H. A. Fricker, A. Luckman, Stability of ice shelves and ice cliffs in a changing climate. *Annu. Rev. Earth Planet. Sci.* **52**, 221–247 (2024).

5. B. Voight, A relation to describe rate-dependent material failure. *Science* **243**, 200–203 (1989).

6. B. Voight, A method for prediction of volcanic eruptions. *Nature* **332**, 125–130 (1988).

7. C. G. Bufe, D. J. Varnes, Predictive modeling of the seismic cycle of the Greater San Francisco Bay Region. *J. Geophys. Res. Solid Earth* **98**, 9871–9883 (1993).

8. I. G. Main, Applicability of time-to-failure analysis to accelerated strain before earthquakes and volcanic eruptions. *Geophys. J. Int.* **139**, F1–F6 (1999).

9. B. Voight, R. R. Cornelius, Prospects for eruption prediction in near real-time. *Nature* **350**, 695–698 (1991).

10. C. R. J. Kilburn, B. Voight, Slow rock fracture as eruption precursor at Soufriere Hills Volcano, Montserrat. *Geophys. Res. Lett.* **25**, 3665–3668 (1998).

11. C. R. J. Kilburn, D. N. Petley, Forecasting giant, catastrophic slope collapse: lessons from Vajont, Northern Italy. *Geomorphology* **54**, 21–32 (2003).

12. R. S. J. Sparks, Forecasting volcanic eruptions. *Earth Planet. Sci. Lett.* **210**, 1–15 (2003).

13. J. Faillettaz, M. Funk, C. Vincent, Avalanching glacier instabilities: Review on processes and early warning perspectives. *Rev. Geophys.* **53**, 203–224 (2015).

14. E. Intrieri, T. Carlà, G. Gigli, Forecasting the time of failure of landslides at slope-scale: A literature review. *Earth-Sci. Rev.* **193**, 333–349 (2019).

15. J. Leinauer, S. Weber, A. Cicoira, J. Beutel, M. Krautblatter, An approach for prospective forecasting of rock slope failure time. *Commun. Earth Environ.* **4**, 253 (2023).

16. V. Acocella, M. Ripepe, E. Rivalta, A. Peltier, F. Galetto, E. Joseph, Towards scientific forecasting of magmatic eruptions. *Nat. Rev. Earth Environ.* **5**, 5–22 (2023).

17. N. Casagli, E. Intrieri, V. Tofani, G. Gigli, F. Raspini, Landslide detection, monitoring and prediction with remote-sensing techniques. *Nat. Rev. Earth Environ.* **4**, 51–64 (2023).

18. J.-C. Anifrani, C. Le Floc'h, D. Sornette, B. Souillard, Universal log-periodic correction to renormalization group scaling for rupture stress prediction from acoustic emissions. *J. Phys. I* **5**, 631–638 (1995).

19. D. Sornette, C. G. Sammis, Complex critical exponents from renormalization group theory of earthquakes: Implications for earthquake predictions. *J. Phys. I* **5**, 607–619 (1995).

20. A. Johansen, D. Sornette, Critical ruptures. *Eur. Phys. J. B* **18**, 163–181 (2000).

21. D. Sornette, Predictability of catastrophic events: Material rupture, earthquakes, turbulence, financial crashes, and human birth. *Proc. Natl. Acad. Sci.* **99**, 2522–2529 (2002).

22. D. Sornette, Discrete-scale invariance and complex dimensions. *Phys. Rep.* **297**, 239–270 (1998).

23. C. G. Sammis, D. Sornette, Positive feedback, memory, and the predictability of earthquakes. *Proc. Natl. Acad. Sci.* **99**, 2501–2508 (2002).

24. Y. Huang, G. Ouillon, H. Saleur, D. Sornette, Spontaneous generation of discrete scale invariance in growth models. *Phys. Rev. E* **55**, 6433–6447 (1997).

25. W. I. Newman, D. L. Turcotte, A. M. Gabrielov, Log-periodic behavior of a hierarchical failure model with applications to precursory seismic activation. *Phys. Rev. E* **52**, 4827–4835 (1995).

26. M. Sahimi, S. Arbabi, Scaling laws for fracture of heterogeneous materials and rock. *Phys. Rev. Lett.* **77**, 3689–3692 (1996).

27. Y. Huang, H. Saleur, C. Sammis, D. Sornette, Precursors, aftershocks, criticality and self-organized criticality. *Europhys. Lett. EPL* **41**, 43–48 (1998).

28. G. Demos, D. Sornette, Comparing nested data sets and objectively determining financial bubbles' inceptions. *Phys. Stat. Mech. Its Appl.* **524**, 661–675 (2019).

29. V. Filimonov, D. Sornette, A stable and robust calibration scheme of the log-periodic power law model. *Phys. Stat. Mech. Its Appl.* **392**, 3698–3707 (2013).

30. L. Kristensen, J. Czekirda, I. Penna, B. Etzelmüller, P. Nicolet, J. S. Pullarello, L. H. Blikra, I. Skrede, S. Oldani, A. Abellan, Movements, failure and climatic control of the Veslemannen rockslide, Western Norway. *Landslides* **18**, 1963–1980 (2021).

31. B. Shen, A. King, H. Guo, Displacement, stress and seismicity in roadway roofs during mining-induced failure. *Int. J. Rock Mech. Min. Sci.* **45**, 672–688 (2008).

32. J. Faillettaz, M. Funk, M. Vagliasindi, Time forecast of a break-off event from a hanging glacier. *The Cryosphere* **10**, 1191–1200 (2016).

33. W. W. Chadwick, S. L. Nooner, D. A. Butterfield, M. D. Lilley, Seafloor deformation and forecasts of the April 2011 eruption at Axial Seamount. *Nat. Geosci.* **5**, 474–477 (2012).

34. S. L. Nooner, W. W. Chadwick, Inflation-predictable behavior and co-eruption deformation at Axial Seamount. *Science* **354**, 1399–1403 (2016).

35. S. Loew, S. Gschwind, V. Gischig, A. Keller-Signer, G. Valenti, Monitoring and early warning of the 2012 Preonzo catastrophic rockslope failure. *Landslides* **14**, 141–154 (2017).

36. P. Lacroix, J. Huanca, L. Albinez, E. Taipe, Precursory motion and time-of-failure prediction of the Achoma landslide, Peru, from high frequency PlanetScope satellites. *Geophys. Res. Lett.* **50**, e2023GL105413 (2023).

37. E. Nonveiller, The Vajont reservoir slope failure. *Eng. Geol.* **24**, 493–512 (1987).

38. T. Okamoto, J. O. Larsen, S. Matsuura, S. Asano, Y. Takeuchi, L. Grande, Displacement properties of landslide masses at the initiation of failure in quick clay deposits and the effects of meteorological and hydrological factors. *Eng. Geol.* **72**, 233–251 (2004).

39. M. J. Royán, A. Abellán, J. M. Vilaplana, Progressive failure leading to the 3 December 2013 rockfall at Puigcercós scarp (Catalonia, Spain). *Landslides* **12**, 585–595 (2015).

40. T. Carlà, T. Nolesini, L. Solari, C. Rivolta, L. Dei Cas, N. Casagli, Rockfall forecasting and risk management along a major transportation corridor in the Alps through ground-based radar interferometry. *Landslides* **16**, 1425–1435 (2019).

41. D. F. Malan, J. A. L. Napier, A. L. Janse van Rensburg, Stope deformation measurements as a diagnostic measure of rock behaviour: A decade of research. *J. South. Afr. Inst. Min. Metall.* **107**, 743–765.

42. G. Ouillon, D. Sornette, The concept of "critical earthquakes" applied to mine rockbursts with time-to-failure analysis. *Geophys. J. Int.* **143**, 454–468 (2000).

43. C. C. Walker, M. K. Becker, H. A. Fricker, A high resolution, three-dimensional view of the D-28 Calving Event from Amery Ice Shelf with ICESat-2 and satellite imagery. *Geophys. Res. Lett.* **48**, e2020GL091200 (2021).

44. T. Scambos, R. Ross, R. Bauer, Y. Yermolin, P. Skvarca, D. Long, J. Bohlander, T. Haran, Calving and ice-shelf break-up processes investigated by proxy: Antarctic tabular iceberg evolution during northward drift. *J. Glaciol.* **54**, 579–591 (2008).

45. L. Meier, M. Jacquemart, R. Steinacher, D. Jäger, M. Funk, "Monitoring of the Weissmies glacier before the failure event of September 10, 2017 with Radar Interferometry and high-resolution deformation camera" in *Proceedings of the International Snow Science Workshop* (Innsbruck, Austria, 2018).

46. D. Giordan, N. Dematteis, P. Allasia, E. Motta, Classification and kinematics of the Planpincieux Glacier break-offs using photographic time-lapse analysis. *J. Glaciol.* **66**, 188–202 (2020).

47. Surono, P. Jousset, J. Pallister, M. Boichu, M. F. Buongiorno, A. Budisantoso, F. Costa, S. Andreastuti, F. Prata, D. Schneider, L. Clarisse, H. Humaida, S. Sumarti, C. Bignami, J. Griswold, S. Carn, C. Oppenheimer, F. Lavigne, The 2010 explosive eruption of Java's Merapi volcano—A '100-year' event. *J. Volcanol. Geotherm. Res.* **241–242**, 121–135 (2012).

48. A. F. Bell, P. C. La Femina, M. Ruiz, F. Amelung, M. Bagnardi, C. J. Bean, B. Bernard, C. Ebinger, M. Gleeson, J. Grannell, S. Hernandez, M. Higgins, C. Liorzou, P. Lundgren, N. J. Meier, M. Möllhoff, S.-J. Oliva, A. G. Ruiz, M. J. Stock, Caldera resurgence during the 2018 eruption of Sierra Negra volcano, Galápagos Islands. *Nat. Commun.* **12**, 1397 (2021).

49. D. Dzurisin, J. A. Westphal, D. J. Johnson, Eruption prediction aided by electronic tiltmeter data at Mount St. Helens. *Science* **221**, 1381–1383 (1983).

50. A. Cannata, G. Spedalieri, B. Behncke, F. Cannavò, G. Di Grazia, S. Gambino, S. Gresta, S. Gurrieri, M. Liuzzo, M. Palano, Pressurization and depressurization phases inside the plumbing system of Mount Etna volcano: Evidence from a multiparametric approach. *J. Geophys. Res. Solid Earth* **120**, 5965–5982 (2015).

51. D. Sornette, *Critical Phenomena in Natural Sciences - Chaos, Fractals, Selforganization and Disorder: Concepts and Tools* (Springer, Berlin/Heidelberg, 2006).

52. S. Gluzman, D. Sornette, Log-periodic route to fractal functions. *Phys. Rev. E* **65**, 036142 (2002).

53. H. Saleur, C. G. Sammis, D. Sornette, Renormalization group theory of earthquakes. *Nonlinear Process. Geophys.* **3**, 102–109 (1996).

54. H. Saleur, D. Sornette, Complex exponents and log-periodic corrections in frustrated systems. *J. Phys. I* **6**, 327–355 (1996).

55. K. P. Burnham, D. R. Anderson, *Model Selection and Multimodel Inference: A Practical Information-Theoretic Approach* (Springer, New York, 2002).

56. C. G. Newhall, F. Costa, A. Ratdomopurbo, D. Y. Venezky, C. Widiwijayanti, N. T. Z. Win, K. Tan, E. Fajiculay, WOVOdat – An online, growing library of worldwide volcanic unrest. *J. Volcanol. Geotherm. Res.* **345**, 184–199 (2017).

57. G. T. Hancox, The 1979 Abbotsford Landslide, Dunedin, New Zealand: a retrospective look at its nature and causes. *Landslides* **5**, 177–188 (2008).

58. S. Hayashi, T. Yamamori, Forecast of time-to-slope failure by the a-tr method. *J. Jpn. Landslide Soc.* **28**, 1–8 (1991).

59. R. Tang, S. Ren, J. Li, P. Feng, H. Li, R. Deng, D. Li, K. Kasama, The failure mechanism of the Baishi landslide in Beichuan County, Sichuan, China. *Sci. Rep.* **14**, 17482 (2024).

60. B. Li, C. Zhao, J. Li, H. Chen, Y. Gao, F. Cui, J. Wan, Mechanism of mining-induced landslides in the karst mountains of Southwestern China: a case study of the Baiyan landslide in Guizhou. *Landslides* **20**, 1481–1495 (2023).

61. S. Loew, Monitoring data from the Insel compartment at Brienz/Brinzauls, Switzerland, ETH Zurich (2024); https://doi.org/10.3929/ethz-b-000670494.

62. T. Carlà, E. Intrieri, F. Raspini, F. Bardi, P. Farina, A. Ferretti, D. Colombo, F. Novali, N. Casagli, Perspectives on the prediction of catastrophic slope failures from satellite InSAR. *Sci. Rep.* **9**, 14137 (2019).

63. M. Saito, "Forecasting the time of occurrence of a slope failure" in *Proceedings of the 6th International Conference of Soil Mechanics and Foundation Engineering* (1965, Montreal, 1965; https://cir.nii.ac.jp/crid/1572543024011185664), pp. 537–541.

64. A. Cicoira, S. Weber, A. Biri, B. Buchli, R. Delaloye, R. Da Forno, I. Gärtner-Roer, S. Gruber, T. Gsell, A. Hasler, R. Lim, P. Limpach, R. Mayoraz, M. Meyer, J. Noetzli, M. Phillips, E. Pointner, H. Raetzo, C. Scapozza, T. Strozzi, L. Thiele, A. Vieli, D. Vonder Mühll, V. Wirz, J. Beutel, In situ observations of the Swiss periglacial environment using GNSS instruments. *Earth Syst. Sci. Data* **14**, 5061–5091 (2022).

65. C. O. Brawner, P. F. Stacey, "Hogarth Pit Slope Failure, Ontario, Canada" in *Developments in Geotechnical Engineering*, B. Voight, Ed. (Elsevier, 1979)vol. 14 of *Rockslides and Avalanches*, pp. 691–707.

66. T. M. Ryan, R. D. Call, "Applications of rock mass monitoring for stability assessment of pit slope failure" in *Proceedings of the 33rd U.S. Symposium on Rock Mechanics* (OnePetro, 1992; https://dx.doi.org/).

67. M. Chen, D. Huang, Q. Jiang, Slope movement classification and new insights into failure prediction based on landslide deformation evolution. *Int. J. Rock Mech. Min. Sci.* **141**, 104733 (2021).

68. U. Yamaguchi, T. Shimotani, A case study of slope failure in a limestone quarry. *Int. J. Rock Mech. Min. Sci. Geomech. Abstr.* **23**, 95–104 (1986).

69. A. Manconi, D. Giordan, Landslide failure forecast in near-real-time. *Geomat. Nat. Hazards Risk* **7**, 639–648 (2016).

70. G. Kayesa, "Prediction of slope failure at Letlhakane Mine with the Geomos slope monitoring system" in *Proceedings of the International Symposium on Stability of Rock Slopes in Open Pit*

Mining and Civil Engineering (The South African Institute of Mining and Metallurgy, South African, 2006).

71. X. Fan, Q. Xu, J. Liu, S. S. Subramanian, C. He, X. Zhu, L. Zhou, Successful early warning and emergency response of a disastrous rockslide in Guizhou province, China. *Landslides* **16**, 2445–2457 (2019).

72. E. Intrieri, F. Raspini, A. Fumagalli, P. Lu, S. Del Conte, P. Farina, J. Allievi, A. Ferretti, N. Casagli, The Maoxian landslide as seen from space: detecting precursors of failure with Sentinel-1 data. *Landslides* **15**, 123–133 (2018).

73. G. Gigli, R. Fanti, P. Canuti, N. Casagli, Integration of advanced monitoring and numerical modeling techniques for the complete risk scenario analysis of rockslides: The case of Mt. Beni (Florence, Italy). *Eng. Geol.* **120**, 48–59 (2011).

74. M. Jacquemart, K. Tiampo, Leveraging time series analysis of radar coherence and normalized difference vegetation index ratios to characterize pre-failure activity of the Mud Creek landslide, California. *Nat. Hazards Earth Syst. Sci.* **21**, 629–642 (2021).

75. I. Brown, M. Hittinger, R. Goodman, Finite element study of the Nevis Bluff (New Zealand) rock slope failure. *Rock Mech.* **12**, 231–245 (1980).

76. J. Carey, "The Progressive Development and Post-failure Behaviour of Deep-seated Landslide Complexes," thesis, Durham University (2011).

77. J. Zvelebill, M. Moser, Monitoring based time-prediction of rock falls: Three case-histories. *Phys. Chem. Earth Part B Hydrol. Oceans Atmosphere* **26**, 159–167 (2001).

78. T. Carlà, P. Farina, E. Intrieri, K. Botsialas, N. Casagli, On the monitoring and early-warning of brittle slope failures in hard rock masses: Examples from an open-pit mine. *Eng. Geol.* **228**, 71–81 (2017).

79. K. Fujisawa, G. Marcato, Y. Nomura, A. Pasuto, Management of a typhoon-induced landslide in Otomura (Japan). *Geomorphology* **124**, 150–156 (2010).

80. P. Mazzanti, F. Bozzano, I. Cipriani, A. Prestininzi, New insights into the temporal prediction of landslides by a terrestrial SAR interferometry monitoring case study. *Landslides* **12**, 55–68 (2015).

81. M. Saito, "Evidencial study on forecasting occurence of slope failure" (Applied Geological Survey Office Annual Report, Japan, 1979).

82. D. Kwan, Observations of the failure of a vertical cut in clay at Welland, Ontario. *Can. Geotech. J.* **8**, 283–298 (1971).

83. L. Xue, S. Qin, P. Li, G. Li, I. Adewuyi Oyediran, X. Pan, New quantitative displacement criteria for slope deformation process: From the onset of the accelerating creep to brittle rupture and final failure. *Eng. Geol.* **182**, 79–87 (2014).

84. A. Pralong, C. Birrer, W. A. Stahel, M. Funk, On the predictability of ice avalanches. *Nonlinear Process. Geophys.* **12**, 849–861 (2005).

85. M. Chmiel, F. Walter, A. Pralong, L. Preiswerk, M. Funk, L. Meier, F. Brenguier, Seismic constraints on damage growth within an unstable hanging glacier. *Geophys. Res. Lett.* **50**, e2022GL102007 (2023).

86. N. Dematteis, D. Giordan, F. Troilo, A. Wrzesniak, D. Godone, Ten-year monitoring of the Grandes Jorasses glaciers kinematics. Limits, potentialities, and possible applications of different monitoring systems. *Remote Sens.* **13**, 3005 (2021).

87. J. Faillettaz, A. Pralong, M. Funk, N. Deichmann, Evidence of log-periodic oscillations and increasing icequake activity during the breaking-off of large ice masses. *J Glaciol* **54**, 725–737 (2008).

88. J. Faillettaz, M. Funk, D. Sornette, Icequakes coupled with surface displacements for predicting glacier break-off. *J. Glaciol.* **57**, 453–460 (2011).

89. W. W. Chadwick, W. S. D. Wilcock, S. L. Nooner, J. W. Beeson, A. M. Sawyer, T. -K. Lau, Geodetic monitoring at Axial Seamount since its 2015 eruption reveals a waning magma supply and tightly linked rates of deformation and seismicity. *Geochem. Geophys. Geosystems* **23**, e2021GC010153 (2022).

90. J. C. Carracedo, V. R. Troll, K. Zaczek, A. Rodríguez-González, V. Soler, F. M. Deegan, The 2011–2012 submarine eruption off El Hierro, Canary Islands: New lessons in oceanic island growth and volcanic crisis management. *Earth-Sci. Rev.* **150**, 168–200 (2015).

91. Y. Sudo, H. Ono, A. W. Hurst, T. Tsutsui, T. Mori, M. Nakaboh, Y. Matsumoto, M. Sako, S. Yoshikawa, M. Tanaka, Y. Kobayashi, T. Hashimoto, T. Hoka, T. Yamada, H. Masuda, S. Kikuchi, Seismic activity and ground deformation associated with 1995 phreatic eruption of Kuju Volcano, Kyushu, Japan. *J. Volcanol. Geotherm. Res.* **81**, 245–267 (1998).

92. A. F. Bell, J. Greenhough, M. J. Heap, I. G. Main, Challenges for forecasting based on accelerating rates of earthquakes at volcanoes and laboratory analogues. *Geophys. J. Int.* **185**, 718–723 (2011).

93. A. Ratdomopurbo, F. Beauducel, J. Subandriyo, I. G. M. Agung Nandaka, C. G. Newhall, Suharna, D. S. Sayudi, H. Suparwaka, Sunarta, Overview of the 2006 eruption of Mt. Merapi. *J. Volcanol. Geotherm. Res.* **261**, 87–97 (2013).

94. T. P. Miller, B. A. Chouet, The 1989–1990 eruptions of Redoubt Volcano: An introduction. *J. Volcanol. Geotherm. Res.* **62**, 1–10 (1994).

95. K. F. Bull, H. Buurman, An overview of the 2009 eruption of Redoubt Volcano, Alaska. *J. Volcanol. Geotherm. Res.* **259**, 2–15 (2013).

96. D. J. Geist, K. S. Harpp, T. R. Naumann, M. Poland, W. W. Chadwick, M. Hall, E. Rader, The 2005 eruption of Sierra Negra volcano, Galápagos, Ecuador. *Bull. Volcanol.* **70**, 655–673 (2008).

97. D. A. Swanson, T. J. Casadevall, D. Dzurisin, S. D. Malone, C. G. Newhall, C. S. Weaver, Predicting eruptions at Mount St. Helens, June 1980 through December 1982. *Science* **221**, 1369–1376 (1983).

98. A. F. Bell, M. Naylor, I. G. Main, The limits of predictability of volcanic eruptions from accelerating rates of earthquakes. *Geophys. J. Int.* **194**, 1541–1553 (2013).

99. S. R. Young, R. S. J. Sparks, W. P. Aspinall, L. L. Lynch, A. D. Miller, R. E. A. Robertson, J. B. Shepherd, Overview of the eruption of Soufriere Hills Volcano, Montserrat, 18 July 1995 to December 1997. *Geophys. Res. Lett.* **25**, 3389–3392 (1998).

100. S. Nakada, H. Shimizu, K. Ohta, Overview of the 1990–1995 eruption at Unzen Volcano. *J. Volcanol. Geotherm. Res.* **89**, 1–22 (1999).

Supplementary Materials for

Generalized failure law for landslides, rockbursts, glacier breakoffs, and volcanic eruptions

Qinghua Lei[1]*, Didier Sornette[2]

[1] Department of Earth Sciences, Uppsala University; Uppsala, 752 36, Sweden.

[2] Institute of Risk Analysis, Prediction and Management, Academy for Advanced Interdisciplinary Studies, Southern University of Science and Technology; Shenzhen, 518055, China.

*Corresponding author. Email: qinghua.lei@geo.uu.se

Materials and Methods

Derivation of the power law singularity (PLS) model

An integration of equation (2) in the Main Text leads to:

$$\Omega(t) = \begin{cases} A - \dfrac{\kappa}{m}(t_c - t)^m, & m \neq 0 \\ A - \kappa \ln(t_c - t), & m = 0 \end{cases},$$ (S1)

where $m = 1 - \xi < 1$ and A can be determined from the initial condition of $\Omega(t = t_0) = \Omega_0$, so that:

$$\Omega(t) = \begin{cases} \Omega_0 + \dfrac{\kappa}{m}\left[(t_c - t_0)^m - (t_c - t)^m\right], & m \neq 0 \\ \Omega_0 - \kappa \ln\left(\dfrac{t_c - t}{t_c - t_0}\right), & m = 0 \end{cases}.$$ (S2)

Recall that t_c is the time of failure determined from the other initial condition $\dot{\Omega}(t = t_0) = \dot{\Omega}_0$, giving $t_c = t_0 + (\xi / \eta)\dot{\Omega}_0^{-1/\xi}$.

For $m \to 0$, consider the Taylor expansion $(t_c - t_0)^m = e^{m\ln(t_c - t_0)} = 1 + m\ln(t_c - t_0) + O(m^2)$ and $(t_c - t)^m = e^{m\ln(t_c - t)} = 1 + m\ln(t_c - t) + O(m^2)$, we have:

$$\Omega(t) = \Omega_0 + \frac{\kappa}{m}\left[e^{m\ln(t_c - t_0)} - e^{m\ln(t_c - t)}\right] = \Omega_0 - \kappa \ln\left(\frac{t_c - t}{t_c - t_0}\right) + O(m).$$ (S3)

Thus, as $m \to 0$, the solution of $\Omega(t)$ for $m \neq 0$ converges to that for $m = 0$, so equation (2) in the Main Text with $B = -\kappa / m$ gives the general solution of $\Omega(t)$ for $m < 1$.

Derivation of the log-periodic power law singularity (LPPLS) model

Let us define:

$$\tilde{\Omega}(t) = \frac{\Omega(t) - A}{B} = (t_c - t)^m,$$ (S4)

where $B \neq 0$ ensures the presence of a finite-time singularity. The power law relation (S4) obeys the symmetry of scale invariance. This means that scaling $t_c - t$ by an arbitrary factor λ leads to a

corresponding scaling of the observable by factor $\mu(\lambda)$, while the $t_c - t$ dependence remains unchanged. Mathematically, this is expressed as:

$$\mu\tilde{\Omega}(t) = \left[\lambda(t_c - t)\right]^m. \tag{S5}$$

In other words, if we replace $t_c - t$ with $\lambda(t_c - t)$ and replace $\tilde{\Omega}$ with $\mu\tilde{\Omega}$ in equation (S4), the equality still holds, reflecting the scale invariance. From equations (S4) and (S5), we can derive the following equation that determines $\mu(\lambda)$:

$$\lambda^m / \mu = 1. \tag{S6}$$

It is often the case that, rather than deriving $\mu(\lambda)$ from λ and m, first-principle considerations provide the values of λ and μ, from which one derives the value of the exponent as:

$$m = \frac{\ln \mu}{\ln \lambda}. \tag{S7}$$

In the presence of continuous scale invariance, the above derivation holds for arbitrary value of λ with $\mu(\lambda)$ adjusting so that there is a single value of the exponent m given by equation (S7). The general theoretical procedure is usually formulated with the Renormalization Group (*51*) by taking the limit $\lambda = 1 + \delta \to 1$ ($\delta \to 0$) and $\mu = 1 + \zeta \to 1$ ($\zeta \to 0$), so that $m = \delta / \zeta$ in the limit.

The continuous scale invariance discussed above can be partially broken into a discrete scale invariance. This means that the power law relationship (S4) holds under scaling $t_c - t$ by specific factors that are integer powers λ^n of a specific scaling ratio $\lambda > 1$, where n is an arbitrary integer indexing the hierarchy of scales (*22*). There are several derivations of the corresponding spectrum of power law exponents m_n. The simplest one is to start from the identity $1 = \exp(i2\pi n)$ and substitute it into the right-hand-side of equation (S6). Solving for m_n yields the series of complex critical exponents:

$$m_n = m + in\omega, \tag{S8}$$

where m is the real part given by (S7), n is an arbitrary integer, and $\omega = 2\pi / \ln \lambda$. The general form of $\tilde{\Omega}$ can be expressed as an infinite sum of power laws $(t_c - t)^{m_n}$, similarly to a Fourier series (it is in fact a discrete Mellin transform generalization of discrete Fourier series, see e.g., (*52*)). The corresponding log-periodic power law is obtained by taking the real part of each power law $(t_c - t)^{m_n}$, since observables are real. This gives:

$$\tilde{\Omega}_n(t) = \text{Re}\left[(t_c - t)^{m_n}\right] = (t_c - t)^m \cos\left[n\omega\ln(t_c - t)\right]. \tag{S9}$$

Thus, the most general solution of $\tilde{\Omega}$ is given by a superposition of all the components of this generalized Fourier series in logarithmic scale (*19*):

$$\tilde{\Omega}(t) = (t_c - t)^m \sum_{n=0}^{+\infty} a_n \cos\left[n\omega\ln(t_c - t) - \phi_n\right], \tag{S10}$$

where a_n are the generalized Fourier coefficients and ϕ_n represent the phase shifts, with $a_0 = 1$ and $\phi_0 = 0$. The term for $n = 0$ defines a pure power law with fully continuous scale invariance governed by the real critical exponent m, while the terms for $n > 1$ introduce a partial breaking of continuous scale invariance into discrete scale invariance, resulting in a series of log-periodic oscillations decorating the pure power law (*22*). It has been proven that the amplitudes of the coefficients a_n decay fast with n (*52*), so that only the first correction term $n = 1$ is important in general (there are

exceptions in which higher-order terms need to be considered but we do not consider this situation here). Keeping the terms $n = 0$ and $n = 1$ in (S10) recovers the LPPLS formula, i.e., equation (4) in the Main Text.

The local maxima of the log-periodic term $C \cos[\omega \ln(t_c - t) - \phi]$ in the LPPLS formula occur at times converging to t_c according to a geometric time series $\{t_1, t_2, ..., t_k, ...\}$ with $t_c - t_k = \tilde{\tau} \lambda^{-k}$, where k is an integer and $\tilde{\tau} = \exp(\phi / \omega)$ is a time constant determined from the initial conditions. The geometric time series corresponds to the times for which the argument of the cosine function is an integer multiple of 2π.

Calibration of the LPPLS model

For the time series of N measurements of the observable quantity $\mathbf{\Omega} = \{\Omega_1, \Omega_2, ..., \Omega_N\}$ recorded at time $\mathbf{t} = \{t_1, t_2, ..., t_N\} \in [\tau, T]$ (τ and T respectively denote the start and end of the time window over which the fitting is performed), the LPPLS model is calibrated based on the following scheme (*29*).

The LPPLS model is written as:

$$\Omega(t) = A + \{B + C \cos[\omega \ln(t_c - t) - \phi]\}(t_c - t)^m, \qquad (S11)$$

with a parameter set $\boldsymbol{\theta}_{\text{LPPLS}} = \{A, B, C, t_c, m, \omega, \phi\}$ including seven parameters with the former three being linear and the latter four being nonlinear. By introducing $C_1 = C \cos\phi$ and $C_2 = C \sin\phi$, we can rewrite the LPPLS formula as:

$$\Omega(t) = A + B(t_c - t)^m + C_1(t_c - t)^m \cos[\omega \ln(t_c - t)] + C_2(t_c - t)^m \sin[\omega \ln(t_c - t)], \qquad (S12)$$

where the new parameter set $\boldsymbol{\theta}_{\text{LPPLS}} = \{A, B, C_1, C_2, t_c, m, \omega\}$ still has seven parameters but now with four linear and only three nonlinear parameters. To estimate all these parameters, we define the cost function as the sum of squared errors:

$$F(\boldsymbol{\theta}_{\text{LPPLS}}; \mathbf{\Omega}, \mathbf{t}) = \sum_{i=1}^{N} \varepsilon_i^2, \qquad (S13)$$

with each residual calculated as:

$$\varepsilon_i = \Omega_i - A - B(t_c - t_i)^m - C_1(t_c - t_i)^m \cos[\omega \ln(t_c - t_i)] - C_2(t_c - t_i)^m \sin[\omega \ln(t_c - t_i)]. \qquad (S14)$$

The ordinary least squares method amounts to minimizing the cost function (S13) to obtain the estimates for the model parameters:

$$\hat{\boldsymbol{\theta}}_{\text{LPPLS}} = \arg \min_{\boldsymbol{\theta}_{\text{LPPLS}}} F(\boldsymbol{\theta}_{\text{LPPLS}}; \mathbf{\Omega}, \mathbf{t}). \qquad (S15)$$

This is not a trivial task due to the strong nonlinearity of the cost function and the presence of multiple local minima.

To solve this minimization problem, we enslave the four linear parameters $\{A, B, C_1, C_2\}$ to the three nonlinear ones $\{t_c, m, \omega\}$ so as to reduce the minimization problem to:

$$\{\hat{t}_c, \hat{m}, \hat{\omega}\} = \arg \min_{t_c, m, \omega} F_1(t_c, m, \omega), \qquad (S16)$$

with the profiled cost function defined as:

$$F_1(t_c, m, \omega) = \min_{A,B,C_1,C_2} F(A, B, C_1, C_2, t_c, m, \omega) = F(t_c, m, \omega, \hat{A}, \hat{B}, \hat{C}_1, \hat{C}_2), \tag{S17}$$

and the estimates for the linear parameters $\{A, B, C_1, C_2\}$ obtained by solving the optimization problem for fixed values of the nonlinear parameters $\{t_c, m, \omega\}$:

$$\{\hat{A}, \hat{B}, \hat{C}_1, \hat{C}_2\} = \arg\min_{A,B,C_1,C_2} F(A, B, C_1, C_2, t_c, m, \omega), \tag{S18}$$

which has a unique solution analytically solved from the following system of linear equations:

$$\begin{bmatrix} N & \sum f_i & \sum g_i & \sum h_i \\ \sum f_i & \sum f_i^2 & \sum f_i g_i & \sum f_i h_i \\ \sum g_i & \sum f_i g_i & \sum g_i^2 & \sum g_i h_i \\ \sum h_i & \sum f_i h_i & \sum g_i h_i & \sum h_i^2 \end{bmatrix} \begin{bmatrix} \hat{A} \\ \hat{B} \\ \hat{C}_1 \\ \hat{C}_2 \end{bmatrix} = \begin{bmatrix} \sum \Omega_i \\ \sum \Omega_i f_i \\ \sum \Omega_i g_i \\ \sum \Omega_i h_i \end{bmatrix}, \tag{S19}$$

where $f_i = (t_c - t_i)^m$, $g_i = (t_c - t_i)^m \cos[\omega \ln(t_c - t_i)]$, and $h_i = (t_c - t_i)^m \sin[\omega \ln(t_c - t_i)]$.

The optimization problem (S16) can be further reformulated as:

$$\hat{t}_c = \arg\min_{t_c} F_2(t_c), \tag{S20}$$

with the cost function given by:

$$F_2(t_c) = \min_{m,\omega} F_1(t_c, m, \omega) = F_1(t_c, \hat{m}, \hat{\omega}), \tag{S21}$$

and the estimates for parameters $\{m, \omega\}$ obtained by solving the optimization problem:

$$\{\hat{m}, \hat{\omega}\} = \arg\min_{m,\omega} F_1(t_c, m, \omega). \tag{S22}$$

Here, a constraint of $4.94 \leq \omega \leq 15$ is imposed with the lower bound defined to prevent chaotic scenarios (53) and the upper bound defined to avoid spurious oscillations (29), so that the scaling ratio $\lambda = \exp(2\pi/\omega)$ is at the order of 2 (22), as suggested by general theoretical arguments (54).

Calibration of the PLS model

For the time series of N measurements of the observable quantity $\mathbf{\Omega} = \{\Omega_1, \Omega_2, ..., \Omega_N\}$ recorded at time $\mathbf{t} = \{t_1, t_2, ..., t_N\} \in [\tau, T]$ (τ and T respectively denote the start and end of the time window over which the fitting is performed), the PLS model is calibrated based on a scheme similar to the one for the LPPLS model.

The PLS model is written as:

$$\Omega(t) = A + B(t_c - t)^m, \tag{S23}$$

with a parameter set $\mathbf{\theta}_{\mathrm{PLS}} = \{A, B, t_c, m\}$ including four parameters with the first two being linear and the last two being nonlinear. To estimate all these parameters, we define the cost function as the sum of squared errors:

$$F(\mathbf{\theta}_{\mathrm{PLS}}; \mathbf{\Omega}, \mathbf{t}) = \sum_{i=1}^{N} \varepsilon_i^2, \tag{S24}$$

with each residual calculated as:

$$\varepsilon_i = \Omega_i - A - B(t_c - t_i)^m. \tag{S25}$$

The ordinary least squares method amounts to minimizing the cost function (S24) to obtain the estimates for the model parameters:

$$\hat{\mathbf{\theta}}_{\text{PLS}} = \arg\min_{\mathbf{\theta}_{\text{PLS}}} F(\mathbf{\theta}_{\text{PLS}}). \tag{S26}$$

To do so, we enslave the two linear parameters $\{A, B\}$ to the two nonlinear ones $\{t_c, m\}$ to obtain the nonlinear optimization problem:

$$\{\hat{t}_c, \hat{m}\} = \arg\min_{t_c, m} F_1(t_c, m), \tag{S27}$$

with the cost function defined as:

$$F_1(t_c, m) = \min_{A,B} F(t_c, m, A, B) = F(t_c, m, \hat{A}, \hat{B}). \tag{S28}$$

The estimates for parameters $\{A, B\}$ are obtained by solving the optimization problem:

$$\{\hat{A}, \hat{B}\} = \arg\min_{A,B} F(t_c, m, A, B), \tag{S29}$$

which has a unique solution analytically solved from the following system of linear equations:

$$\begin{bmatrix} N & \sum f_i \\ \sum f_i & \sum f_i^2 \end{bmatrix} \begin{bmatrix} \hat{A} \\ \hat{B} \end{bmatrix} = \begin{bmatrix} \sum \Omega_i \\ \sum \Omega_i f_i \end{bmatrix}, \tag{S30}$$

where $f_i = (t_c - t_i)^m$.

The optimization problem (S27) can be further reformulated as:

$$\hat{t}_c = \arg\min_{t_c} F_2(t_c), \tag{S31}$$

with the cost function given by:

$$F_2(t_c) = \min_m F_1(t_c, m) = F_1(t_c, \hat{m}), \tag{S32}$$

and the estimate for parameter m is obtained by solving the optimization problem:

$$\hat{m} = \arg\min_m F_1(t_c, m). \tag{S33}$$

Lagrange regularization for determining the onset of the fitting time window

For a fixed end time T, the optimal start time τ of the time window for calibrating the LPPLS or PLS model can be endogenously detected using the Lagrange regularization approach (28) with the following cost function to minimize:

$$\tilde{F}'(\tau) = \tilde{F}(\tau) - \chi N(\tau), \tag{S34}$$

where χ is the Lagrange parameter, N is the number of observations within the time window $[\tau, T]$, and $\tilde{F}(\tau)$ is the normalized sum of squared residuals given by:

$$\tilde{F}(\tau) = \frac{F}{N(\tau) - n}, \tag{S35}$$

where F is the sum of squared errors given by equation (S13) for the LPPLS fitting or by equation (S24) for the PLS fitting and n is the number of degrees of freedom of the model (i.e., 7 and 4 for the LPPLS and PLS model, respectively). The Lagrange parameter χ can be heuristically approximated by the slope in the linear regression model of $\tilde{F}(\tau)$ with respect to τ.

When comparing the LPPLS and PLS models, we estimate τ based on the LPPLS model to determine the time window for comparison. Alternatively, we can estimate τ based on the PLS model or as the maximum of the τ values from the LPPLS and PLS models, which do not affect our conclusions about the model's superiority.

<u>Goodness-of-fit tests for comparing the LPPLS and PLS models</u>

We employ a set of evaluation metrics to compare the LPPLS and PLS models, including normalized root mean square error (NRMSE), normalized Akaike information criterion (NAIC) and normalized Bayesian information criterion (NBIC) as well as p-values derived from the Wilks likelihood-ratio test, the two-sample Kolmogorov-Smirnov (KS) test, and the two-sample Anderson-Darling (AD) test.

For the time series of N measurements of the observable quantity $\mathbf{\Omega} = \{\Omega_1, \Omega_2, ..., \Omega_N\}$ recorded at time $\mathbf{t} = \{t_1, t_2, ..., t_N\} \in [\tau, T]$, we compute NRMSE as:

$$\text{NRMSE} = \frac{1}{\Omega_N - \Omega_1} \sqrt{\frac{1}{N} F(\mathbf{\theta}; \mathbf{\Omega}, \mathbf{t})}, \tag{S36}$$

where F is the sum of squared errors given by equation (S13) for the LPPLS fitting or by equation (S24) for the PLS fitting.

In the context of ordinary least squares, if the model is well-specified (i.e., it represents the true generative process of the data, with the noise being independent and identically distributed), then the error term $\varepsilon(\mathbf{\theta}; \mathbf{\Omega}, \mathbf{t})$ obeys a zero-mean Gaussian distribution:

$$f(\varepsilon; \sigma^2) = \frac{1}{\sqrt{2\pi\sigma^2}} \exp\left(-\frac{\varepsilon^2}{2\sigma^2}\right), \tag{S37}$$

where σ^2 is the variance. We construct the likelihood function as:

$$L(\mathbf{\theta}, \sigma^2; \mathbf{\Omega}, \mathbf{t}) = \prod_{i=1}^{N} \left[\frac{1}{\sqrt{2\pi\sigma^2}} \exp\left(-\frac{\varepsilon_i^2}{2\sigma^2}\right) \right] = (2\pi\sigma^2)^{-N/2} \exp\left[-\frac{F(\mathbf{\theta}; \mathbf{\Omega}, \mathbf{t})}{2\sigma^2}\right]. \tag{S38}$$

The corresponding log-likelihood function is:

$$\ln L(\mathbf{\theta}, \sigma^2; \mathbf{\Omega}, \mathbf{t}) = -\frac{N}{2} \ln(2\pi\sigma^2) - \frac{F(\mathbf{\theta}; \mathbf{\Omega}, \mathbf{t})}{2\sigma^2}, \tag{S39}$$

with the maximum likelihood estimate for σ^2 given as:

$$\hat{\sigma}^2 = \frac{1}{N} F(\hat{\mathbf{\theta}}; \mathbf{\Omega}, \mathbf{t}), \tag{S40}$$

so that we obtain:

$$\ln L(\hat{\mathbf{\theta}}; \mathbf{\Omega}, \mathbf{t}) = -\frac{N}{2} \left[\ln F(\hat{\mathbf{\theta}}; \mathbf{\Omega}, \mathbf{t}) + \ln\left(\frac{2\pi}{N}\right) + 1 \right]. \tag{S41}$$

We test the null hypothesis H_0 that the observable quantity $\mathbf{\Omega}(\mathbf{t})$ follows the PLS model against the alternative that it follows the LPPLS model. Note that the PLS model is a special case of (or a model nested in) the LPPLS model (i.e., the latter reduces to the former if $C = 0$ or in other words $\mathbf{\theta}_{\text{PLS}}$ is a subset of $\mathbf{\theta}_{\text{LPPLS}}$), Thus, we use the Wilks likelihood ratio test which is powerful and widely applicable, especially for nested models, because it relies on comparing the likelihoods of the two models, which is a robust way of assessing model fit. It has desirable properties under certain

conditions, such as asymptotically following a chi-squared distribution under the null hypothesis, which makes it convenient for deriving *p*-values and making decisions about model selection. The corresponding likelihood-ratio test statistic is defined as:

$$\Lambda = -2\left[\ln L(\hat{\mathbf{\theta}}_{\text{PLS}};\mathbf{\Omega},\mathbf{t}) - \ln L(\hat{\mathbf{\theta}}_{\text{LPPLS}};\mathbf{\Omega},\mathbf{t})\right] = N\ln\frac{F(\hat{\mathbf{\theta}}_{\text{PLS}};\mathbf{\Omega},\mathbf{t})}{F(\hat{\mathbf{\theta}}_{\text{LPPLS}};\mathbf{\Omega},\mathbf{t})}, \qquad (S42)$$

which converges asymptotically to a chi-squared distribution (with $\kappa = 3$ degrees of freedom, which is the difference in the number of parameters between the LPPLS and PLS models), if H_0 happens to be true. For the finite sample here with N number of data points, the distribution of the likelihood-ratio test statistic is unknown. Here, we perform Monte Carlo simulations (1000 runs) to estimate the *p*-value of the null hypothesis as the fraction of exceedances of the test statistic of simulated data compared to that of the actual data. If the *p*-value is smaller than the prescribed significance level (e.g., 0.05), the null hypothesis is rejected.

We also perform a two-sample KS test and AD test on the null hypothesis that the probability distributions of the LPPLS and PLS residuals do not differ. If the *p*-value is smaller than the prescribed significance level, the null hypothesis is rejected, meaning that the residuals of the LPPLS and PLS models are not from the same distribution.

Furthermore, we estimate the relative model quality based on the NAIC and NBIC values calculated as (*55*):

$$\text{NAIC} = \frac{2\kappa - 2\ln L(\hat{\mathbf{\theta}},\hat{\sigma}^2;\mathbf{\Omega},\mathbf{t})}{N} = \frac{2\kappa}{N} + \ln F(\hat{\mathbf{\theta}};\mathbf{\Omega},\mathbf{t}) + \ln\left(\frac{2\pi}{N}\right) + 1, \qquad (S43)$$

$$\text{NBIC} = \frac{\kappa\ln N - 2\ln L(\hat{\mathbf{\theta}},\hat{\sigma}^2;\mathbf{\Omega},\mathbf{t})}{N} = \frac{\kappa\ln N}{N} + \ln F(\hat{\mathbf{\theta}};\mathbf{\Omega},\mathbf{t}) + \ln\left(\frac{2\pi}{N}\right) + 1, \qquad (S44)$$

which reward the goodness-of-fit while introducing a penalty term for the number of parameters.

Data acquisition approach

In this study, we have compiled a large dataset of >100 geohazard events of landslides, rockbursts, glacier breakoffs, and volcanic eruptions (see Tables S1-S4). These data were retrieved through two major ways: (1) exported directly from the monitoring system and obtained from either published dataset/database or from the authors (indicated as "Original"), and (2) digitized from figures in published literature using digitization software (indicated as "Digitized").

The data of 10 cases (Agoyama, Arvigo, Galterengraben, Grabengufer, Hogarth, Kagemori, La Saxe, Nevis Bluff, Vajont, and Weissmiess) were extracted from the published dataset (https://mediatum.ub.tum.de/1688868) (*15*), where the data of 4 cases are "Original" and the data of other 6 cases are "Digitized". Most volcano data are downloaded from the WOVOdat platform (https://www.wovodat.org), which is a publicly accessible database of volcanic unrest (*56*). For most of digitized data in our dataset, we employ the software PlotDigitizer Pro (https://plotdigitizer.com/) to retrieve the data from the published literature. The references for all the data are indicated in Tables S1-S4.
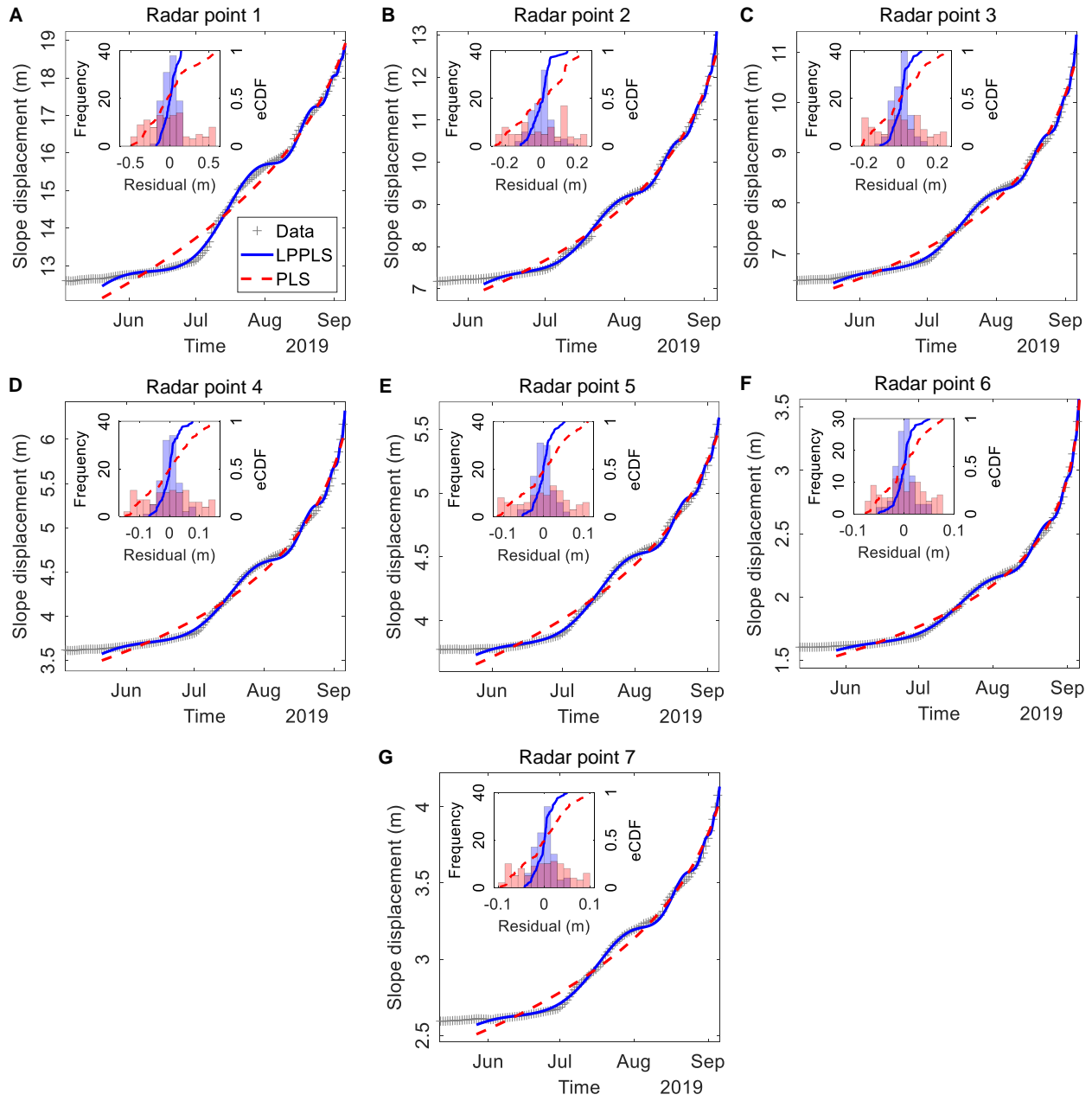
Fig. S1. Comparison of the LPPLS versus PLS models in fitting the data of the Veslemannen landslide.
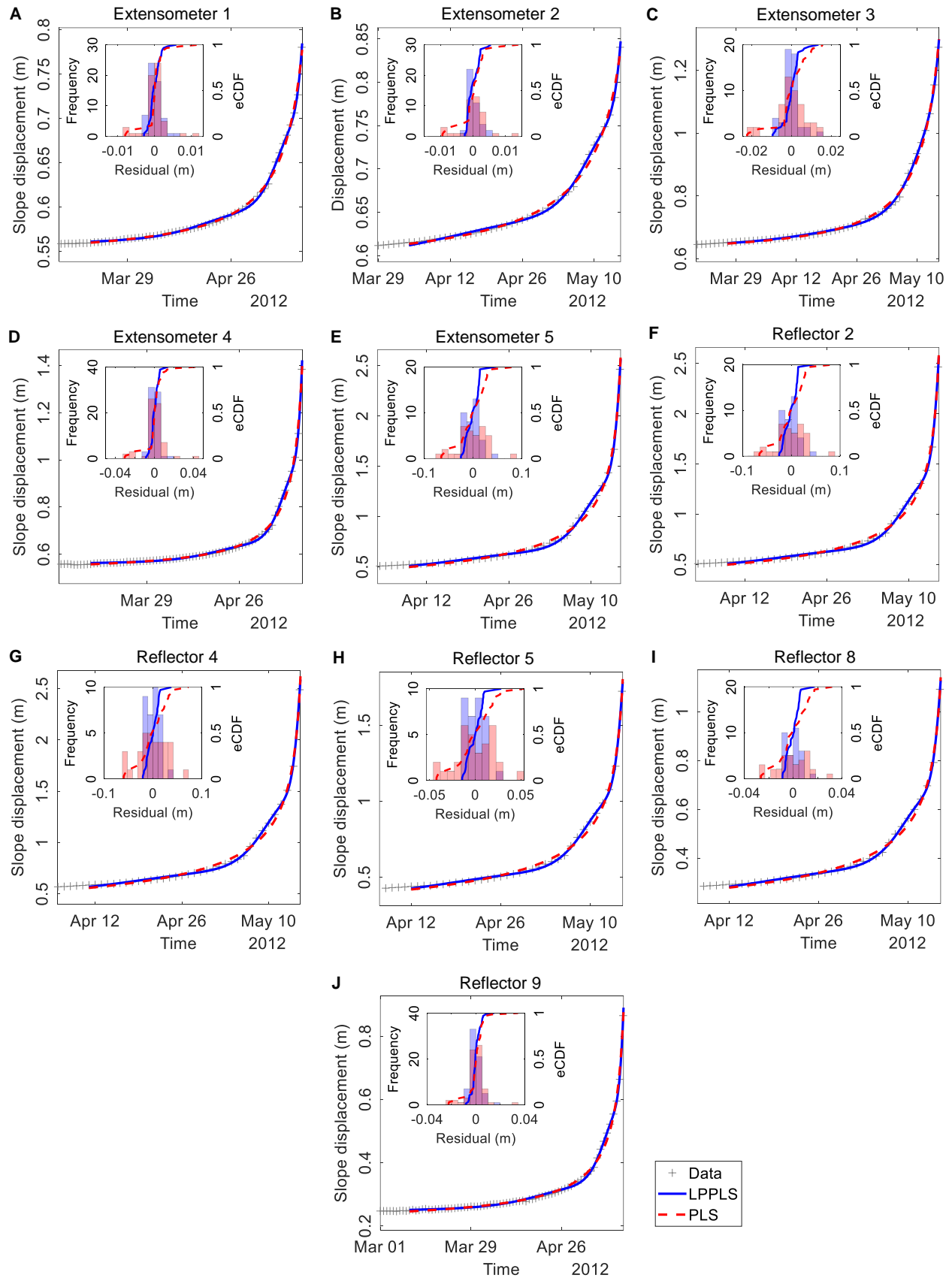
Fig. S2. Comparison of the LPPLS versus PLS models in fitting the data of the Preonzo landslide.
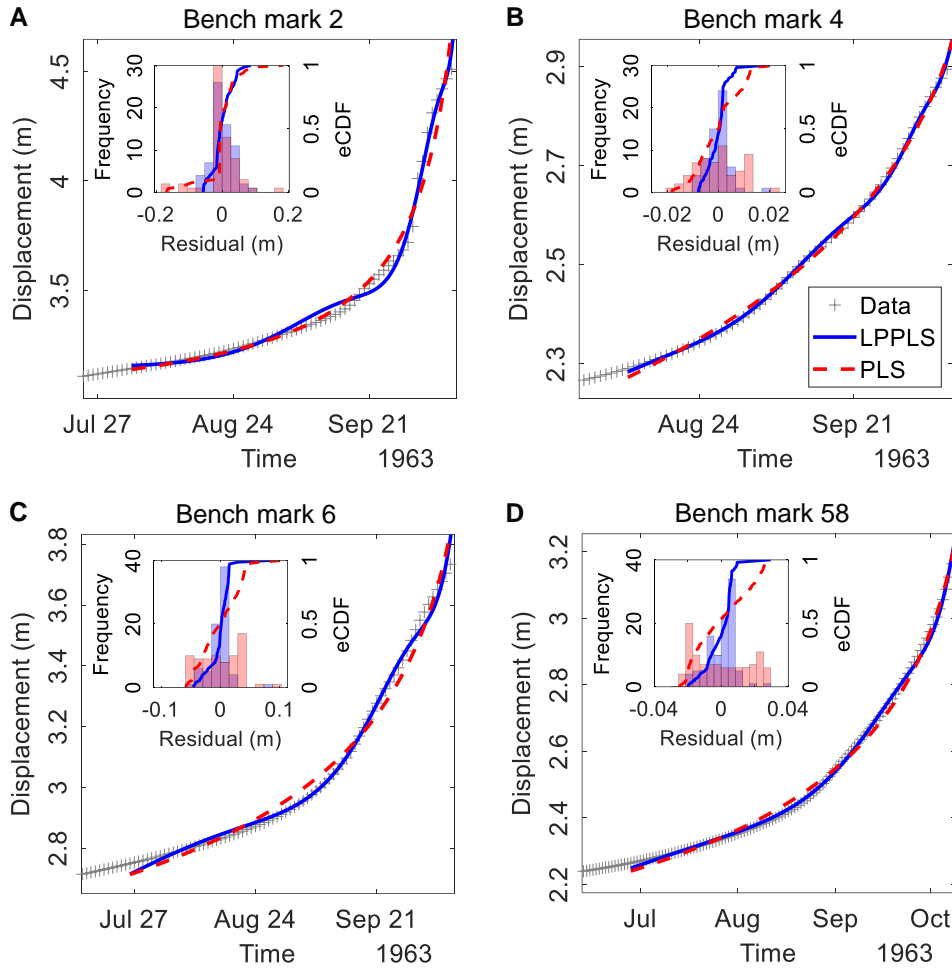
Fig. S3. Comparison of the LPPLS versus PLS models in fitting the data of the Vajont landslide.
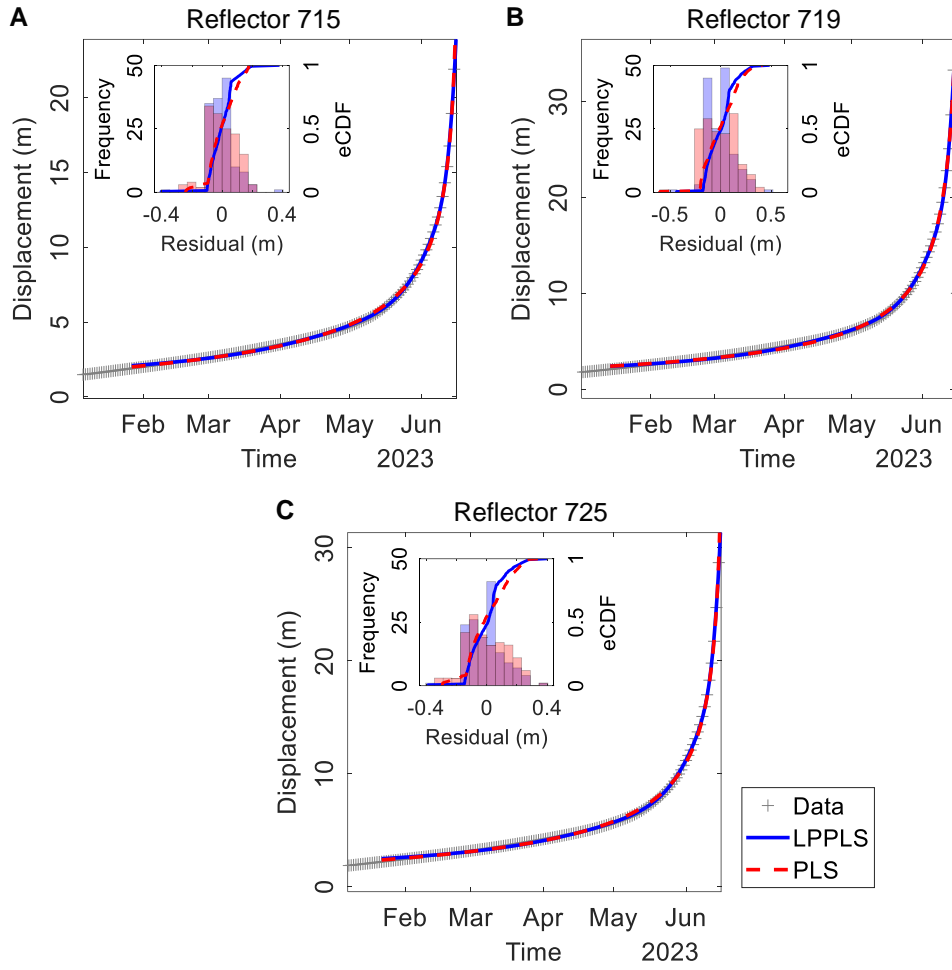
Fig. S4. Comparison of the LPPLS versus PLS models in fitting the reflector monitoring data of the Brienz/Brinzauls landslide.
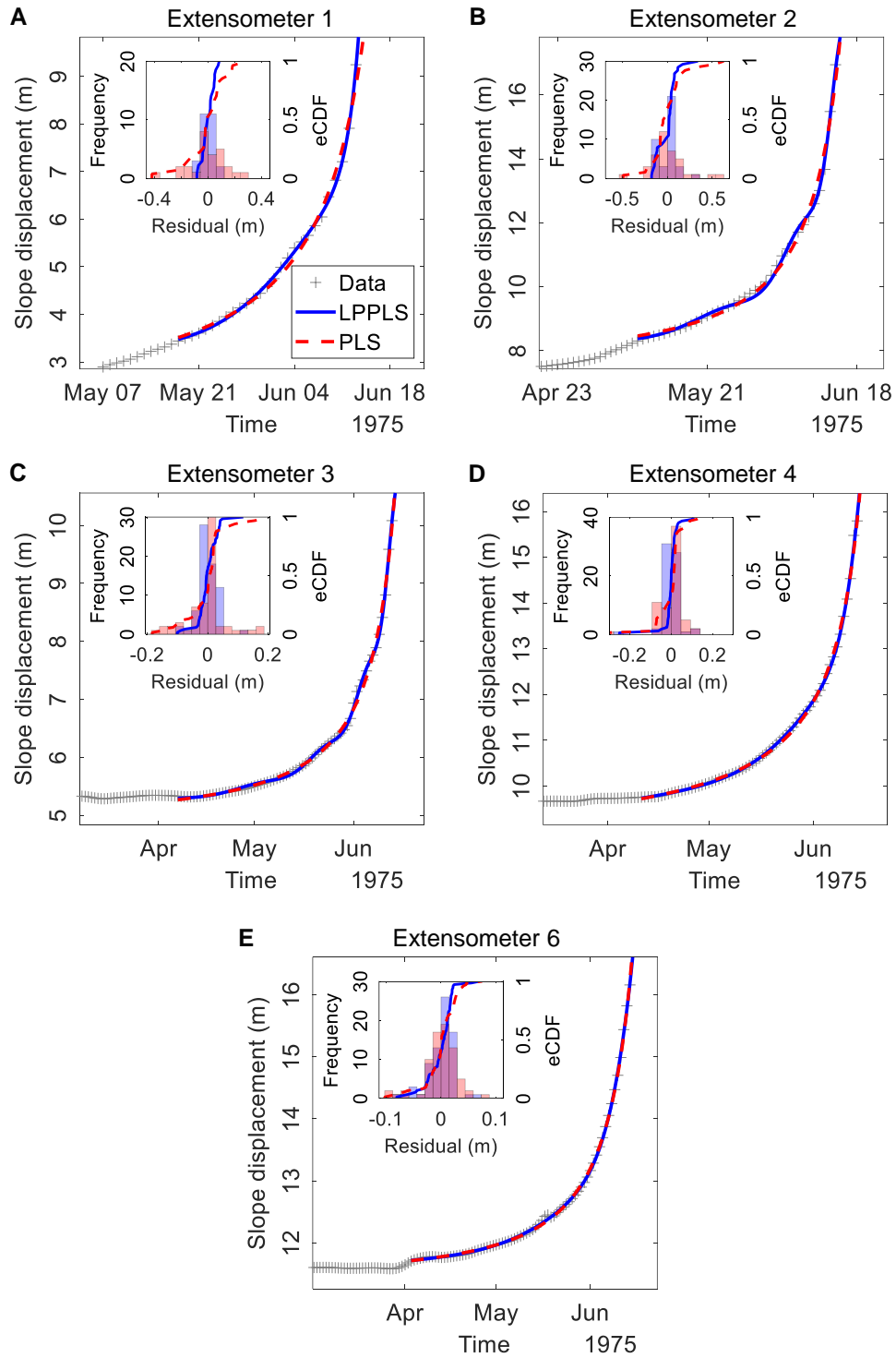
Fig. S5. Comparison of the LPPLS versus PLS models in fitting the data of the Hogarth landslide.
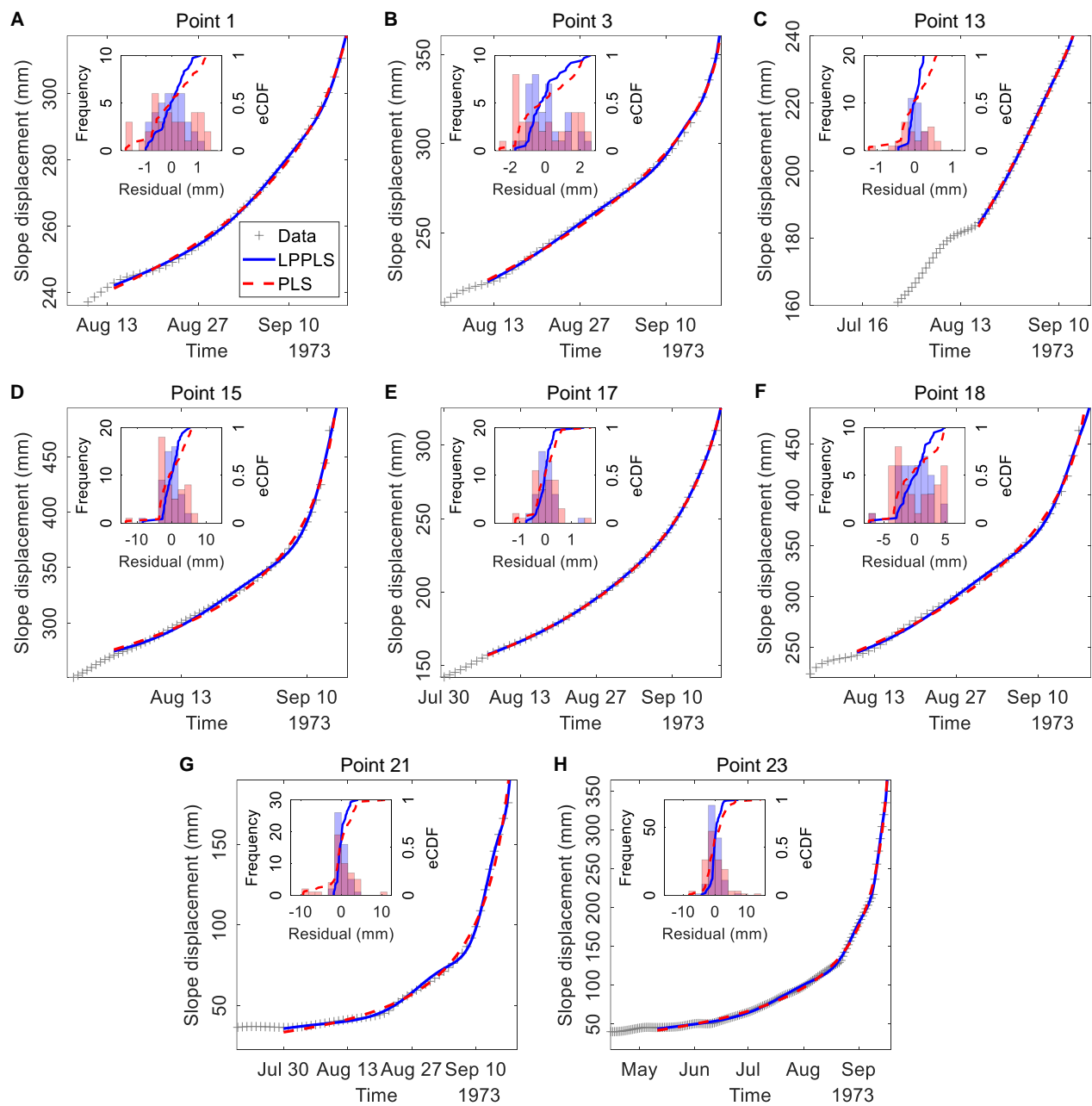
Fig. S6. Comparison of the LPPLS versus PLS models in fitting the data of the Kagemori landslide.
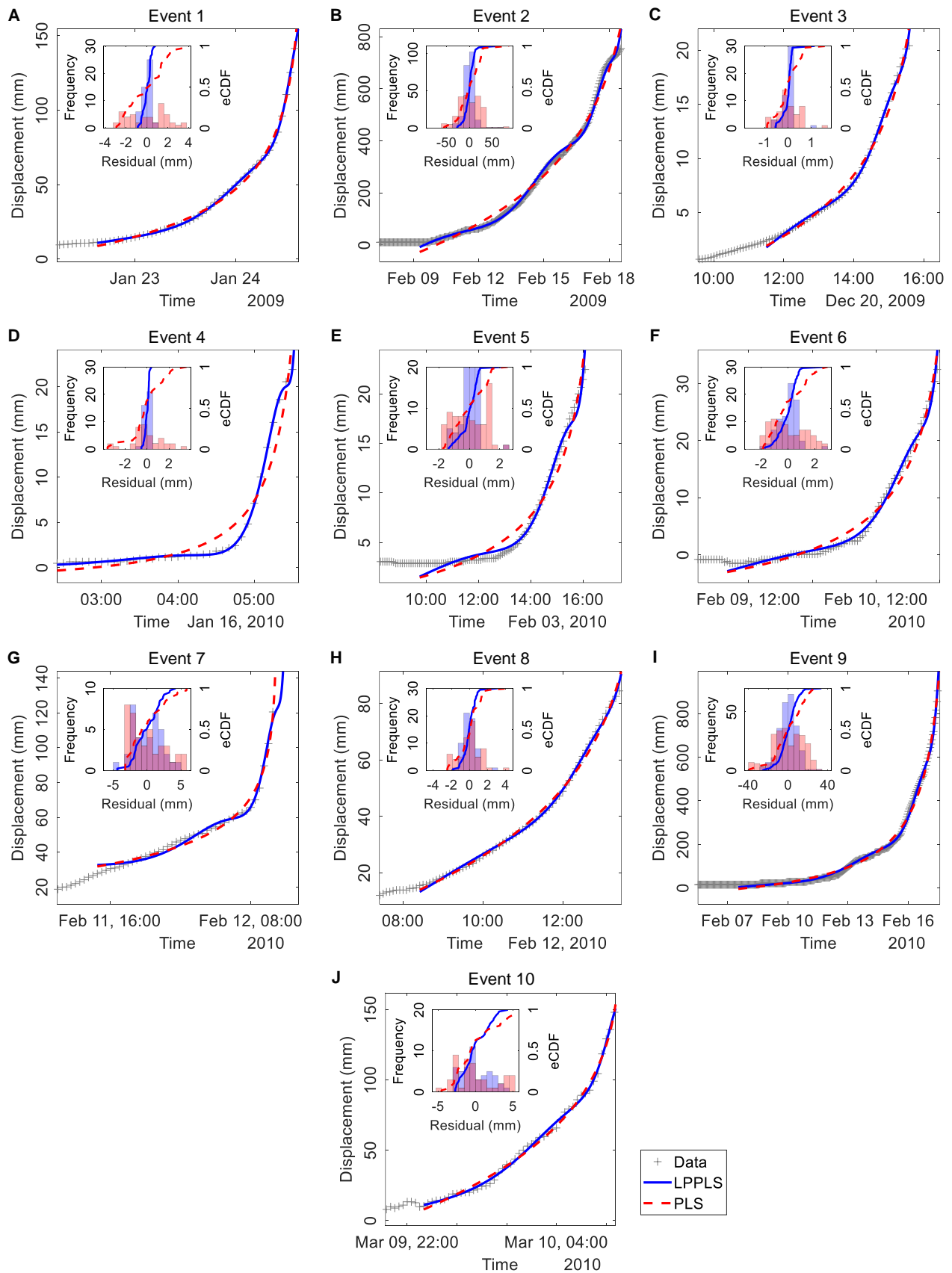
Fig. S7. Comparison of the LPPLS versus PLS models in fitting the monitoring data of a road slope.
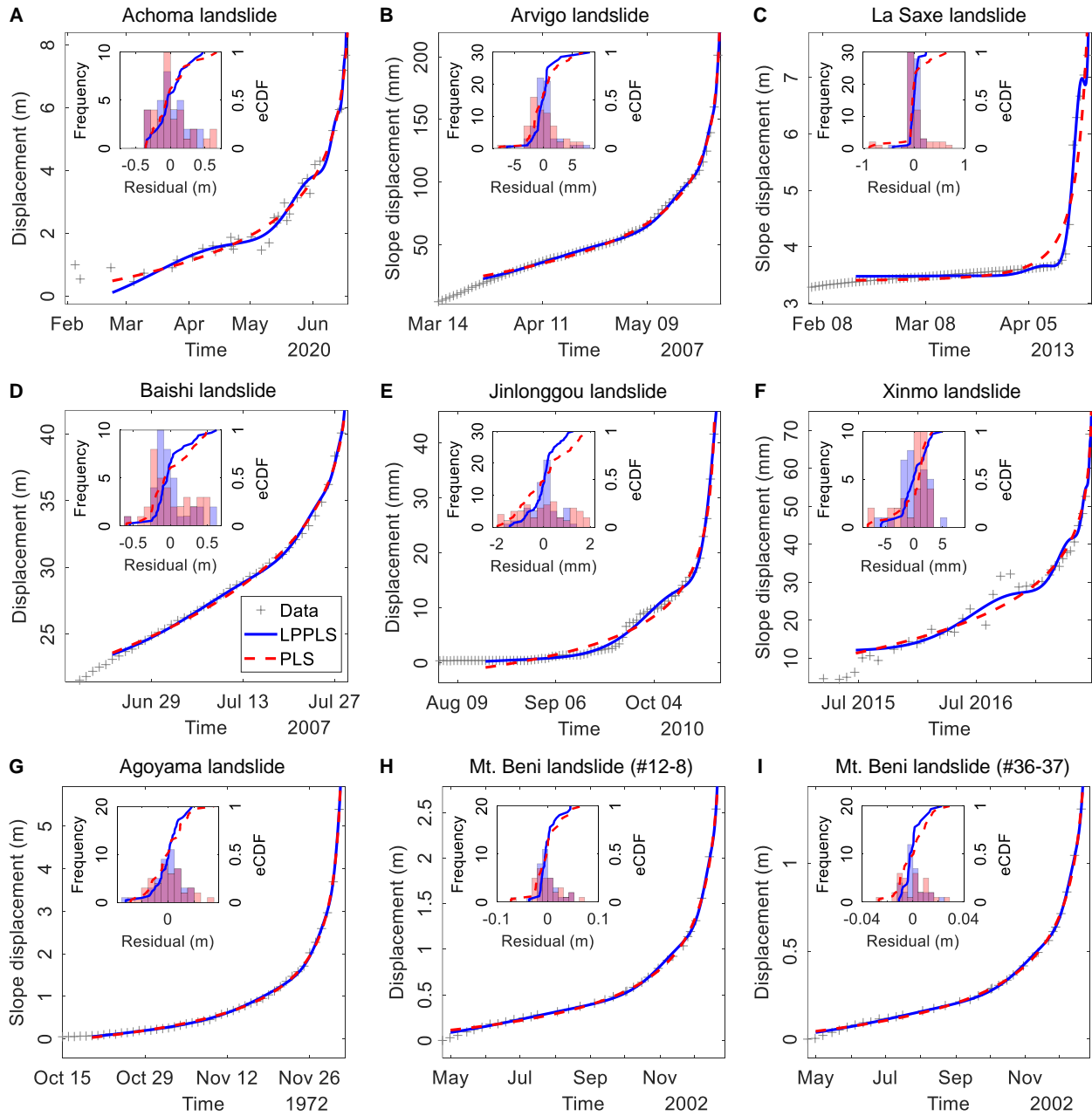
Fig. S8. Comparison of the LPPLS versus PLS models in fitting the data of various landslides in rock.
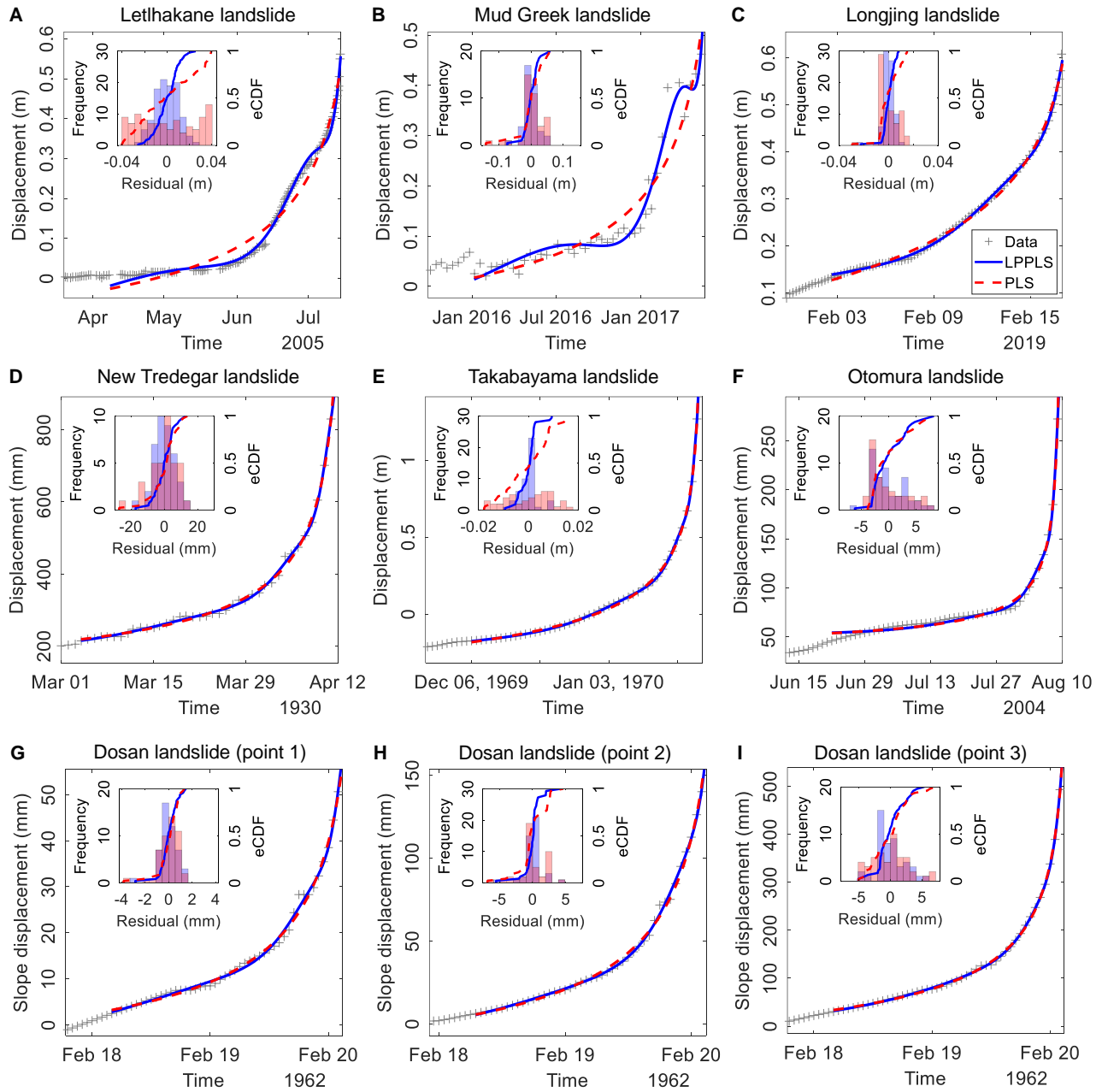
Fig. S9. Comparison of the LPPLS versus PLS models in fitting the data of various landslides in rock.
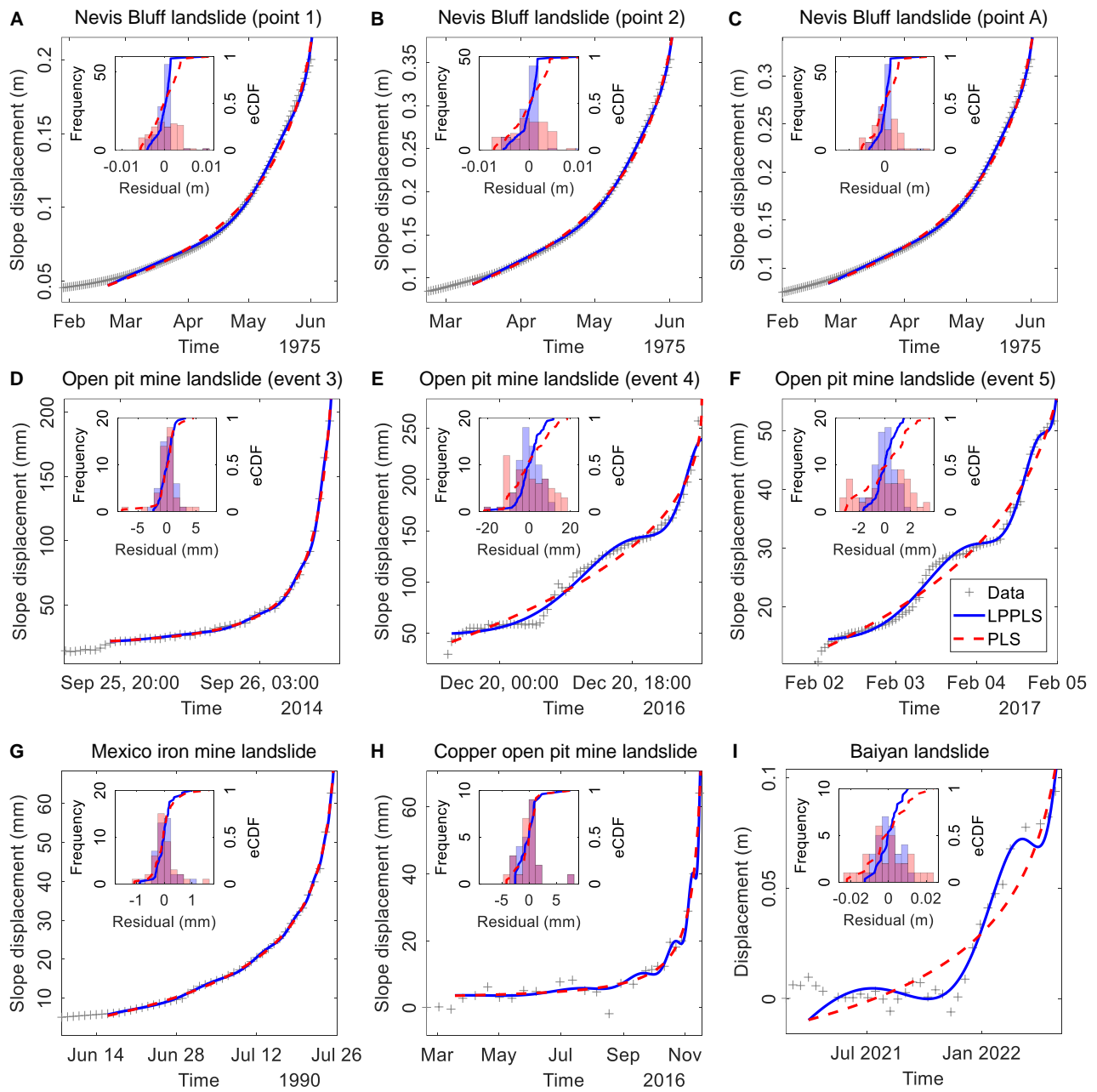
Fig. S10. Comparison of the LPPLS versus PLS models in fitting the data of various landslides in rock.
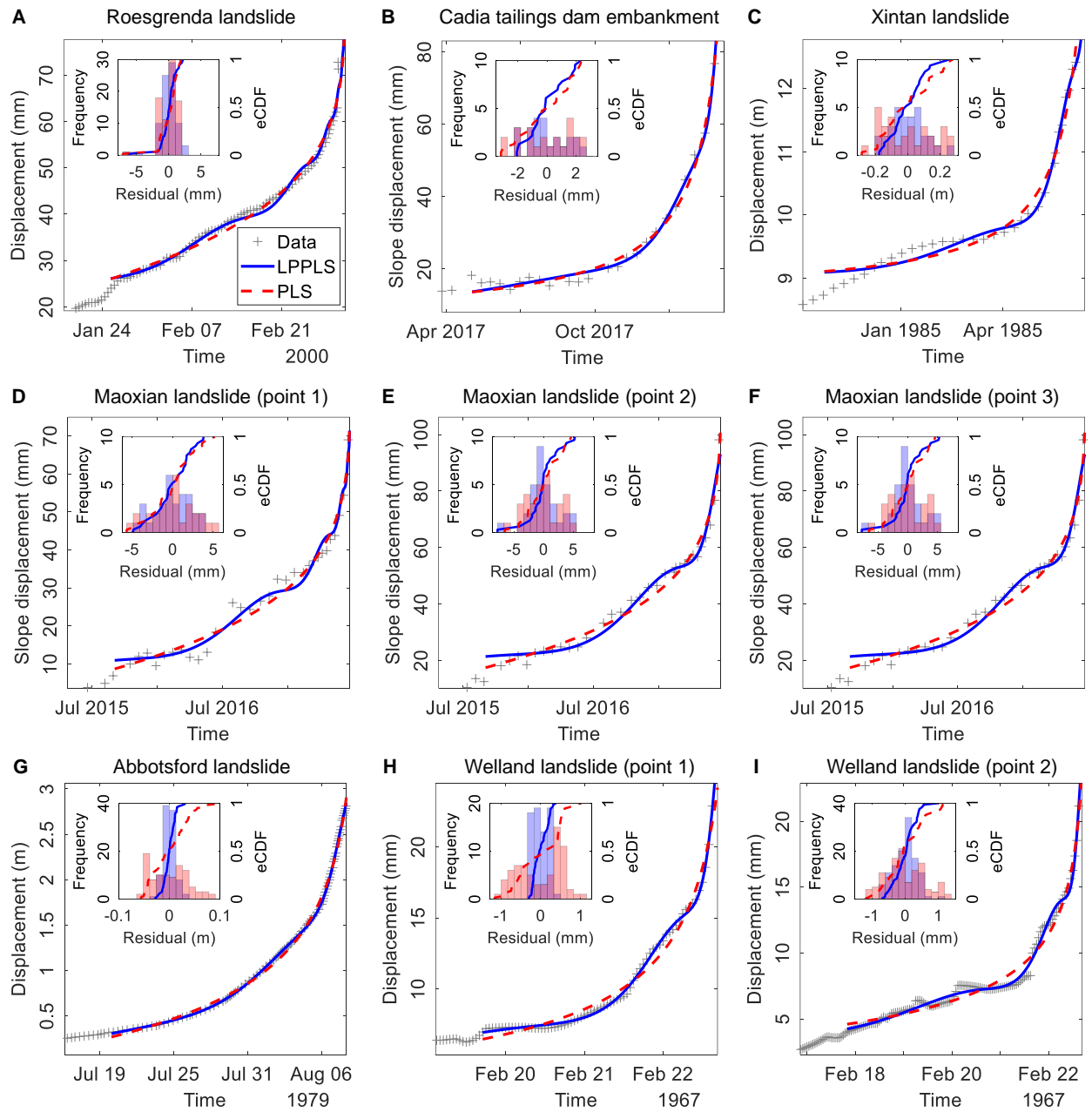
Fig. S11. Comparison of the LPPLS versus PLS models in fitting the data of various landslides in soil.
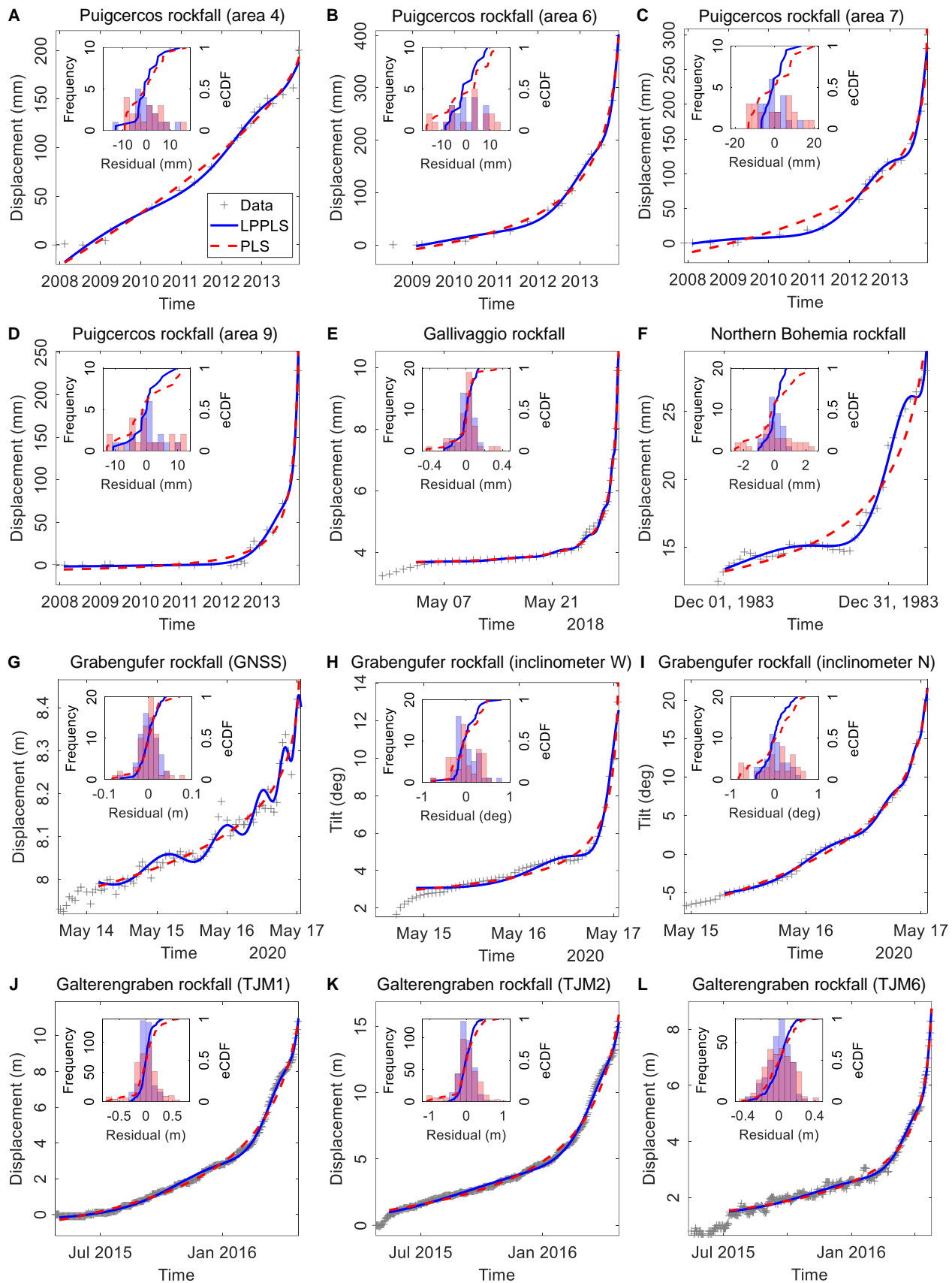
Fig. S12. Comparison of the LPPLS versus PLS models in fitting the data of various rockfalls.
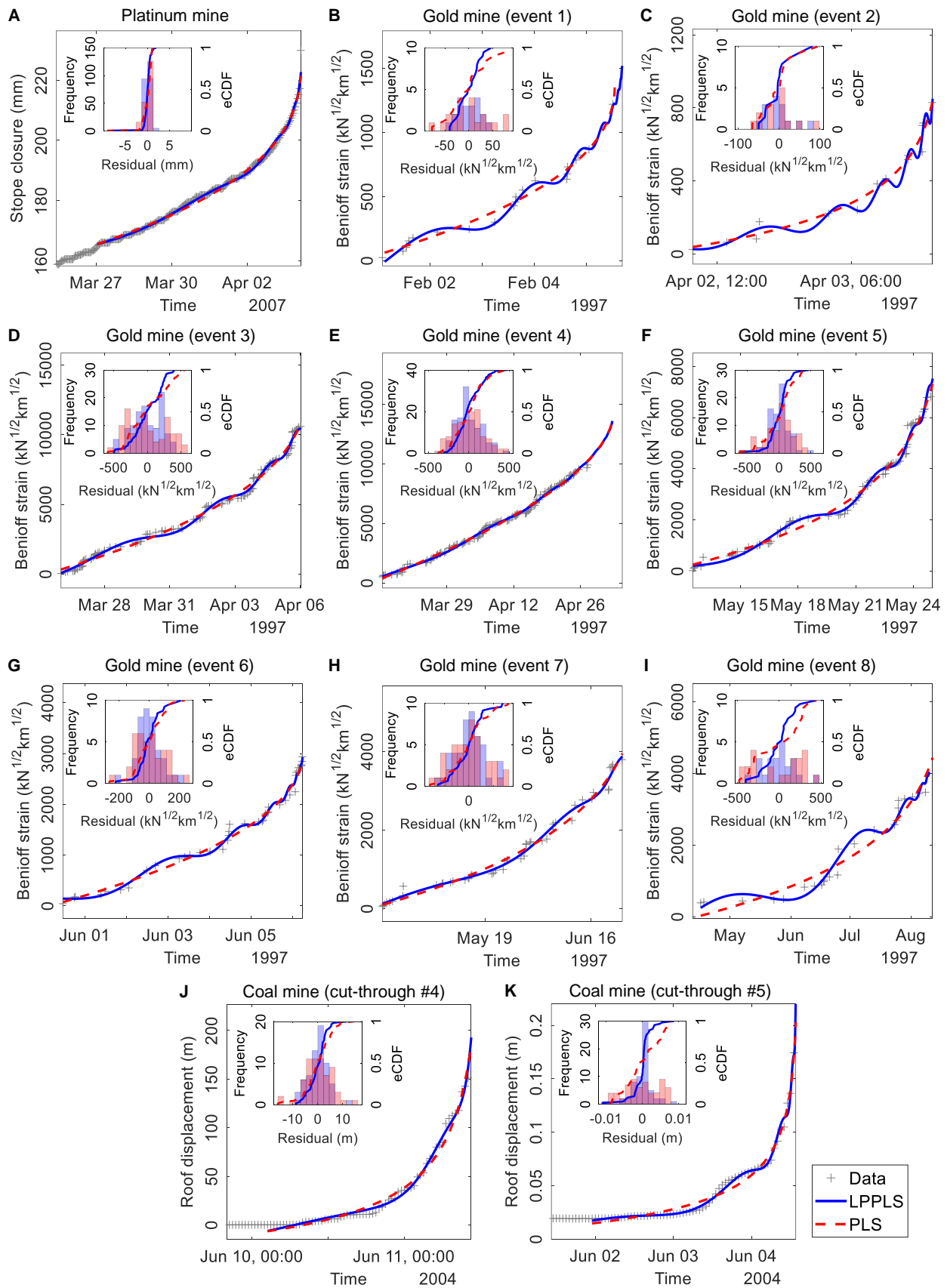
Fig. S13. Comparison of the LPPLS versus PLS models in fitting the data of various rockbursts.
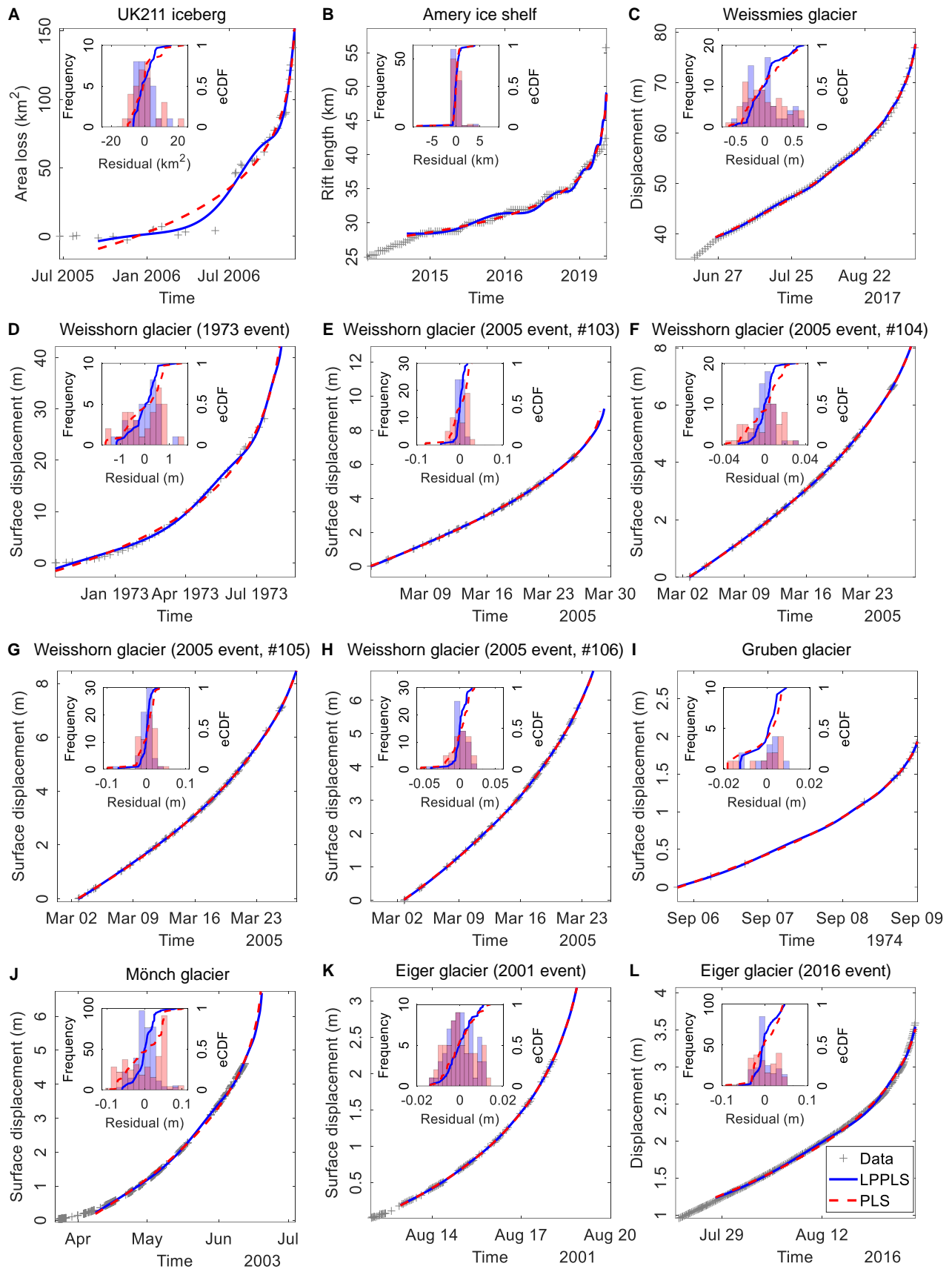
Fig. S14. Comparison of the LPPLS versus PLS models in fitting the data of various glaciers.
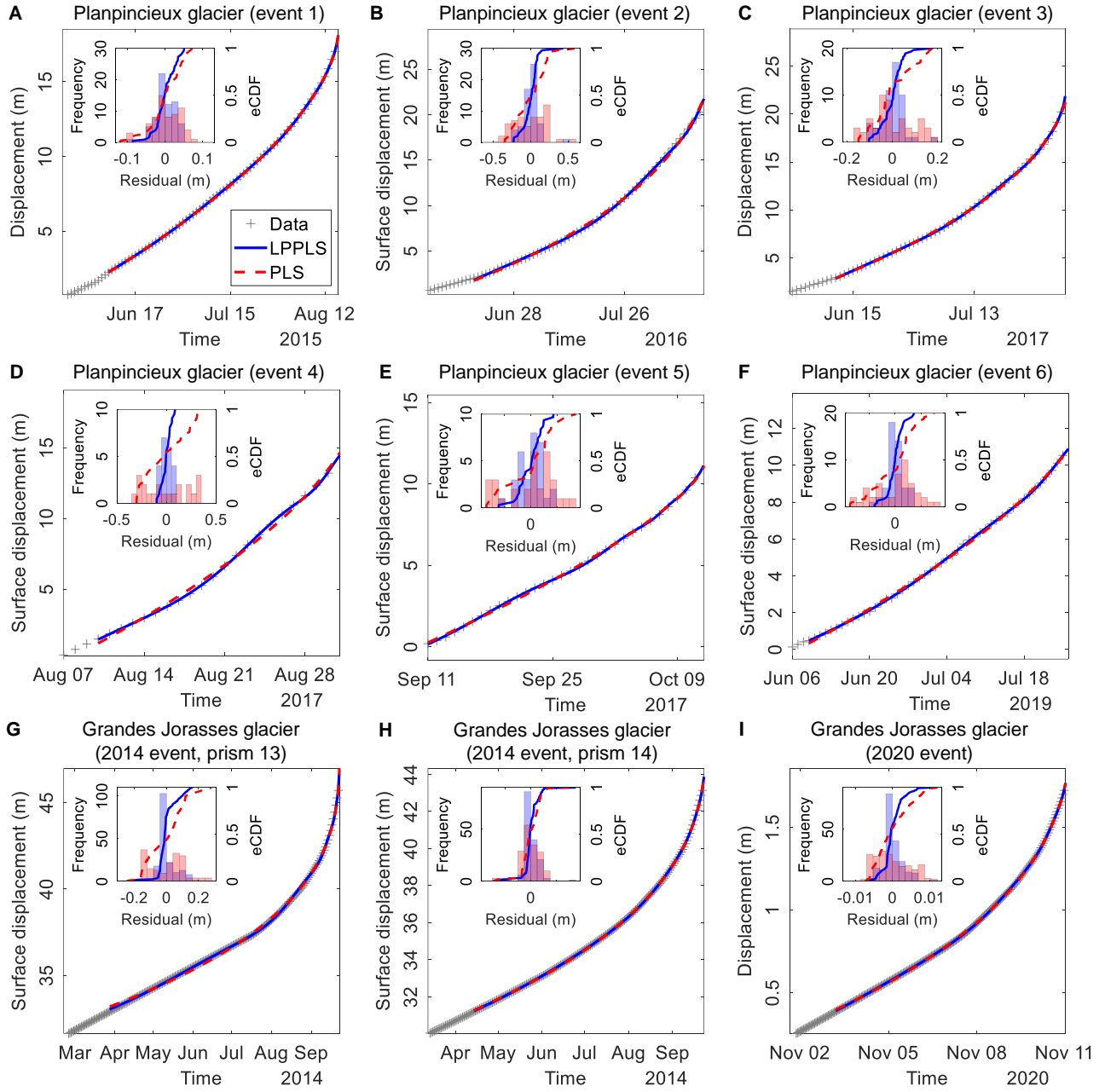
Fig. S15. Comparison of the LPPLS versus PLS models in fitting the data of multiple breakoff events of the Planpincieux glacier and Grandes Jorasses glacier.
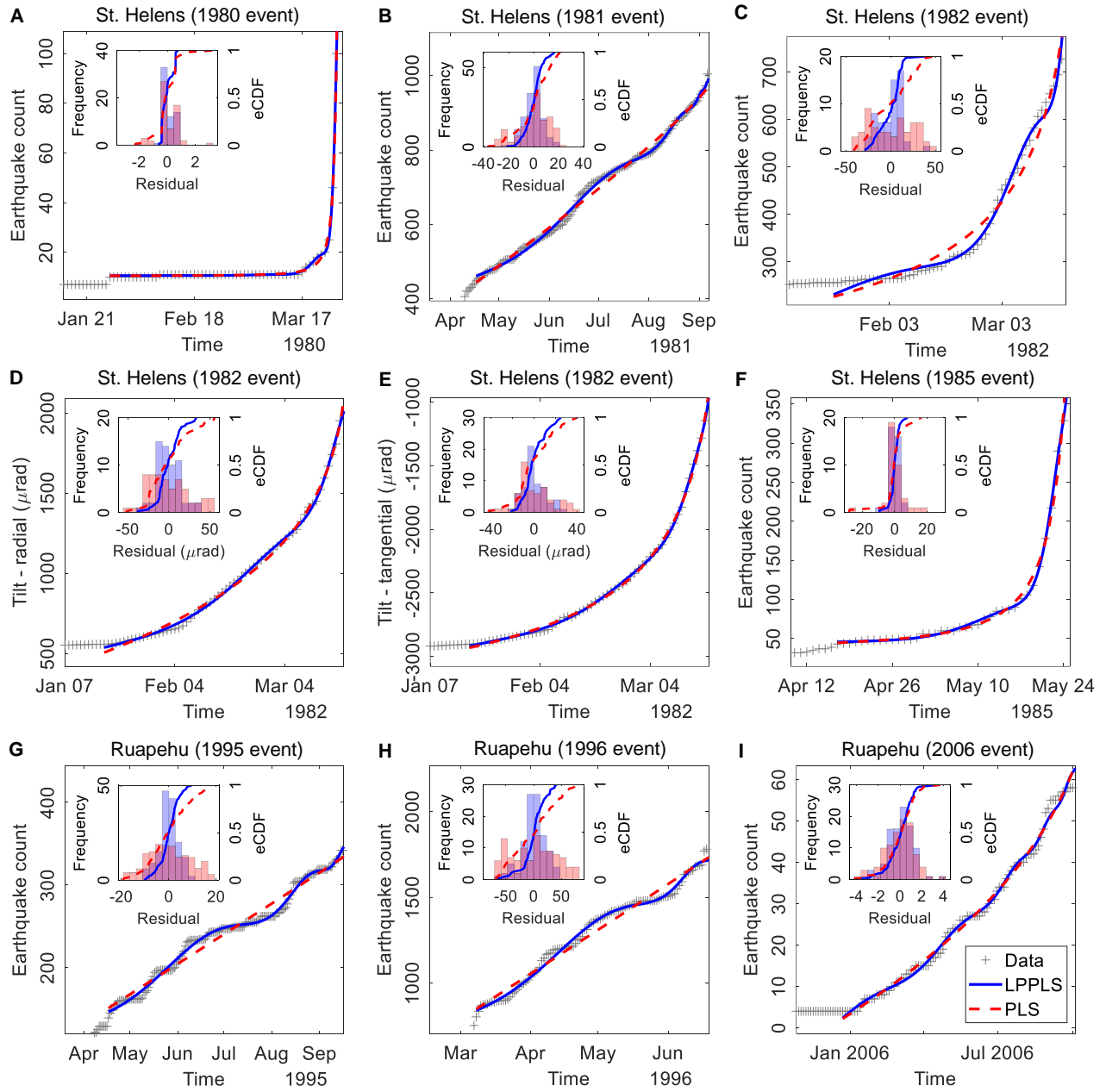
Fig. S16. Comparison of the LPPLS versus PLS models in fitting the data of multiple eruption events at the Mount St. Helen volcano and the Ruapehu volcano.
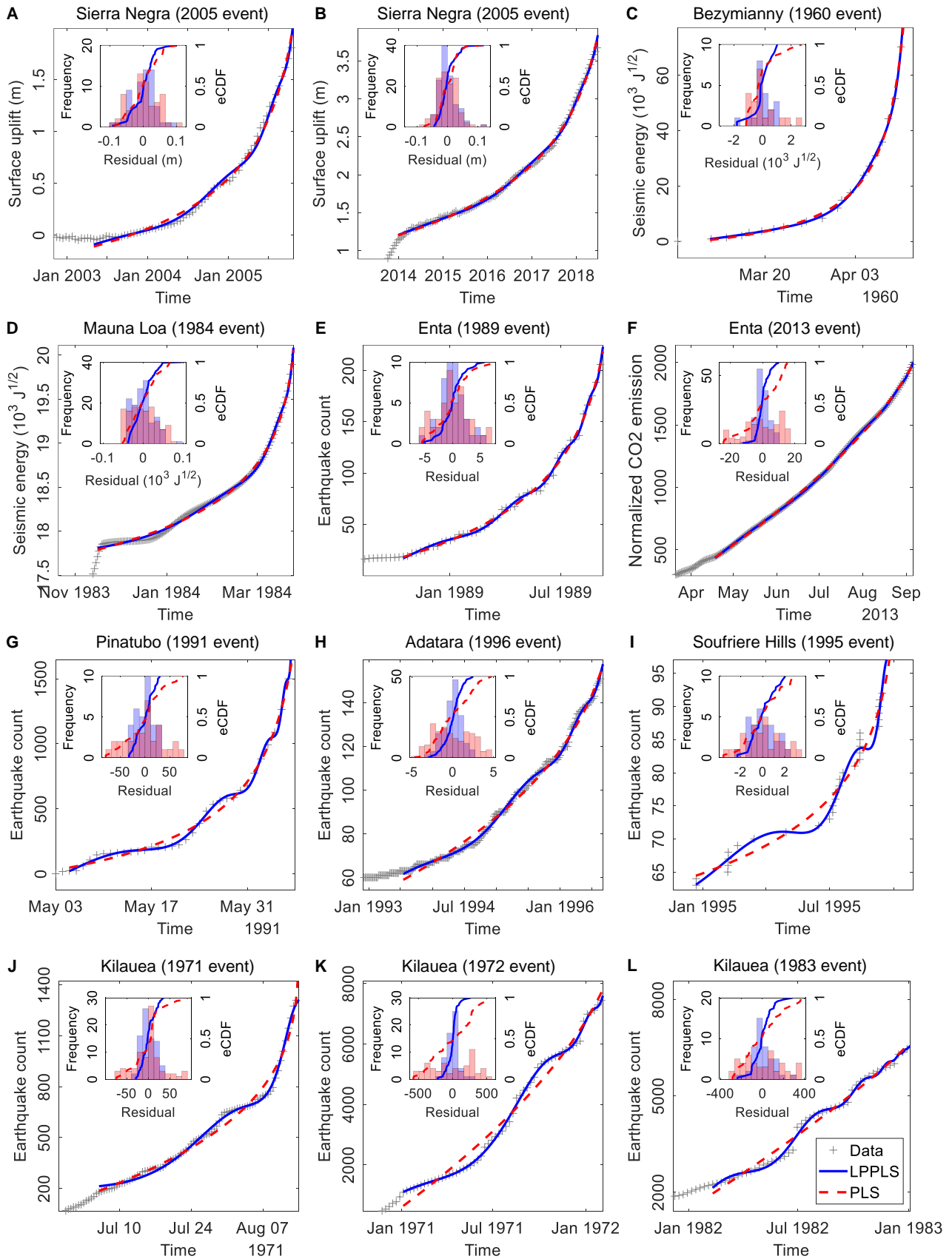
Fig. S17. Comparison of the LPPLS versus PLS models in fitting the data of various volcanoes.
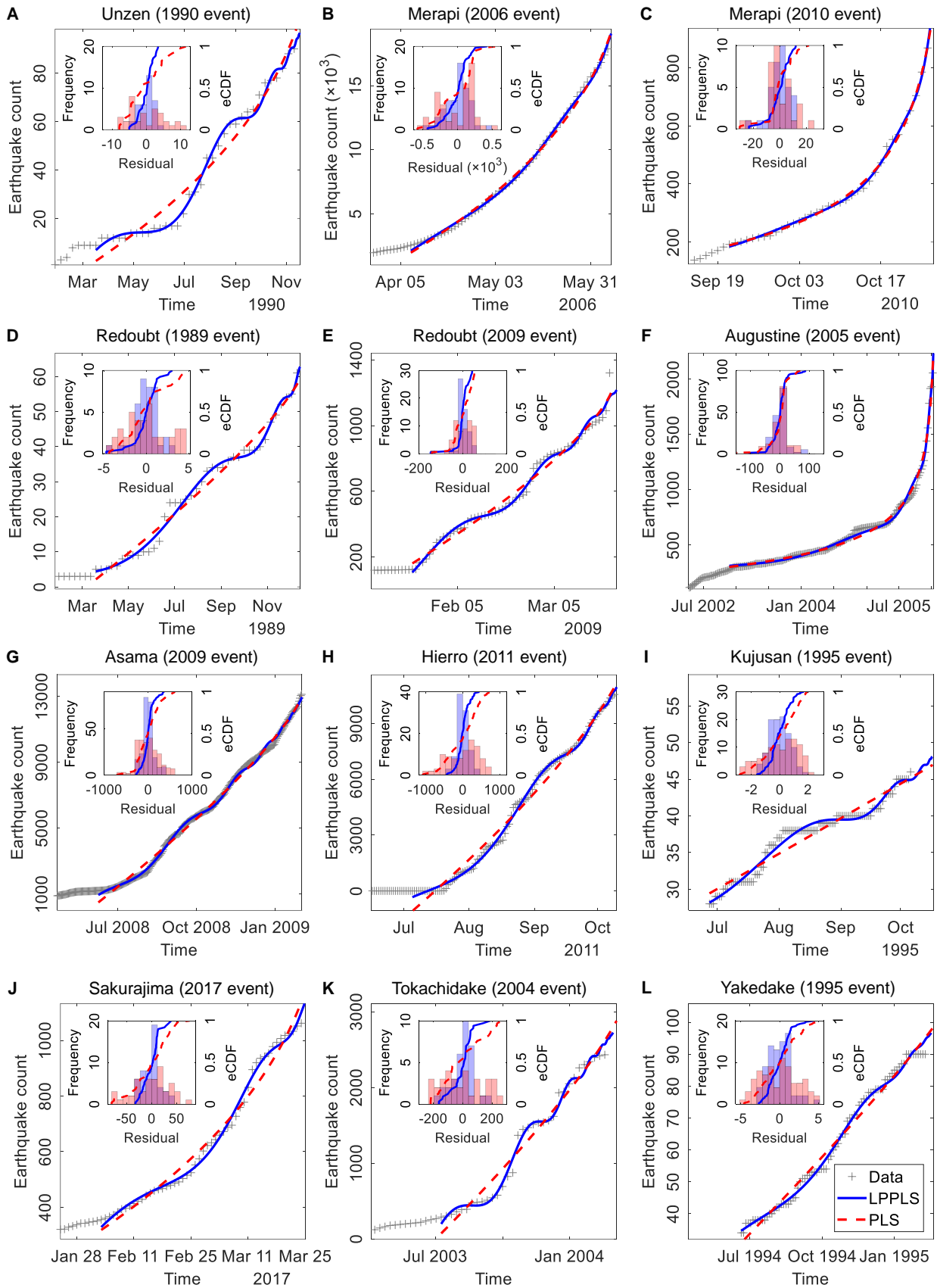
Fig. S18. Comparison of the LPPLS versus PLS models in fitting the data of various volcanoes.

Table S1. Landslide cases (49 events in total).

Site	Location	Type	Material	Failure time	Volume (m^3)	Monitoring method	Data source	Reference
Abbotsford	New Zealand	Soilslide	Clay	1979-08-08	5×10^6	Survey lines	Digitized	(*57*)
Achoma	Peru	Rock-soilslide	Lacustrine sediments	2020-06-16	5.4×10^6	Optical satellites	Digitized	(*36*)
Agoyama	Japan	Rockslide	Tuffaceous sandstone	1972-12-02	Unknown	Geodetic bench marks	Digitized	(*58*)
Arvigo	Switzerland	Topple / rockslide	Gneiss	2007-05-28	2×10^5	Telejointmeter	Original	(*15*)
Baishi	China	Rockslide	Phyllite	2007-07-28	2×10^6	Total station with reflectors	Digitized	(*59*)
Baiyan	China	Rockslide	Limestone	2022-05-08	2.5×10^4	Satellite-based InSAR	Digitized	(*60*)
Brienz / Brinzauls	Switzerland	Rockslide	Flysch, schists, dolomite	2023-06-15	1.2×10^6	Total station with reflectors	Original	(*61*)
Cadia	Australia	Soilslide	Earthfill materials	2018-03-09	7.2×10^4	Satellite-based InSAR	Digitized	(*62*)
Copper open pit	Undisclosed	Rockslide	Limestone, spilite	2016-11-17	6.4×10^5	Satellite-based InSAR	Digitized	(*62*)
Dosan	Japan	Rockslide	Schist	1962-02-20	6×10^4	Crack meter	Digitized	(*63*)
Gallivaggio	Italy	Rockfall	Granite	2018-05-29	5×10^3	Ground-based InSAR	Digitized	(*40*)
Galterengraben	Switzerland	Rockfall	Sandstone	2016-04-24	2.5×10^3	Telejointmeter	Original	(*15*)
Grabengufer	Switzerland	Rockfall	Rock & ice	2020-05-17	5×10^2	GNSS & inclinometer	Original	(*64*)
Hogarth	Canada	Topple	Diorite	1975-06-23	2×10^5	Extensometers	Digitized	(*65*)
Iron mine	Mexico	Rockslide	Rock	1990-07-26	Unknown	Total station with reflectors	Digitized	(*66*)
Jinlonggou	China	Rockslide	Syenite & basalt	2010-10-23	2×10^5	Extensometer	Digitized	(*67*)
Kagemori	Japan	Rockslide	Limestone	1973-09-20	3×10^5-4×10^5	Measuring tapes	Digitized	(*68*)
La Saxe	Italy	Rockslide	Meta-sedimentary sequences	2013-04-21	5×10^2-1×10^3	Total station with reflectors	Original	(*69*)
Letlhakane diamond mine	Botswana	Rockslide	Sandstone	2005-07-14	2.3×10^5	Total station with reflectors	Digitized	(*70*)
Longjing	China	Rockslide	Dolomite & limestone	2019-02-17	1.4×10^6	Extensometers	Digitized	(*71*)

Table S1 (continued). Landslide cases (49 events in total).

Site	Location	Type	Material	Failure time	Volume (m^3)	Monitoring method	Data source	Reference
Maoxian	China	Soilslide	Soil	2017-06-24	1.5×10^7	Satellite-based InSAR	Digitized	(*72*)
Mt. Beni	Italy	Rockslide	Basalt & limestone	2002-12-28	5.0×10^5	Distometric benchmarks	Digitized	(*73*)
Mud Greek	USA	Rockslide	Shale, sandstone, sediments	2017-05-20	3×10^6	Satellite-based InSAR	Digitized	(*74*)
Nevis Bluff	New Zealand	Flexural topple / rockslide	Schist	1975-06-14	3.2×10^4	Survey markers	Digitized	(*75*)
New Tredegar	UK	Rockslide	Sandstone	1930-04-12	Unknown	Unspecified	Digitized	(*76*)
Northern Bohemia	Czech Republic	Rockfall	Sandstone	1984-01-07	1.4×10^3	Extensometers	Digitized	(*77*)
Open pit mine (event 3)	Undisclosed	Rockslide	Anorthosite	2014-09-26	6×10^2	Ground-based InSAR	Digitized	(*78*)
Open pit mine (event 4)	Undisclosed	Rockslide	Anorthosite	2014-2017	3×10^3	Ground-based InSAR	Digitized	(*78*)
Open pit mine (event 5)	Undisclosed	Topple	Anorthosite	2017-02-05	4×10^3	Ground-based InSAR	Digitized	(*78*)
Otomura	Japan	Rockslide	Sandstone & shale	2004-08-10	2×10^5	Extensometers	Digitized	(*79*)
Preonzo	Switzerland	Rockslide	Gneiss	2012-05-15	2.1×10^5	Extensometers & total station with reflectors	Original	(*35*)
Puigcercós	Spain	Rockfall	Marl, silt, sandstone, limestone	2013-12-03	1×10^3	LiDAR	Digitized	(*39*)
Road slope (event 1)	Undisclosed	Rockslide	Mobilized gneiss	2009-01-24	3×10^2	Ground-based InSAR	Digitized	(*80*)
Road slope (event 2)	Undisclosed	Flow	Colluvium	2009-02-18	1.4×10^1	Ground-based InSAR	Digitized	(*80*)
Road slope (event 3)	Undisclosed	Soilslide	Colluvium & beton	2009-12-20	1.6×10^2	Ground-based InSAR	Digitized	(*80*)
Road slope (event 4)	Undisclosed	Soilslide	Colluvium & beton	2010-01-16	2×10^2	Ground-based InSAR	Digitized	(*80*)
Road slope (event 5)	Undisclosed	Soilslide	Colluvium & beton	2009-02-03	8×10^1	Ground-based InSAR	Digitized	(*80*)
Road slope (event 6)	Undisclosed	Soilslide	Colluvium & beton	2010-02-11	5×10^2	Ground-based InSAR	Digitized	(*80*)
Road slope (event 7)	Undisclosed	Flow	Mobilized & altered gneiss	2010-02-12	2×10^2	Ground-based InSAR	Digitized	(*80*)
Road slope (event 8)	Undisclosed	Rockslide	Colluvium & beton	2010-02-12	3×10^2	Ground-based InSAR	Digitized	(*80*)

Table S1 (continued). Landslide cases (49 events in total).

Site	Location	Type	Material	Failure time	Volume (m^3)	Monitoring method	Data source	Reference
Road slope (event 9)	Undisclosed	Rockslide	Mobilized & altered gneiss	2010-02-17	8×10^1	Ground-based InSAR	Digitized	(*80*)
Road slope (event 10)	Undisclosed	Rockslide	Mobilized & altered gneiss	2010-03-10	1.5×10^2	Ground-based InSAR	Digitized	(*80*)
Roesgrenda	Norway	Soilslide	Quick clay	2000-03-02	2×10^3	Extensometers	Digitized	(*38*)
Takabayama	Japan	Rockslide	Mudstone, sandstone	1970-01-22	5×10^3	Extensometers	Digitized	(*81*)
Vajont	Italy	Rockslide	Limestone	1963-10-09	2.7×10^8	Geodetic bench marks	Digitized	(*37*)
Veslemannen	Norway	Rockslide	Gneiss	2019-09-05	5.4×10^4	Ground-based InSAR	Original	(*30*)
Welland	Canada	Soilslide	Clay	1967-02-22	5×10^2	Extensometers	Digitized	(*82*)
Xinmo	China	Rockslide	Sandstone, phyllite	2017-06-24	1.3×10^7	Satellite-based InSAR	Digitized	(*62*)
Xintan	China	Rockslide	Sediments	1985-06-12	3×10^7	Geodetic bench marks	Digitized	(*83*)

Note: InSAR - Interferometric Synthetic Aperture Radar; LiDAR - Light Detection and Ranging; GNSS - Global navigation satellite system.

Table S2. Rockburst cases (11 events in total).

Site	Location	Material	Failure time	Monitoring method	Data source	Reference
Coal mine (cut-through #4)	Australia	Coal	2004-06-11	Extensometer	Digitized	(*31*)
Coal mine (cut-through #5)	Australia	Coal	2004-06-04	Extensometer	Digitized	(*31*)
Gold mine (event 1)	South Africa	Metamorphic rock	1997-02-05	Seismic stations	Digitized	(*42*)
Gold mine (event 2)	South Africa	Metamorphic rock	1997-04-03	Seismic stations	Digitized	(*42*)
Gold mine (event 3)	South Africa	Metamorphic rock	1997-04-06	Seismic stations	Digitized	(*42*)
Gold mine (event 4)	South Africa	Metamorphic rock	1997-05-04	Seismic stations	Digitized	(*42*)
Gold mine (event 5)	South Africa	Metamorphic rock	1997-05-26	Seismic stations	Digitized	(*42*)
Gold mine (event 6)	South Africa	Metamorphic rock	1997-06-06	Seismic stations	Digitized	(*42*)
Gold mine (event 7)	South Africa	Metamorphic rock	1997-06-23	Seismic stations	Digitized	(*42*)
Gold mine (event 8)	South Africa	Metamorphic rock	1997-08-15	Seismic stations	Digitized	(*42*)
Platinum mine	South Africa	Merensky reef	2007-04-04	Closure meters	Digitized	(*41*)

Table S3. Glacier cases (17 events in total).

Site	Location	Type	Failure time	Size	Monitoring method	Data source	Reference
Amery	Antarctica	Ice shelf	2019-09-25	1,636 km^2	Satellite images	Digitized	(*43*)
Eiger glacier (2001 event)	Switzerland	Polythermal glacier	2001-08-20	2.7×10^5 m^3	Theodolite with reflectors	Digitized	(*84*)
Eiger glacier (2016 event)	Switzerland	Polythermal glacier	2016-08-25	1.5×10^4 m^3	Ground-based InSAR	Digitized	(*85*)
Grandes Jorasses (2014 event)	Italy	Cold glacier	2014-09-23 & 2014-09-29	1.5×10^5 m^3	Total station with reflectors	Original	(*32*)
Grandes Jorasses (2020 event)	Italy	Cold glacier	2020-11-11	2.0×10^4 m^3	Total station with reflectors	Digitized	(*86*)
Gruben	Switzerland	Temperate glacier	1974-09-09	Unknown	Dial gauge with wire	Digitized	(*84*)
Mönch	Switzerland	Temperate glacier	2003-07-04	6×10^5 m^3	Theodolite with reflectors	Original	(*84*)
Planpincieux (event 1)	Italy	Polythermal glacier	2015-08-16	1.4×10^4 m^3	Time-lapse camera	Original	(*46, 86*)
Planpincieux (event 2)	Italy	Polythermal glacier	2016-08-15	2.5×10^4 m^3	Time-lapse camera	Original	(*46, 86*)
Planpincieux (event 3)	Italy	Polythermal glacier	2017-08-03	2.0×10^4 m^3	Time-lapse camera	Original	(*46, 86*)
Planpincieux (event 4)	Italy	Polythermal glacier	2017-08-31	5.4×10^4 m^3	Time-lapse camera	Original	(*46, 86*)
Planpincieux (event 5)	Italy	Polythermal glacier	2017-10-12	1.5×10^4 m^3	Time-lapse camera	Original	(*46, 86*)
Planpincieux (event 6)	Italy	Polythermal glacier	2019-07-26	2.2×10^4 m^3	Time-lapse camera	Original	(*46, 86*)
UK211	Antarctica	Iceberg	2006-11-23	2,400 km^2	Satellite images	Digitized	(*44*)
Weisshorn (1973 event)	Switzerland	Cold glacier	1972-10-17	5×10^5 m^3	Theodolite with reflectors	Original	(*87*)
Weisshorn (2005 event)	Switzerland	Cold glacier	2005-03-30	5×10^5 m^3	Total station with reflectors	Original	(*87, 88*)
Weissmies	Switzerland	Polythermal glacier	2017-09-10	2.5×10^5 m^3	Time-lapse camera	Original	(*15, 45*)

Table S4. Volcano cases (32 events in total).

Site	Location	Type	Eruption time	Erupted volume (m^3)	Monitoring method	Data source	Reference
Adatara	Japan	Stratovolcano	1996-09-01	1.1×10^6	JMA seismic network	Original	(*56*)
Asama	Japan	Complex volcano	2009-02-02	$\sim 10^4$	JMA seismic network	Original	(*56*)
Augustine	USA	Lava dome	2006-01-11	7.3×10^7	USGS seismic network-AVO	Original	(*56*)
Axial Seamount	USA	Submarine fissure volcano	2011-04-06	9.9×10^7	Bottom pressure recorders & mobile pressure recorders	Original	(*89*)
Bezymianny	Russia	Stratovolcano	1960-04-10	$\sim 10^6$	Unspecified	Digitized	(*6*)
Etna (1989 event)	Italy	Stratovolcano	1989-09-08	$\sim 10^7$	ISCSN	Original	(*56*)
Etna (2013 event)	Italy	Stratovolcano	2013-09-05	$\sim 10^6$	Geochemical monitoring stations	Original	(*50, 56*)
Hierro	Spain	Submarine shield volcano	2011-10-10	3.3×10^7	El Hierro seismic network	Original	(*56, 90*)
Kilauea (1971 event)	USA	Shield volcano	1971-08-14	9.1×10^6	NCDC-ANSS seismic network	Original	(*56*)
Kilauea (1972 event)	USA	Shield volcano	1972-02-04	1.2×10^8	NCDC-ANSS seismic network	Original	(*56*)
Kilauea (1983 event)	USA	Shield volcano	1983-01-03	4×10^6	NCDC-ANSS seismic network	Original	(*56*)
Kujusan	Japan	Stratovolcano	1995-10-11	2×10^5	JMA seismic network	Original	(*56, 91*)
Mauna Loa	USA	Shield volcano	1984-03-25	$\sim 10^8$	Unspecified	Digitized	(*92*)
Merapi (2006 event)	Indonesia	Stratovolcano	2006-06-06	5.3×10^6	Plawangan Observatory	Original	(*56, 93*)
Merapi (2010 event)	Indonesia	Stratovolcano	2010-10-26	$\sim 10^7$	Plawangan Observatory	Original	(*47, 56*)
Pinatubo	Philippines	Stratovolcano	1991-06-07	5×10^9	Seismic network	Original	(*56*)
Redoubt (1989 event)	USA	Stratovolcano	1989-12-14	$\sim 10^8$	ANSS seismic network	Original	(*56, 94*)
Redoubt (2009 event)	USA	Stratovolcano	2009-03-22	$\sim 10^8$	ANSS seismic network	Original	(*56, 95*)
Ruapehu (1995 event)	New Zealand	Stratovolcano	1995-09-18	2×10^5	New Zealand seismic network	Original	(*56*)
Ruapehu (1996 event)	New Zealand	Stratovolcano	1996-06-19	$\sim 10^7$	New Zealand seismic network	Original	(*56*)
Ruapehu (2006 event)	New Zealand	Stratovolcano	2006-10-04	$\sim 10^5$	New Zealand seismic network	Original	(*56*)

Table S4 (continued). Volcano cases (32 events in total).

Site	Location	Type	Eruption time	Erupted volume (m^3)	Monitoring method	Data source	Reference
Sakurajima	Japan	Stratovolcano	2017-03-25	$\sim10^6$	JMA seismic network	Original	(*56*)
Sierra Negra (2005 event)	Ecuador	Shield volcano	2005-10-22	1.5×10^8	Continuous GPS network	Original	(*96*)
Sierra Negra (2018 event)	Ecuador	Shield volcano	2018-06-26	1.4×10^8	Continuous GPS network	Original	(*48*)
St. Helens (1980 event)	USA	Stratovolcano	1980-03-27	$\sim10^5$	PNSN	Original	(*56, 97*)
St. Helens (1981 event)	USA	Stratovolcano	1981-09-06	$\sim10^6$	PNSN	Original	(*56, 97*)
St. Helens (1982 event)	USA	Stratovolcano	1982-03-19	$\sim10^6$	PNSN, tiltmeter	Original	(*56, 97*)
St. Helens (1985 event)	USA	Stratovolcano	1985-05-25	$\sim10^6$	PNSN	Original	(*56, 98*)
Soufriere Hills	UK	Stratovolcano	1995-11-15	7×10^7	ISCSN	Original	(*56, 99*)
Tokachidake	Japan	Stratovolcano	2004-02-25	$\sim10^5$	JMA seismic network	Original	(*56*)
Unzen	Japan	Complex volcano	1990-11-17	2.1×10^8	ISCSN	Original	(*56, 100*)
Yakedake	Japan	Stratovolcano	1995-02-11	6×10^3	JMA seismic network	Original	(*56*)

Note: PNSN - Pacific Northwest Seismic Network; ISCSN - International Seismological Centre Seismographic Network; JMASN - Japan Meteorological Agency Seismic Network; NCDC - National Climatic Data Center; ANSS - Advanced National Seismic System; GPS - Global Positioning System; USGS - United States Geological Survey; AVO - Alaska Volcano Observatory.

Table S5. Parameters of the LPPLS and PLS models fitted to landslide data (49 events and 94 time series monitoring data in total).

Data	LPPLS							PLS			
	t_c	m	ω	ϕ	A	B	C	t_c	m	A	B
Abbotsford	1.40	-0.24	4.94	1.56	-2.60e+00	5.90e+00	8.03e-02	1.19	-0.20	-3.12e+00	6.24e+00
Achoma	-0.06	0.076	5.01	-1.21	2.59e+01	-1.79e+01	1.84e-01	2.49	-0.13	-1.16e+01	2.27e+01
Agoyama	0.00	-0.35	5.27	0.29	-1.87e+00	7.23e+00	7.87e-02	0.00	-0.36	-1.84e+00	7.20e+00
Arvigo	0.17	-0.063	5.04	-1.28	-5.37e-01	7.29e-01	2.74e-03	0.17	-0.07	-4.40e-01	6.34e-01
Baishi	0.02	0.19	5.73	0.93	5.68e+01	-1.67e+01	1.23e-01	0.02	0.22	5.36e+01	-1.36e+01
Baiyan	26.78	0.33	4.94	0.49	1.96e-01	-3.10e-02	2.86e-03	31.17	-0.29	-1.25e-01	6.70e-01
Brienz/Brinzauls (reflector 715)	3.11	-0.53	4.94	-0.03	-1.40e+00	4.76e+01	5.79e-01	1.57	-0.39	-3.41e+00	3.64e+01
Brienz/Brinzauls (reflector 719)	3.40	-0.63	4.94	-0.20	-1.11e+00	8.53e+01	1.23e+00	3.40	-0.64	-1.09e+00	8.62e+01
Brienz/Brinzauls (reflector 725)	3.22	-0.61	4.94	-0.10	-8.45e-01	6.89e+01	9.67e-01	1.62	-0.45	-2.79e+00	4.91e+01
Cadia	16.16	-0.8	4.94	-0.43	2.78e-03	1.09e+00	6.15e-02	19.48	-0.87	4.31e-03	1.44e+00
Copper open pit	10.28	-1.2	9.88	-0.16	1.82e-03	1.15e+00	1.88e-01	10.28	-1.28	2.30e-03	1.55e+00
Dosan (point 1)	0.06	-0.15	9.41	0.24	-7.73e-02	8.90e-02	8.68e-04	0.10	-0.27	-4.28e-02	5.50e-02
Dosan (point 2)	0.16	-0.52	4.94	-0.43	-5.63e-02	8.71e-02	2.06e-03	0.18	-0.57	-4.86e-02	8.07e-02
Dosan (point 3)	0.05	-0.38	4.94	0.94	-1.63e-01	2.55e-01	2.12e-03	0.05	-0.38	-1.59e-01	2.51e-01
Gallivaggio	0.85	-1.2	11.63	-1.46	3.54e-03	5.78e-03	4.16e-04	0.85	-1.20	3.56e-03	5.89e-03
Galterengraben (TJM1)	32.07	-0.49	5.99	-1.51	-4.97e+00	8.83e+01	3.47e+00	36.07	-0.42	-6.65e+00	7.95e+01
Galterengraben (TJM2)	30.83	-0.53	4.94	-0.19	-4.31e+00	1.29e+02	5.47e+00	34.67	-0.53	-4.49e+00	1.35e+02
Galterengraben (TJM6)	12.96	-0.51	4.94	-1.56	-1.22e-01	3.12e+01	1.38e+00	6.52	-0.31	-1.66e+00	1.85e+01
Grabengufer (GNSS)	0.24	-0.35	12.42	1.16	7.71e+00	4.28e-01	2.75e-02	-0.01	0.13	8.95e+00	-8.36e-01
Grabengufer (inclinometer W)	0.23	-1.2	4.94	-1.39	2.60e+00	1.44e+00	3.06e-01	0.03	-0.46	1.02e+00	2.77e+00
Grabengufer (inclinometer N)	0.03	0.1	6.70	-0.84	7.55e+01	-7.59e+01	5.56e-01	0.03	0.13	5.83e+01	-5.88e+01
Hogarth (extensometer 1)	3.11	-2.7	4.94	1.05	3.09e-03	8.73e+00	2.23e+00	0.00	-1.20	2.06e-03	1.07e-01
Hogarth (extensometer 2)	0.00	-1.3	9.86	-1.22	7.35e-03	1.48e-01	9.85e-03	0.00	-1.37	7.50e-03	1.81e-01
Hogarth (extensometer 3)	6.76	-1.8	14.45	-1.43	5.01e-03	7.06e-01	3.98e-02	0.00	-1.19	4.81e-03	8.05e-02
Hogarth (extensometer 4)	0.00	-0.87	5.39	-0.81	8.56e-03	4.85e-02	1.16e-03	0.00	-0.89	8.61e-03	5.12e-02
Hogarth (extensometer 6)	7.11	-1.6	6.98	-0.01	1.14e-02	4.47e-01	9.90e-03	5.33	-1.53	1.14e-02	2.83e-01

Table S5 (continued). Parameters of the LPPLS and PLS models fitted to landslide data (49 events and 94 time series monitoring data in total).

Data	LPPLS							PLS			
	t_c	m	ω	ϕ	A	B	C	t_c	m	A	B
Iron mine	0.43	-0.13	11.46	0.21	-9.44e-01	1.64e+00	5.84e-03	0.43	-0.15	-8.46e-01	1.55e+00
Jinlonggou	4.78	-0.87	4.94	-1.36	-5.56e-03	2.19e-01	2.52e-02	-1.00	-0.22	-2.89e-02	7.09e-02
Kagemori (point 1)	3.11	0.14	4.94	1.52	5.04e-01	-1.59e-01	7.03e-04	3.50	0.09	6.36e-01	-2.83e-01
Kagemori (point 3)	12.44	0.22	4.94	1.21	6.91e-01	-2.00e-01	3.32e-03	14.00	0.12	1.12e+00	-5.58e-01
Kagemori (point 13)	2.84	0.57	4.94	0.45	2.82e-01	-1.29e-02	2.17e-04	3.20	0.71	2.72e-01	-7.01e-03
Kagemori (point 15)	4.53	-0.45	4.94	0.63	1.48e-01	8.12e-01	2.42e-02	0.00	-0.10	-3.87e-01	9.67e-01
Kagemori (point 17)	3.73	0.012	6.19	1.31	5.86e+00	-5.44e+00	5.51e-04	4.20	-0.01	-8.55e+00	8.98e+00
Kagemori (point 18)	0.00	0.21	4.94	-0.95	6.95e-01	-2.05e-01	1.70e-03	0.00	0.24	6.49e-01	-1.63e-01
Kagemori (point 21)	4.44	-0.95	7.20	0.72	1.03e-02	1.07e+00	7.21e-02	5.00	-0.93	7.49e-03	1.11e+00
Kagemori (point 23)	2.89	-0.4	6.67	-0.21	-7.85e-02	8.65e-01	1.77e-02	4.33	-0.48	-5.52e-02	1.04e+00
La Saxe	5.64	-3.6	7.72	-0.46	3.47e+00	6.57e+03	3.09e+03	6.34	-2.43	3.39e+00	5.83e+02
Letlhakane diamond mine	9.53	-0.37	4.94	1.20	-4.44e-01	2.29e+00	1.32e-01	10.61	-0.50	-2.81e-01	2.61e+00
Longjing	2.22	-0.45	4.94	-1.24	-1.66e-01	1.08e+00	2.84e-02	0.95	-0.04	-4.19e+00	4.77e+00
Maoxian (point 1)	2.86	0.17	5.31	0.53	1.12e-01	-3.42e-02	8.37e-04	2.86	0.18	1.09e-01	-3.14e-02
Maoxian (point 2)	2.86	0.15	5.32	0.43	1.69e-01	-5.89e-02	6.38e-04	2.86	0.15	1.65e-01	-5.47e-02
Maoxian (point 3)	2.86	0.14	5.29	0.69	1.75e-01	-6.48e-02	8.57e-04	2.86	0.14	1.73e-01	-6.19e-02
Mt. Beni	-0.86	-0.33	5.21	0.15	-1.02e+00	6.91e+00	1.23e-01	1.73	-0.45	-6.44e-01	8.76e+00
Mud Greek	42.13	-0.46	4.94	0.32	-2.88e-01	5.01e+00	5.57e-01	47.38	-0.52	-1.98e-01	5.74e+00
Nevis Bluff (point 1)	-3.11	-0.11	4.94	1.11	-5.28e-01	9.42e-01	5.57e-03	-2.00	-0.21	-2.20e-01	7.06e-01
Nevis Bluff (point 2)	-4.80	-0.051	4.94	-0.95	-2.07e+00	2.71e+00	5.33e-03	-3.90	-0.13	-6.87e-01	1.41e+00
Nevis Bluff (point A)	-3.38	-0.077	4.94	1.42	-1.14e+00	1.75e+00	6.00e-03	-2.30	-0.16	-4.58e-01	1.16e+00
New Tredegar	1.63	-0.58	5.93	0.96	6.11e-02	1.35e+00	3.52e-02	1.21	-0.52	4.21e-02	1.21e+00
Northern Bohemia	3.94	-0.68	4.94	0.12	7.62e-03	6.59e-02	9.97e-03	4.35	-0.64	7.64e-03	5.98e-02
Open pit mine (event 3)	0.03	-1.4	10.94	-0.14	1.50e-02	2.64e-03	1.08e-04	0.04	-1.49	1.51e-02	2.49e-03

Table S5 (continued). Parameters of the LPPLS and PLS models fitted to landslide data (49 events and 94 time series monitoring data in total).

Data	LPPLS							PLS			
	t_c	m	ω	ϕ	A	B	C	t_c	m	A	B
Open pit mine (event 4)	0.13	0.041	4.94	0.81	1.92e+00	-1.83e+00	1.27e-02	0.00	0.38	2.85e-01	-2.14e-01
Open pit mine (event 5)	0.25	-0.1	5.97	-0.94	-1.33e-01	1.67e-01	2.54e-03	0.25	0.13	1.63e-01	-1.29e-01
Otomura	0.53	-0.81	4.94	-1.07	4.17e-02	3.12e-01	1.67e-02	0.00	-0.65	3.48e-02	2.37e-01
Preonzo (extensometer 1)	5.95	-1.1	6.47	1.15	5.44e-01	1.84e+00	1.11e-01	6.59	-1.14	5.42e-01	2.01e+00
Preonzo (extensometer 2)	3.62	-0.65	4.94	-0.15	5.54e-01	6.72e-01	3.24e-02	4.99	-0.85	5.74e-01	1.04e+00
Preonzo (extensometer 3)	5.51	-1.4	5.16	-1.44	6.19e-01	7.31e+00	4.50e-01	6.09	-1.35	6.15e-01	7.86e+00
Preonzo (extensometer 4)	5.42	-1.5	6.63	1.27	7.32e-01	1.21e+01	7.97e-01	4.85	-1.30	7.20e-01	7.89e+00
Preonzo (extensometer 5)	4.44	-1.3	5.97	0.20	5.39e-01	6.21e+00	5.58e-01	3.02	-1.01	5.19e-01	2.66e+00
Preonzo (reflector 2)	2.49	-0.93	4.94	0.77	3.45e-01	4.80e+00	4.18e-01	0.89	-0.50	1.21e-01	2.32e+00
Preonzo (reflector 4)	2.40	-0.87	4.94	0.89	3.69e-01	4.43e+00	3.30e-01	0.89	-0.47	1.18e-01	2.36e+00
Preonzo (reflector 5)	2.35	-0.79	4.94	0.93	2.56e-01	2.83e+00	1.97e-01	0.89	-0.43	5.77e-02	1.65e+00
Preonzo (reflector 8)	2.35	-0.76	4.94	0.94	1.67e-01	1.74e+00	1.14e-01	0.89	-0.41	2.97e-02	1.06e+00
Preonzo (reflector 9)	3.82	-1.1	5.61	1.47	2.24e-01	2.81e+00	2.12e-01	2.35	-0.79	1.98e-01	1.33e+00
Puigcercós (area 4)	191.03	0.63	4.94	-1.48	2.42e-01	-2.01e-03	8.77e-05	2.87	0.69	1.96e-01	-1.06e-03
Puigcercós (area 6)	151.36	-0.67	4.94	-0.52	-9.30e-02	1.35e+01	7.96e-01	73.42	-0.36	-1.92e-01	2.76e+00
Puigcercós (area 7)	189.80	-0.5	4.94	1.18	-1.16e-01	5.03e+00	4.20e-01	1.35	0.14	5.20e-01	-1.85e-01
Puigcercós (area 9)	130.55	-1.7	9.16	-1.44	-7.31e-03	9.23e+02	2.53e+02	33.62	-0.83	-1.81e-02	5.80e+00
Road slope (event 1)	0.13	-0.41	4.94	0.03	-6.02e-02	9.56e-02	2.58e-03	0.07	-0.25	-1.12e-01	1.45e-01
Road slope (event 2)	0.86	0.031	6.89	1.45	1.18e+01	-1.10e+01	2.80e-02	0.96	-0.05	-7.71e+00	8.54e+00
Road slope (event 3)	-0.05	0.0043	4.94	1.29	2.10e+00	-2.12e+00	6.94e-04	-0.05	-0.12	-6.23e-02	5.25e-02
Road slope (event 4)	0.01	-0.51	4.94	1.34	-1.75e-02	4.66e-03	4.90e-04	0.01	-0.51	-1.68e-02	4.72e-03
Road slope (event 5)	-0.03	-0.4	4.94	-0.92	-1.46e-02	9.38e-03	5.20e-04	-0.03	-0.54	-8.09e-03	4.92e-03

Table S5 (continued). Parameters of the LPPLS and PLS models fitted to landslide data (49 events and 94 time series monitoring data in total).

Data	LPPLS							PLS			
	t_c	m	ω	ϕ	A	B	C	t_c	m	A	B
Road slope (event 6)	0.14	-0.46	4.94	-0.40	-2.37e-02	2.58e-02	1.28e-03	0.16	-0.58	-1.70e-02	1.94e-02
Road slope (event 7)	-0.03	-0.64	4.94	-0.11	1.12e-02	2.18e-02	2.06e-03	-0.10	-0.13	-1.13e-01	1.42e-01
Road slope (event 8)	0.02	0.19	4.94	0.42	2.27e-01	-2.83e-01	2.47e-03	0.02	0.09	4.13e-01	-4.56e-01
Road slope (event 9)	0.82	-0.92	6.87	0.53	-1.12e-01	9.80e-01	5.31e-02	0.93	-0.96	-1.11e-01	1.06e+00
Road slope (event 10)	0.07	-0.75	4.94	0.64	-3.52e-02	2.58e-02	1.79e-03	0.07	-0.82	-2.87e-02	2.15e-02
Roesgrenda	-0.15	0.2	6.28	-1.23	1.05e-01	-3.84e-02	6.89e-04	-0.15	0.25	9.35e-02	-2.76e-02
Takabayama	-0.06	-0.28	4.94	-0.01	-9.23e-01	2.19e+00	2.84e-02	-0.06	-0.27	-9.75e-01	2.23e+00
Vajont (bench mark 2)	6.13	-0.98	5.59	0.33	2.98e+00	1.24e+01	1.30e+00	6.90	-0.89	2.90e+00	1.13e+01
Vajont (bench mark 4)	5.42	0.21	6.89	0.48	3.99e+00	-7.26e-01	5.85e-03	6.10	0.16	4.42e+00	-1.09e+00
Vajont (bench mark 6)	6.40	0.02	4.94	-0.59	2.76e+01	-2.28e+01	4.17e-02	7.20	-0.15	-1.05e-01	5.36e+00
Vajont (bench mark 58)	8.71	-0.025	4.94	0.52	-1.27e+01	1.68e+01	2.39e-02	9.80	-0.13	-3.72e-01	4.88e+00
Veslemannen (radar point 1)	0.13	0.65	6.52	-0.75	1.90e+01	-3.39e-01	3.06e-02	10.93	0.29	2.55e+01	-3.28e+00
Veslemannen (radar point 2)	0.13	0.42	7.49	-0.82	1.36e+01	-1.03e+00	4.09e-02	9.23	0.07	4.39e+01	-2.68e+01
Veslemannen (radar point 3)	0.13	0.37	6.46	-0.42	1.19e+01	-1.00e+00	4.16e-02	10.93	-0.04	-4.08e+01	5.68e+01
Veslemannen (radar point 4)	0.13	0.39	6.42	-0.27	6.61e+00	-5.03e-01	2.36e-02	9.64	0.03	4.06e+01	-3.22e+01
Veslemannen (radar point 5)	0.13	0.49	6.44	-0.31	5.70e+00	-2.13e-01	1.25e-02	10.53	0.15	9.63e+00	-2.87e+00
Veslemannen (radar point 6)	0.13	0.21	6.51	-0.48	4.54e+00	-1.15e+00	2.45e-02	1.26	0.11	7.00e+00	-3.35e+00
Veslemannen (radar point 7)	0.13	0.47	6.57	-0.81	4.23e+00	-2.03e-01	1.12e-02	10.23	0.14	7.85e+00	-2.74e+00
Welland (point 1)	0.28	-0.5	4.94	-1.41	-1.22e-03	1.37e-02	8.72e-04	0.31	-0.54	-3.01e-04	1.30e-02
Welland (point 2)	0.23	-0.47	4.96	-0.82	-1.02e-03	1.21e-02	9.11e-04	0.12	-0.31	-4.56e-03	1.50e-02
Xinmo	2.62	0.049	4.94	-1.35	2.68e-01	-1.85e-01	1.46e-03	2.62	0.06	2.25e-01	-1.42e-01
Xintan	12.89	-0.96	4.94	0.24	8.78e+00	7.04e+01	8.00e+00	15.36	-0.97	8.71e+00	8.45e+01

Note: t_c is in day; m, ω, and ϕ are dimensionless; A is in deg for tilt (Grabengufer inclinometer) and in meter for displacement (all other cases); B and C are in the unit of A per day^m. The actual failure corresponds to time $t = 0$ day. Parameters A, B, and C are displayed using scientific exponential notation, where 1.00e-02 represents 1.00×10^{-2}.

Table S6. Parameters of the LPPLS and PLS models fitted to rockburst data (11 events and 11 time series monitoring data in total).

Data	LPPLS							PLS			
	t_c	m	ω	ϕ	A	B	C	t_c	m	A	B
Coal mine (cut-through #4)	0.12	-0.58	4.94	0.87	-7.14e+01	7.81e+01	3.86e+00	0.13	-0.62	-6.29e+01	7.15e+01
Coal mine (cut-through #5)	0.02	-0.12	4.94	-0.01	-2.43e-01	2.85e-01	5.77e-03	0.05	-0.28	-7.64e-02	1.19e-01
Gold mine (event 1)	-0.14	0.5	7.26	1.56	1.34e+03	-6.42e+02	4.43e+01	-0.14	0.43	1.40e+03	-7.14e+02
Gold mine (event 2)	0.08	-0.32	11.94	1.21	-4.91e+02	6.06e+02	3.61e+01	0.07	-0.09	-2.68e+03	2.80e+03
Gold mine (event 3)	1.01	0.24	9.59	-0.79	2.33e+04	-1.26e+04	2.11e+02	0.28	0.40	1.39e+04	-5.10e+03
Gold mine (event 4)	-2.46	0.59	9.14	0.36	1.36e+04	-1.34e+03	1.85e+01	-1.98	0.58	1.40e+04	-1.45e+03
Gold mine (event 5)	0.42	0.11	7.75	-1.40	2.31e+04	-1.70e+04	2.10e+02	0.97	0.01	2.12e+05	-2.05e+05
Gold mine (event 6)	0.03	0.42	8.37	1.04	3.28e+03	-1.51e+03	7.88e+01	0.03	0.44	3.22e+03	-1.45e+03
Gold mine (event 7)	3.75	0.43	4.98	-0.18	5.47e+03	-9.12e+02	3.47e+01	7.26	0.13	1.52e+04	-8.75e+03
Gold mine (event 8)	-5.42	0.64	5.65	0.26	4.14e+03	-2.12e+02	3.33e+01	4.74	0.09	2.06e+04	-1.33e+04
Platinum mine	0.04	0.31	4.94	1.38	2.35e-01	-3.56e-02	6.93e-04	0.04	0.36	2.31e-01	-3.07e-02

Note: t_c is in day; m, ω, and ϕ are dimensionless; A is in meter for displacement (Coal and Platinum mines) and in $kN^{1/2}km^{1/2}$ for Benioff strain (Gold mine); B and C are in the unit of A per day^m. The actual failure corresponds to time $t = 0$ day. Parameters A, B, and C are displayed using scientific exponential notation, where 1.00e-02 represents 1.00×10^{-2}.

Table S7. Parameters of the LPPLS and PLS models fitted to glacier data (17 events and 21 time series monitoring data in total).

Data	LPPLS							PLS			
	t_c	m	ω	ϕ	A	B	C	t_c	m	A	B
Amery	2.69	0.14	11.47	1.35	6.64e+01	-1.39e+01	1.26e-01	2.69	0.14	6.47e+01	-1.25e+01
Eiger glacier (2001 event)	-0.46	0.027	14.15	-0.06	5.10e+01	-4.83e+01	3.96e-03	-0.40	0.00	3.12e+02	-3.09e+02
Eiger glacier (2016 event)	0.00	0.51	4.94	-0.44	3.61e+00	-4.41e-01	3.43e-03	0.00	0.53	3.56e+00	-4.03e-01
Grandes Jorasses (2014 event, prism 13)	0.00	0.33	4.94	0.65	4.88e+01	-2.88e+00	3.56e-02	0.00	0.34	4.85e+01	-2.66e+00
Grandes Jorasses (2014 event, prism 14)	1.79	0.36	4.94	1.07	4.70e+01	-2.57e+00	6.86e-03	1.79	0.36	4.69e+01	-2.50e+00
Grandes Jorasses (2020 event)	0.26	0.36	5.80	0.62	2.34e+00	-9.28e-01	4.06e-03	0.26	0.35	2.36e+00	-9.52e-01
Gruben	0.03	0.5	8.11	0.16	2.14e+00	-1.20e+00	9.30e-03	0.03	0.50	2.14e+00	-1.20e+00
Mönch	-14.13	0.45	4.94	-1.10	7.27e+00	-1.04e+00	1.39e-02	-13.40	0.37	8.33e+00	-1.63e+00
Planpincieux (event 1)	0.00	0.58	4.94	0.41	1.85e+01	-1.38e+00	7.70e-03	0.00	0.60	1.83e+01	-1.31e+00
Planpincieux (event 2)	5.07	0.36	4.94	0.22	3.56e+01	-7.83e+00	8.69e-02	5.70	0.27	4.41e+01	-1.40e+01
Planpincieux (event 3)	0.00	0.53	4.94	1.19	2.26e+01	-2.42e+00	2.66e-02	1.73	0.43	2.67e+01	-4.34e+00
Planpincieux (event 4)	1.78	0.69	4.94	1.21	1.71e+01	-1.89e+00	6.52e-02	2.00	0.56	1.92e+01	-3.07e+00
Planpincieux (event 5)	0.00	0.7	7.41	1.28	1.13e+01	-1.00e+00	1.65e-02	0.00	0.72	1.11e+01	-9.04e-01
Planpincieux (event 6)	4.09	0.62	4.94	-0.50	1.36e+01	-1.15e+00	1.71e-02	4.60	0.62	1.39e+01	-1.16e+00
UK211	40.47	-0.36	4.94	-0.68	-1.12e+02	9.71e+02	4.90e+01	2.39	0.10	4.22e+02	-2.35e+02
Weisshorn (1973 event)	-9.84	0.21	4.94	-1.07	8.06e+01	-2.53e+01	2.40e-01	-7.03	0.11	1.42e+02	-7.66e+01
Weisshorn (2005 event, #103)	-0.92	0.56	4.94	-0.44	9.32e+00	-1.48e+00	7.17e-03	-1.18	0.57	9.11e+00	-1.44e+00
Weisshorn (2005 event, #104)	-0.92	0.53	4.94	-0.59	9.98e+00	-1.79e+00	6.59e-03	-0.92	0.52	1.01e+01	-1.86e+00
Weisshorn (2005 event, #105)	-0.92	0.44	4.94	-0.82	1.19e+01	-2.86e+00	1.11e-02	-0.66	0.41	1.27e+01	-3.37e+00
Weisshorn (2005 event, #106)	-2.99	0.36	9.24	1.19	1.28e+01	-4.11e+00	6.46e-03	-2.99	0.37	1.25e+01	-3.87e+00
Weissmies	0.75	0.39	11.20	1.09	8.52e+01	-8.41e+00	5.63e-02	0.75	0.40	8.48e+01	-8.12e+00

Note: t_c is in day; m, ω, and ϕ are dimensionless; A is in km^2 for area loss (UK211), in km for rift length (Amery), and in meter for displacement (all other cases); B and C are in the unit of A per day^m. The actual failure corresponds to time $t = 0$ day. Parameters A, B, and C are displayed using scientific exponential notation, where 1.00e-02 represents 1.00×10^{-2}.

Table S8. Parameters of the LPPLS and PLS models fitted to volcano data (32 events and 34 time series monitoring data in total).

Data	LPPLS							PLS			
	t_c	m	ω	ϕ	A	B	C	t_c	m	A	B
Adatara	93.18	0.36	7.12	0.90	2.20e+02	-1.22e+01	2.76e-01	105.70	0.29	2.49e+02	-2.33e+01
Asama	0.00	0.8	10.41	0.70	1.31e+04	-1.59e+02	6.40e+00	0.00	0.78	1.31e+04	-1.73e+02
Augustine	15.68	-0.31	4.96	-0.65	-4.19e+02	6.43e+03	1.69e+02	15.68	-0.28	-5.73e+02	6.12e+03
Axial Seamount	6.00	0.64	9.23	0.61	3.38e+00	-7.50e-03	5.12e-04	323.10	0.32	4.38e+00	-1.62e-01
Bezymianny	1.78	-1	4.94	0.41	-8.13e+00	2.93e+02	1.28e+01	2.11	-1.02	-8.36e+00	3.15e+02
Etna (1989 event)	31.62	-0.15	10.84	-0.91	-4.28e+02	1.10e+03	6.93e+00	35.20	-0.21	-3.02e+02	1.09e+03
Etna (2013 event)	0.35	0.76	4.94	-0.54	2.02e+03	-3.74e+01	8.23e-01	14.35	0.59	2.49e+03	-1.03e+02
Hierro	2.49	0.72	4.94	-0.41	1.20e+04	-4.56e+02	5.12e+01	11.20	0.38	2.03e+04	-3.40e+03
Kilauea (1971 event)	3.02	-0.12	4.94	0.33	-2.56e+03	4.33e+03	7.93e+01	0.00	0.30	1.64e+03	-4.80e+02
Kilauea (1972 event)	12.71	0.81	4.94	-0.48	8.03e+03	-5.86e+01	6.29e+00	43.20	0.55	1.06e+04	-3.46e+02
Kilauea (1983 event)	2.00	0.99	9.05	-0.29	6.58e+03	-1.56e+01	1.34e+00	34.20	0.82	7.46e+03	-4.50e+01
Kujusan	4.98	0.75	4.94	0.19	4.80e+01	-5.10e-01	7.93e-02	6.10	0.99	4.70e+01	-1.64e-01
Mauna Loa	5.73	-0.15	5.05	0.02	1.41e+01	7.75e+00	6.31e-02	4.30	-0.05	4.60e+00	1.65e+01
Merapi (2006 event)	5.51	0.39	4.94	-0.57	2.98e+04	-5.57e+03	8.98e+01	6.20	0.28	3.76e+04	-1.09e+04
Merapi (2010 event)	3.02	-0.35	5.44	-1.00	-3.90e+02	2.08e+03	2.74e+01	3.40	-0.41	-2.91e+02	2.14e+03
Pinatubo	0.36	-0.016	6.94	0.39	-2.90e+04	3.06e+04	6.06e+01	3.20	-0.50	-7.04e+02	4.50e+03
Redoubt (1989 event)	8.91	0.52	4.94	-0.16	7.26e+01	-3.40e+00	2.93e-01	3.00	0.79	6.10e+01	-6.93e-01
Redoubt (2009 event)	3.43	0.7	8.43	0.10	1.39e+03	-6.89e+01	3.93e+00	-1.00	0.72	1.24e+03	-5.90e+01
Ruapehu (1995 event)	13.60	0.67	6.40	0.32	3.87e+02	-7.26e+00	6.23e-01	0.00	0.99	3.36e+02	-1.26e+00
Ruapehu (1996 event)	9.07	0.83	4.94	0.75	1.84e+03	-1.79e+01	2.11e+00	10.20	0.99	1.83e+03	-9.04e+00
Ruapehu (2006 event)	25.07	0.45	11.66	1.50	9.22e+01	-6.70e+00	1.01e-01	28.20	0.40	1.02e+02	-1.02e+01
Sakurajima	8.18	-0.055	4.94	-0.88	-7.37e+03	9.66e+03	5.01e+01	9.20	-0.13	-2.67e+03	5.22e+03
Sierra Negra (2005 event)	85.89	-0.31	7.21	-0.92	-2.06e+00	1.63e+01	2.43e-01	96.00	-0.37	-1.69e+00	1.99e+01
Sierra Negra (2018 event)	154.60	-0.1	7.36	0.55	-8.32e+00	2.02e+01	4.79e-02	172.80	-0.15	-4.83e+00	1.92e+01
St. Helens (1980 event)	3.41	-3.4	7.42	-0.63	1.06e+01	1.64e+04	5.55e+03	0.13	-2.04	1.05e+01	2.51e+02

Table S8 (continued). Parameters of the LPPLS and PLS models fitted to volcano data (32 events and 34 time series monitoring data in total).

Data	LPPLS							PLS			
	t_c	m	ω	ϕ	A	B	C	t_c	m	A	B
St. Helens (1981 event)	0.20	0.73	4.94	0.14	9.98e+02	-1.42e+01	9.96e-01	0.20	0.86	9.76e+02	-7.42e+00
St. Helens (1982 event, seismic data)	4.62	-0.099	4.94	0.83	-1.97e+03	3.25e+03	4.32e+01	5.20	-0.31	-3.28e+02	1.92e+03
St. Helens (1982 event, radial tilt)	0.00	0.32	6.39	0.09	2.49e+03	-5.44e+02	9.76e+00	0.64	0.26	2.85e+03	-8.00e+02
St. Helens (1982 event, tangential tilt)	5.24	-0.4	6.14	0.25	-4.10e+03	6.24e+03	7.49e+01	5.90	-0.44	-4.00e+03	6.76e+03
St. Helens (1985 event)	3.29	-1.5	5.62	1.06	3.65e+01	2.88e+03	3.84e+02	3.70	-1.63	3.60e+01	3.86e+03
Soufriere Hills	-37.48	0.0039	5.50	0.60	2.92e+03	-2.79e+03	2.20e+00	-34.53	-0.04	-2.04e+02	3.38e+02
Tokachidake	4.98	0.99	9.38	0.95	2.73e+03	-1.26e+01	1.37e+00	22.40	0.80	3.18e+03	-3.78e+01
Unzen	0.00	0.82	6.11	-0.52	9.72e+01	-1.16e+00	1.49e-01	23.80	0.37	1.71e+02	-2.12e+01
Yakedake	6.20	0.99	4.94	-1.18	9.68e+01	-2.89e-01	2.44e-02	24.40	0.91	1.04e+02	-4.76e-01

Note: t_c is in day; m, ω, and ϕ are dimensionless; A is dimensionless for earthquake count, in meter for displacement, and in μrad for tilt; B and C are in the unit of A per day^m. The actual failure corresponds to time $t = 0$ day. Parameters A, B, and C are displayed using scientific exponential notation, where 1.00e-02 represents 1.00×10^{-2}.

Table S9. Comparison between the LPPLS and PLS models for landslide data (49 events and 94 time series monitoring data in total).

Data	LPPLS			PLS			*p*-value		
	NRMSE	NAIC	NBIC	NRMSE	NAIC	NBIC	Wilks	KS	AD
Abbotsford	4.98e-05	-6.01	-5.83	5.25e-04	-3.72	-3.61	0.00	0.00	0.00
Achoma	6.53e-03	0.19	0.51	9.20e-03	0.36	0.54	0.14	0.96	0.72
Agoyama	1.13e-04	-4.25	-3.97	1.97e-04	-3.84	-3.67	0.00	0.77	0.48
Arvigo	2.28e-05	-9.34	-9.10	3.53e-05	-9.00	-8.86	0.00	0.05	0.10
Baishi	2.36e-03	-0.01	0.31	3.51e-03	0.20	0.38	0.05	0.38	0.46
Baiyan	3.59e-04	-6.93	-6.60	1.16e-03	-5.96	-5.78	0.00	0.34	0.17
Brienz/Brinzauls (reflector 715)	3.56e-04	-2.01	-1.86	4.51e-04	-1.81	-1.73	0.00	0.04	0.17
Brienz/Brinzauls (reflector 719)	5.77e-04	-1.09	-0.95	8.25e-04	-0.77	-0.69	0.00	0.06	0.02
Brienz/Brinzauls (reflector 725)	4.80e-04	-1.43	-1.28	6.70e-04	-1.14	-1.06	0.00	0.12	0.17
Cadia	3.41e-05	-9.61	-9.27	4.75e-05	-9.54	-9.35	0.42	0.84	0.71
Copper open pit	6.52e-05	-8.94	-8.59	7.88e-05	-9.00	-8.80	0.52	0.99	0.73
Dosan (point 1)	9.47e-06	-11.45	-11.19	1.60e-05	-11.04	-10.89	0.00	0.18	0.14
Dosan (point 2)	1.57e-05	-9.91	-9.62	3.27e-05	-9.32	-9.16	0.00	0.03	0.09
Dosan (point 3)	9.96e-06	-9.15	-8.88	1.67e-05	-8.76	-8.61	0.00	0.21	0.27
Gallivaggio	1.12e-06	-15.61	-15.33	2.48e-06	-14.95	-14.79	0.00	0.61	0.60
Galterengraben (TJM1)	1.20e-03	-1.46	-1.38	4.50e-03	-0.15	-0.11	0.00	0.00	0.00
Galterengraben (TJM2)	2.26e-03	-0.53	-0.45	6.89e-03	0.57	0.61	0.00	0.01	0.00
Galterengraben (TJM6)	2.09e-03	-1.34	-1.26	3.32e-03	-0.90	-0.85	0.00	0.04	0.01
Grabengufer (GNSS)	8.41e-04	-4.82	-4.59	1.41e-03	-4.40	-4.26	0.00	0.69	0.68
Grabengufer (inclinometer W)	7.02e-03	0.49	0.75	8.07e-03	0.52	0.67	0.34	0.55	0.37
Grabengufer (inclinometer N)	2.16e-03	0.26	0.54	6.84e-03	1.27	1.43	0.00	0.27	0.08
Hogarth (extensometer 1)	3.50e-07	-16.66	-16.32	3.26e-06	-14.65	-14.46	0.00	0.28	0.17
Hogarth (extensometer 2)	1.29e-06	-15.11	-14.80	4.37e-06	-14.04	-13.87	0.00	0.12	0.21
Hogarth (extensometer 3)	2.24e-07	-17.61	-17.39	8.74e-07	-16.34	-16.21	0.00	0.15	0.08
Hogarth (extensometer 4)	2.66e-07	-17.20	-16.96	6.17e-07	-16.45	-16.31	0.00	0.00	0.00
Hogarth (extensometer 6)	1.31e-07	-18.23	-18.01	1.97e-07	-17.91	-17.78	0.00	0.18	0.18

Table S9 (continued). Comparison between the LPPLS and PLS models for landslide data (49 events and 94 time series monitoring data in total).

Data	LPPLS			PLS			*p*-value		
	NRMSE	NAIC	NBIC	NRMSE	NAIC	NBIC	Wilks	KS	AD
Iron mine	1.73e-05	-8.35	-8.05	3.20e-05	-7.88	-7.71	0.00	0.98	0.67
Jinlonggou	8.70e-06	-11.79	-11.56	2.55e-05	-10.81	-10.68	0.00	0.09	0.01
Kagemori (point 1)	4.66e-06	-11.74	-11.43	1.08e-05	-11.07	-10.89	0.00	0.46	0.21
Kagemori (point 3)	5.33e-05	-8.30	-8.16	1.69e-04	-7.19	-7.11	0.00	0.00	0.00
Kagemori (point 13)	8.75e-07	-13.54	-13.21	5.30e-06	-11.96	-11.77	0.00	0.09	0.03
Kagemori (point 15)	2.88e-05	-8.93	-8.66	6.70e-05	-8.21	-8.05	0.00	0.09	0.02
Kagemori (point 17)	1.05e-06	-12.48	-12.19	1.58e-06	-12.21	-12.04	0.00	0.77	0.42
Kagemori (point 18)	2.84e-05	-8.78	-8.48	4.79e-05	-8.41	-8.24	0.00	0.04	0.06
Kagemori (point 21)	1.33e-05	-10.08	-9.81	7.73e-05	-8.44	-8.29	0.00	0.36	0.13
Kagemori (point 23)	7.97e-06	-10.03	-9.88	3.27e-05	-8.67	-8.58	0.00	0.00	0.00
La Saxe	1.95e-03	-1.79	-1.55	1.50e-02	0.16	0.29	0.00	0.12	0.07
Letlhakane diamond mine	2.51e-04	-5.91	-5.73	1.18e-03	-4.42	-4.32	0.00	0.00	0.00
Longjing	4.27e-05	-7.78	-7.57	1.24e-04	-6.80	-6.68	0.00	0.00	0.00
Maoxian (point 1)	8.45e-05	-8.91	-8.59	1.12e-04	-8.82	-8.64	0.35	0.94	0.76
Maoxian (point 2)	8.87e-05	-8.57	-8.24	9.80e-05	-8.66	-8.47	0.95	0.94	0.77
Maoxian (point 3)	8.80e-05	-8.57	-8.25	1.04e-04	-8.60	-8.41	0.74	0.94	0.75
Mt. Beni	1.25e-04	-4.81	-4.49	2.86e-04	-4.16	-3.98	0.00	0.23	0.24
Mud Greek	1.21e-03	-4.33	-4.03	3.25e-03	-3.50	-3.33	0.00	0.69	0.60
Nevis Bluff (point 1)	3.08e-05	-9.31	-9.13	6.23e-05	-8.67	-8.56	0.00	0.00	0.00
Nevis Bluff (point 2)	2.78e-05	-8.85	-8.64	5.22e-05	-8.29	-8.17	0.00	0.00	0.01
Nevis Bluff (point A)	2.48e-05	-9.10	-8.91	5.31e-05	-8.40	-8.29	0.00	0.00	0.00
New Tredegar	5.61e-05	-7.08	-6.78	9.85e-05	-6.67	-6.50	0.00	0.71	0.64
Northern Bohemia	1.78e-05	-11.95	-11.64	1.01e-04	-10.39	-10.21	0.00	0.18	0.05
Open pit mine (event 3)	7.27e-06	-10.44	-10.15	1.88e-05	-9.62	-9.46	0.00	0.92	0.75
Open pit mine (event 4)	1.60e-04	-7.23	-7.00	3.59e-04	-6.51	-6.38	0.00	0.06	0.02

Table S9 (continued). Comparison between the LPPLS and PLS models for landslide data (49 events and 94 time series monitoring data in total).

Data	LPPLS			PLS			p-value		
	NRMSE	NAIC	NBIC	NRMSE	NAIC	NBIC	Wilks	KS	AD
Open pit mine (event 5)	1.71e-05	-11.21	-10.98	7.90e-05	-9.77	-9.64	0.00	0.01	0.00
Otomura	4.16e-05	-8.45	-8.18	4.76e-05	-8.44	-8.28	0.44	0.95	0.72
Preonzo (extensometer 1)	1.14e-05	-9.81	-9.56	3.90e-05	-8.69	-8.55	0.00	0.09	0.12
Preonzo (extensometer 2)	1.56e-05	-9.38	-9.09	7.09e-05	-8.01	-7.85	0.00	0.55	0.23
Preonzo (extensometer 3)	2.71e-05	-7.88	-7.62	8.45e-05	-6.86	-6.71	0.00	0.17	0.15
Preonzo (extensometer 4)	1.27e-05	-8.21	-7.94	1.10e-04	-6.16	-6.01	0.00	0.37	0.13
Preonzo (extensometer 5)	1.90e-05	-8.01	-7.78	1.29e-04	-6.19	-6.05	0.00	0.28	0.30
Preonzo (reflector 2)	1.09e-04	-5.24	-4.93	4.72e-04	-3.94	-3.76	0.00	0.03	0.06
Preonzo (reflector 4)	8.14e-05	-5.53	-5.21	4.54e-04	-3.98	-3.80	0.00	0.16	0.05
Preonzo (reflector 5)	6.35e-05	-6.15	-5.84	3.38e-04	-4.66	-4.48	0.00	0.08	0.05
Preonzo (reflector 8)	3.87e-05	-7.12	-6.80	2.09e-04	-5.62	-5.44	0.00	0.08	0.05
Preonzo (reflector 9)	2.22e-05	-8.15	-7.92	9.31e-05	-6.81	-6.68	0.00	0.30	0.29
Puigcercós (area 4)	1.53e-04	-6.82	-6.47	2.40e-04	-6.68	-6.48	0.35	0.46	0.54
Puigcercós (area 6)	6.97e-05	-6.95	-6.60	2.17e-04	-6.14	-5.94	0.03	0.43	0.16
Puigcercós (area 7)	1.11e-04	-6.84	-6.49	3.51e-04	-5.99	-5.79	0.00	0.13	0.06
Puigcercós (area 9)	9.27e-05	-7.15	-6.80	2.31e-04	-6.57	-6.37	0.05	0.71	0.35
Road slope (event 1)	1.11e-06	-12.62	-12.35	2.54e-05	-9.62	-9.46	0.00	0.00	0.00
Road slope (event 2)	2.01e-04	-5.91	-5.80	7.46e-04	-4.62	-4.56	0.00	0.00	0.00
Road slope (event 3)	4.88e-06	-13.13	-12.86	1.41e-05	-12.19	-12.04	0.00	0.02	0.01
Road slope (event 4)	1.82e-05	-11.60	-11.33	1.77e-04	-9.45	-9.30	0.00	0.00	0.00
Road slope (event 5)	2.49e-05	-11.51	-11.30	5.67e-05	-10.77	-10.65	0.00	0.00	0.00

Table S9 (continued). Comparison between the LPPLS and PLS models for landslide data (49 events and 94 time series monitoring data in total).

Data	LPPLS			PLS			p-value		
	NRMSE	NAIC	NBIC	NRMSE	NAIC	NBIC	Wilks	KS	AD
Road slope (event 6)	2.07e-05	-11.14	-10.93	4.87e-05	-10.37	-10.25	0.00	0.01	0.00
Road slope (event 7)	5.26e-05	-9.05	-8.75	7.54e-05	-8.84	-8.67	0.02	0.89	0.55
Road slope (event 8)	1.01e-05	-11.11	-10.86	2.17e-05	-10.44	-10.30	0.00	0.48	0.18
Road slope (event 9)	1.15e-04	-6.29	-6.19	2.50e-04	-5.54	-5.48	0.00	0.00	0.00
Road slope (event 10)	4.65e-05	-8.93	-8.75	1.16e-04	-8.08	-7.97	0.00	0.00	0.00
Roesgrenda	3.24e-05	-10.34	-10.13	4.42e-05	-10.11	-9.99	0.00	0.10	0.12
Takabayama	9.01e-06	-8.11	-7.84	5.63e-05	-6.41	-6.25	0.00	0.00	0.00
Vajont (bench mark 2)	6.85e-04	-3.93	-3.70	1.70e-03	-3.11	-2.98	0.00	0.00	0.01
Vajont (bench mark 4)	3.78e-05	-7.61	-7.37	1.42e-04	-6.38	-6.24	0.00	0.04	0.00
Vajont (bench mark 6)	4.61e-04	-4.68	-4.46	1.18e-03	-3.82	-3.69	0.00	0.00	0.00
Vajont (bench mark 58)	9.32e-05	-6.42	-6.23	2.95e-04	-5.32	-5.22	0.00	0.00	0.00
Veslemannen (radar point 1)	1.14e-03	-2.02	-1.85	1.29e-02	0.34	0.44	0.00	0.00	0.00
Veslemannen (radar point 2)	5.55e-04	-2.84	-2.64	3.73e-03	-1.00	-0.89	0.00	0.00	0.00
Veslemannen (radar point 3)	4.34e-04	-3.28	-3.11	3.57e-03	-1.23	-1.13	0.00	0.00	0.00
Veslemannen (radar point 4)	3.42e-04	-4.08	-3.91	2.53e-03	-2.14	-2.04	0.00	0.00	0.00
Veslemannen (radar point 5)	2.69e-04	-4.69	-4.51	2.10e-03	-2.68	-2.58	0.00	0.00	0.00
Veslemannen (radar point 6)	1.93e-04	-5.00	-4.82	9.47e-04	-3.47	-3.37	0.00	0.00	0.00
Veslemannen (radar point 7)	2.51e-04	-4.93	-4.75	1.71e-03	-3.07	-2.96	0.00	0.00	0.00
Welland (point 1)	2.46e-06	-14.03	-13.80	1.91e-05	-12.06	-11.93	0.00	0.00	0.00
Welland (point 2)	6.32e-06	-13.08	-12.91	1.95e-05	-12.00	-11.91	0.00	0.04	0.00
Xinmo	9.00e-05	-8.89	-8.57	1.14e-04	-8.83	-8.65	0.40	0.16	0.28
Xintan	3.44e-03	-1.11	-0.78	6.74e-03	-0.63	-0.45	0.00	0.36	0.21

Note: NRMSE is displayed using scientific exponential notation, where 1.00e-02 represents 1.00×10^{-2}.

Table S10. Comparison between the LPPLS and PLS models for rockburst data (11 events and 11 time series monitoring data in total).

Data	LPPLS			PLS			p-value		
	NRMSE	NAIC	NBIC	NRMSE	NAIC	NBIC	Wilks	KS	AD
Coal mine (cut-through #4)	1.09e-01	5.86	6.10	1.89e-01	6.32	6.45	0.00	0.67	0.42
Coal mine (cut-through #5)	4.34e-05	-8.85	-8.61	1.42e-04	-7.76	-7.62	0.00	0.03	0.00
Gold mine (event 1)	4.60e-01	9.82	10.16	1.42e+00	10.66	10.86	0.00	0.53	0.33
Gold mine (event 2)	1.44e+00	10.89	11.21	2.02e+00	10.80	10.99	0.86	0.86	0.70
Gold mine (event 3)	4.71e+00	13.78	13.95	7.84e+00	14.23	14.33	0.00	0.09	0.03
Gold mine (event 4)	2.46e+00	13.00	13.16	3.32e+00	13.25	13.34	0.00	0.39	0.31
Gold mine (event 5)	3.52e+00	13.10	13.32	7.25e+00	13.75	13.87	0.00	0.20	0.07
Gold mine (event 6)	2.11e+00	11.91	12.21	3.19e+00	12.17	12.34	0.01	0.71	0.46
Gold mine (event 7)	3.68e+00	12.67	12.95	5.29e+00	12.90	13.06	0.01	0.94	0.73
Gold mine (event 8)	1.08e+01	13.86	14.20	2.63e+01	14.49	14.69	0.01	0.20	0.10
Platinum mine	9.62e-06	-11.37	-11.26	1.58e-05	-10.91	-10.84	0.00	0.00	0.00

Note: NRMSE is displayed using scientific exponential notation, where 1.00e-02 represents 1.00×10^{-2}.

Table S11. Comparison between the LPPLS and PLS models for glacier data (17 events and 21 time series monitoring data in total).

Data	LPPLS			PLS			p-value		
	NRMSE	NAIC	NBIC	NRMSE	NAIC	NBIC	Wilks	KS	AD
Amery	1.90e-02	2.44	2.52	2.05e-02	2.50	2.54	0.00	0.05	0.10
Eiger glacier (2001 event)	1.71e-05	-7.23	-7.00	2.19e-05	-7.08	-6.95	0.00	0.82	0.67
Eiger glacier (2016 event)	9.85e-05	-5.09	-4.80	1.29e-04	-4.97	-4.80	0.05	0.36	0.32
Grandes Jorasses (2014 event, prism 13)	2.56e-04	-2.80	-2.68	1.01e-03	-1.46	-1.39	0.00	0.00	0.00
Grandes Jorasses (2014 event, prism 14)	7.37e-05	-4.11	-3.98	1.10e-04	-3.75	-3.67	0.00	0.00	0.00
Grandes Jorasses (2020 event)	5.02e-06	-9.00	-8.88	1.62e-05	-7.86	-7.79	0.00	0.00	0.00
Gruben	2.00e-05	-6.17	-5.89	3.34e-05	-6.16	-5.99	0.71	0.43	0.46
Mönch	2.57e-04	-3.73	-3.50	6.46e-04	-2.90	-2.77	0.00	0.00	0.00
Planpincieux (event 1)	4.96e-05	-4.17	-3.94	1.17e-04	-3.41	-3.28	0.00	0.31	0.14
Planpincieux (event 2)	8.06e-04	-1.14	-0.89	2.28e-03	-0.20	-0.06	0.00	0.02	0.00
Planpincieux (event 3)	1.43e-04	-2.90	-2.64	4.75e-04	-1.81	-1.66	0.00	0.11	0.01
Planpincieux (event 4)	2.43e-04	-2.36	-2.01	4.23e-03	0.22	0.41	0.00	0.07	0.01
Planpincieux (event 5)	1.97e-04	-2.92	-2.60	8.03e-04	-1.71	-1.53	0.00	0.06	0.04
Planpincieux (event 6)	1.00e-04	-3.76	-3.49	6.15e-04	-2.08	-1.92	0.00	0.04	0.00
UK211	1.95e-01	6.62	6.94	3.68e-01	7.05	7.24	0.01	0.76	0.40
Weisshorn (1973 event)	5.31e-03	1.38	1.71	1.04e-02	1.86	2.04	0.00	0.12	0.08
Weisshorn (2005 event, prism 103)	1.46e-05	-6.17	-5.92	5.92e-05	-4.88	-4.74	0.00	0.00	0.00
Weisshorn (2005 event, prism 104)	1.10e-05	-6.44	-6.19	3.54e-05	-5.37	-5.23	0.00	0.06	0.01
Weisshorn (2005 event, prism 105)	2.45e-05	-5.58	-5.34	6.35e-05	-4.73	-4.59	0.00	0.04	0.01
Weisshorn (2005 event, prism 106)	1.37e-05	-6.36	-6.11	3.29e-05	-5.59	-5.44	0.00	0.08	0.04
Weissmies	1.93e-03	0.40	0.62	2.60e-03	0.62	0.75	0.00	0.28	0.27

Note: NRMSE is displayed using scientific exponential notation, where 1.00e-02 represents 1.00×10^{-2}.

Table S12. Comparison between the LPPLS and PLS models for volcano data (32 events and 34 time series monitoring data in total).

Data	LPPLS			PLS			p-value		
	NRMSE	NAIC	NBIC	NRMSE	NAIC	NBIC	Wilks	KS	AD
Adatara	1.37e-02	3.11	3.24	5.67e-02	4.49	4.57	0.00	0.00	0.00
Asama	1.28e+00	12.53	12.63	5.09e+00	13.88	13.94	0.00	0.00	0.00
Augustine	4.00e-01	9.49	9.62	5.95e-01	9.85	9.93	0.00	0.01	0.07
Axial Seamount	6.02e-04	-4.31	-4.24	1.55e-03	-3.37	-3.34	0.00	0.00	0.00
Bezymianny	5.88e-03	2.64	2.99	1.47e-02	3.25	3.45	0.03	0.28	0.25
Etna (1989 event)	2.49e-02	4.67	4.95	4.89e-02	5.22	5.38	0.00	0.81	0.44
Etna (2013 event)	8.84e-03	5.55	5.69	7.78e-02	7.68	7.76	0.00	0.00	0.00
Hierro	4.33e+00	13.69	13.86	3.50e+01	15.73	15.82	0.00	0.00	0.00
Kilauea (1971 event)	3.14e-01	8.84	9.07	1.11e+00	10.02	10.15	0.00	0.02	0.01
Kilauea (1972 event)	9.35e-01	11.77	12.02	1.44e+01	14.41	14.55	0.00	0.00	0.00
Kilauea (1983 event)	2.03e+00	12.19	12.47	8.29e+00	13.47	13.63	0.00	0.01	0.01
Kujusan	2.75e-02	2.27	2.45	8.43e-02	3.33	3.44	0.00	0.05	0.00
Mauna Loa	2.90e-04	-4.42	-4.27	5.01e-04	-3.92	-3.83	0.00	0.04	0.02
Merapi (2006 event)	2.75e+00	13.73	13.97	5.48e+00	14.32	14.46	0.00	0.03	0.03
Merapi (2010 event)	8.49e-02	7.29	7.60	1.44e-01	7.65	7.82	0.01	0.64	0.47
Pinatubo	2.08e-01	8.99	9.31	9.89e-01	10.37	10.55	0.00	0.40	0.11
Redoubt (1989 event)	3.82e-02	3.96	4.26	1.07e-01	4.84	5.01	0.00	0.22	0.07
Redoubt (2009 event)	6.27e-01	9.70	9.95	1.31e+00	10.34	10.48	0.00	0.03	0.01
Ruapehu (1995 event)	8.01e-02	5.72	5.86	3.76e-01	7.23	7.30	0.00	0.00	0.00
Ruapehu (1996 event)	4.78e-01	9.12	9.30	1.67e+00	10.31	10.42	0.00	0.00	0.00
Ruapehu (2006 event)	2.47e-02	3.27	3.46	3.35e-02	3.52	3.62	0.00	0.87	0.58
Sakurajima	5.03e-01	9.11	9.30	1.17e+00	9.88	9.99	0.00	0.30	0.15
Sierra Negra (2005 event)	7.07e-04	-3.59	-3.35	1.03e-03	-3.31	-3.17	0.00	0.20	0.23
Sierra Negra (2018 event)	3.04e-04	-4.21	-4.05	3.92e-04	-4.01	-3.92	0.00	0.04	0.13
St. Helens (1980 event)	1.75e-03	1.22	1.46	6.85e-03	2.49	2.63	0.00	0.48	0.32

Table S12 (continued). Comparison between the LPPLS and PLS models for volcano data (32 events and 34 time series monitoring data in total).

Data	LPPLS			PLS			*p*-value		
	NRMSE	NAIC	NBIC	NRMSE	NAIC	NBIC	Wilks	KS	AD
St. Helens (1981 event)	8.66e-02	6.81	6.96	2.97e-01	8.00	8.08	0.00	0.01	0.00
St. Helens (1982 event, seismic data)	4.27e-01	8.40	8.66	1.24e+00	9.35	9.50	0.00	0.01	0.01
St. Helens (1982 event, radial tilt)	1.32e-01	8.29	8.54	3.77e-01	9.24	9.38	0.00	0.15	0.06
St. Helens (1982 event, tangential tilt)	6.55e-02	7.82	8.06	1.66e-01	8.65	8.79	0.00	0.16	0.10
St. Helens (1985 event)	2.77e-02	5.28	5.58	1.53e-01	6.83	7.00	0.00	0.69	0.53
Soufriere Hills	4.00e-02	3.45	3.78	9.03e-02	4.07	4.25	0.00	0.54	0.43
Tokachidake	2.49e+00	11.84	12.16	9.57e+00	13.01	13.19	0.00	0.14	0.04
Unzen	5.30e-02	4.69	5.01	3.41e-01	6.39	6.56	0.00	0.05	0.01
Yakedake	3.52e-02	3.69	3.90	1.01e-01	4.67	4.79	0.00	0.04	0.01

Note: NRMSE is displayed using scientific exponential notation, where 1.00e-02 represents 1.00×10^{-2}.

Table S13. Parameters of the LPPLS and PLS calibration to landslide data (49 events and 94 time series monitoring data in total).

	Calibration window size (day)	Number of data points	Aggregation interval (day)
Abbotsford	19.04	97	N/A
Achoma	114.76	34	N/A
Agoyama	42.00	43	1
Arvigo	63.00	63	1
Baishi	31.00	32	1
Baiyan	394.75	30	N/A
Brienz/Brinzauls (reflector 715)	139.00	140	1
Brienz/Brinzauls (reflector 719)	152.00	153	1
Brienz/Brinzauls (reflector 725)	144.00	145	1
Cadia	298.86	23	N/A
Copper open pit	241.73	24	N/A
Dosan (point 1)	2.17	53	0.042
Dosan (point 2)	1.75	43	0.042
Dosan (point 3)	1.92	47	0.042
Gallivaggio	26.18	45	1
Galterengraben (TJM1)	360.00	361	1
Galterengraben (TJM2)	346.00	347	1
Galterengraben (TJM6)	290.00	291	1
Grabengufer (GNSS)	2.83	66	0.042
Grabengufer (inclinometer W)	2.21	53	0.042
Grabengufer (inclinometer N)	1.75	43	0.042
Hogarth (extensometer 1)	35.00	27	1
Hogarth (extensometer 2)	45.00	38	1
Hogarth (extensometer 3)	76.00	68	1
Hogarth (extensometer 4)	72.00	65	1
Hogarth (extensometer 6)	80.00	73	1
Iron mine	39.00	40	1
Jinlonggou	65.00	66	1
Kagemori (point 1)	35.00	36	1
Kagemori (point 3)	140.00	141	1
Kagemori (point 13)	32.00	28	1
Kagemori (point 15)	51.00	49	1
Kagemori (point 17)	42.00	43	1
Kagemori (point 18)	39.00	39	1
Kagemori (point 21)	50.00	50	1
Kagemori (point 23)	130.00	129	1
La Saxe	63.00	63	1
Letlhakane diamond mine	97.22	105	N/A

Table S13 (continued). Parameters of the LPPLS and PLS calibration to landslide data (49 events and 94 time series monitoring data in total).

	Calibration window size (day)	Number of data points	Aggregation interval (day)
Longjing	14.29	75	N/A
Maoxian (point 1)	656.50	31	N/A
Maoxian (point 2)	656.50	31	N/A
Maoxian (point 3)	656.50	31	N/A
Mt. Beni	233.23	32	N/A
Mud Greek	472.80	38	N/A
Nevis Bluff (point 1)	100.00	101	1
Nevis Bluff (point 2)	81.00	82	1
Nevis Bluff (point A)	97.00	98	1
New Tredegar	37.94	39	N/A
Northern Bohemia	36.58	36	N/A
Open pit mine (event 3)	0.46	44	0.01
Open pit mine (event 4)	1.40	68	0.021
Open pit mine (event 5)	2.79	67	0.042
Otomura	48.00	49	1
Preonzo (extensometer 1)	57.00	57	1
Preonzo (extensometer 2)	41.00	41	1
Preonzo (extensometer 3)	52.00	52	1
Preonzo (extensometer 4)	51.00	51	1
Preonzo (extensometer 5)	64.00	65	1
Preonzo (reflector 2)	36.00	36	1
Preonzo (reflector 4)	34.00	34	1
Preonzo (reflector 5)	33.00	33	1
Preonzo (reflector 8)	33.00	33	1
Preonzo (reflector 9)	66.00	67	1
Puigcercós (area 4)	2116.87	19	N/A
Puigcercós (area 6)	1753.69	18	N/A
Puigcercós (area 7)	2120.11	20	N/A
Puigcercós (area 9)	1744.84	18	N/A
Road slope (event 1)	1.96	48	0.042
Road slope (event 2)	9.33	225	0.042
Road slope (event 3)	0.17	49	0.0035
Road slope (event 4)	0.08	48	0.0017
Road slope (event 5)	0.26	76	0.0035
Road slope (event 6)	1.58	76	0.021
Road slope (event 7)	0.83	40	0.021
Road slope (event 8)	0.21	60	0.0035
Road slope (event 9)	9.92	238	0.042
Road slope (event 10)	0.68	99	0.0069

Table S13 (continued). Parameters of the LPPLS and PLS calibration to landslide data (49 events and 94 time series monitoring data in total).

	Calibration window size (day)	Number of data points	Aggregation interval (day)
Roesgrenda	35.55	79	N/A
Takabayama	46.00	47	1
Vajont (bench mark 2)	69.00	70	1
Vajont (bench mark 4)	61.00	62	1
Vajont (bench mark 6)	72.00	73	1
Vajont (bench mark 58)	98.00	99	1
Veslemannen (radar point 1)	108.00	108	1
Veslemannen (radar point 2)	91.00	91	1
Veslemannen (radar point 3)	108.00	108	1
Veslemannen (radar point 4)	107.00	107	1
Veslemannen (radar point 5)	104.00	104	1
Veslemannen (radar point 6)	102.00	102	1
Veslemannen (radar point 7)	101.00	101	1
Welland (point 1)	2.96	71	0.042
Welland (point 2)	4.83	116	0.042
Xinmo	728.27	34	N/A
Xintan	221.87	31	7

Note: if no aggregation treatment is applied to the data, the aggregation interval is indicated as N/A.

Table S14. Parameters of the LPPLS and PLS calibration to rockburst data (11 events and 11 time series monitoring data in total).

	Calibration window size (day)	Number of data points	Aggregation interval (day)
Coal mine (cut-through #4)	1.33	64	0.021
Coal mine (cut-through #5)	2.58	63	0.042
Gold mine (event 1)	4.41	21	N/A
Gold mine (event 2)	1.34	14	N/A
Gold mine (event 3)	11.04	108	N/A
Gold mine (event 4)	43.01	125	N/A
Gold mine (event 5)	12.41	77	N/A
Gold mine (event 6)	5.77	39	N/A
Gold mine (event 7)	63.18	46	N/A
Gold mine (event 8)	114.20	23	N/A
Platinum mine	8.08	195	0.042

Note: if no aggregation treatment is applied to the data, the aggregation interval is indicated as N/A.

Table S15. Parameters of the LPPLS and PLS calibration to glacier data (17 events and 21 time series monitoring data in total).

	Calibration window size (day)	Number of data points	Aggregation interval (day)
Amery	2240.00	321	7
Eiger glacier (2001 event)	5.15	64	N/A
Eiger glacier (2016 event)	39.00	40	N/A
Grandes Jorasses (2014 event, prism 13)	178.00	179	1
Grandes Jorasses (2014 event, prism 14)	161.00	162	1
Grandes Jorasses (2020 event)	7.75	187	N/A
Gruben	3.21	12	N/A
Mönch	66.00	67	1
Planpincieux (event 1)	67.00	68	1
Planpincieux (event 2)	57.00	58	1
Planpincieux (event 3)	52.00	53	1
Planpincieux (event 4)	20.00	21	1
Planpincieux (event 5)	30.00	31	1
Planpincieux (event 6)	46.00	47	1
UK211	428.43	30	N/A
Weisshorn (1973 event)	252.70	31	7
Weisshorn (2005 event, #103)	23.26	54	N/A
Weisshorn (2005 event, #104)	23.26	59	N/A
Weisshorn (2005 event, #105)	23.26	62	N/A
Weisshorn (2005 event, #106)	23.26	56	N/A
Weissmies	75.00	76	1

Note: if no aggregation treatment is applied to the data, the aggregation interval is indicated as N/A.

Table S16. Parameters of the LPPLS and PLS calibration to volcano data (32 events and 34 time series monitoring data in total).

	Calibration window size (day)	Number of data points	Aggregation interval (day)
Adatara	1127.00	162	7
Asama	238.00	239	1
Augustine	1141.00	164	7
Axial Seamount	3171.00	454	7
Bezymianny	29.72	20	N/A
Etna (1989 event)	322.00	47	7
Etna (2013 event)	140.00	141	1
Hierro	112.00	113	1
Kilauea (1971 event)	34.00	69	0.5
Kilauea (1972 event)	392.00	57	7
Kilauea (1983 event)	322.00	47	7
Kujusan	101.00	102	1
Mauna Loa	129.00	130	1
Merapi (2006 event)	62.00	63	1
Merapi (2010 event)	34.00	35	1
Pinatubo	32.00	33	1
Redoubt (1989 event)	266.00	39	7
Redoubt (2009 event)	57.00	58	1
Ruapehu (1995 event)	153.00	154	1
Ruapehu (1996 event)	102.00	103	1
Ruapehu (2006 event)	282.00	95	3
Sakurajima	92.00	93	1
Sierra Negra (2005 event)	910.00	66	14
Sierra Negra (2018 event)	1638.00	118	14
St. Helens (1980 event)	59.00	60	1
St. Helens (1981 event)	142.00	143	1
St. Helens (1982 event, seismic data)	52.00	53	1
St. Helens (1982 event, radial tilt)	58.00	59	1
St. Helens (1982 event, tangential tilt)	59.00	60	1
St. Helens (1985 event)	37.00	38	1
Soufriere Hills	265.86	30	1
Tokachidake	224.00	33	7
Unzen	238.00	35	7
Yakedake	234.00	79	3

Note: if no aggregation treatment is applied to the data, the aggregation interval is indicated as N/A.